

MICROFLUIDICS AND NEURAL INTERFACES DEVELOPMENT
FOR THE SAFE DIRECT CURRENT STIMULATOR

by

Ankitha Rajagopalan Nair

A thesis submitted to Johns Hopkins University in conformity with the requirements
for the degree of Master of Science in Engineering.

Baltimore, Maryland

August 2018

© 2018 Ankitha Rajagopalan Nair

All Rights Reserved.

ABSTRACT

Safety of commercial neural implants fundamentally limits its working to the use of charge-balanced, biphasic pulses to interact with target neurons using metal electrodes. Short biphasic pulses are used to avoid toxic electrochemical reactions at the electrode-tissue interfaces. Biphasic pulses are effective at exciting neurons, but quite limited in inhibiting their activity. In contrast, direct current can both excite and inhibit neurons, however it leads to the formation of harmful, Faradaic reactions at the metal electrode/tissue interface. To address this challenge of safety over chronic use, we are developing the Safe Direct Current Stimulator (SDCS) technology, that generates an ionic direct current (iDC) from a biphasic input signal using a network of microfluidic channels and mechanical valves. This rectified iDC is applied to the target neural tissue through an ionically conductive neural interface.

A key enabler towards transforming the SDCS concept from a benchtop design to an implantable neural prosthesis is the design of a miniature valve. Several valve architectures and actuation mechanism were studied for the development of the microfluidics in SDCS technology, before settling on the plunger-membrane microvalve design. This thesis characterizes a miniature polydimethylsiloxane (PDMS) based elastomeric normally closed (NC) mechanical valve actuated using a shape-memory alloy (SMA) wire through distinct tests and examines its current capability for iDC delivery. The analysis of the test outputs confirmed the feasibility of using this design for rectifying the charge-balanced alternating current (AC) into iDC.

As metal electrodes are unsuitable for delivering iDC to the neural tissue safely, an ionic conductive neural lead is built. These gel-based, PDMS electrodes should be designed within the acceptable pressure limits that a nerve can handle safely.

Preliminary experiments were conducted to verify the design and conductivity of the lead. While the results suggest that the lead design maintains the pressure below the maximum limit, its high impedance raises concerns.

Although this thesis forms a basis for development of the SDCS device, further experimentation and progress is required for a reliable, safe, chronic, and fully functional device.

Readers: Dr. Gene Y. Fridman, Dr. Nitish V. Thakor, Dr. Yun Guan

ACKNOWLEDGEMENTS

This intensive learning period has had a profound impact on me in both a professional capacity and on a personal level. I would like to reflect on the people who have supported me throughout this learning process.

I would first like to express my sincere gratitude to my advisor, Dr. Gene Fridman for the unwavering support, patient guidance and words of encouragement and advice he has provided throughout my time as his student. Thank you for taking me under your wing. I find myself extremely lucky to have such a dedicated professor, who is always available for his students and gives us the freedom to pursue various directions without objection.

Moreover, I am grateful to our microfluidics team, Dr. Raviraj Thakur and doctoral candidate Chaojun Cheng for showing me the true meaning of teamwork. I would like to thank Dr. Raviraj Thakur for his mentorship and leadership throughout these projects and for always having time to answer questions, no matter how trivial. Furthermore, I would like to thank Dr. Felix Aplin and Dilawer Singh also for acting as secondary mentors in research and life. I am ever so grateful to my colleague and doctoral candidate Golnoosh Kamali. Thank you for always being there, lending an ear, offering great advice and for simply being you. I am forever indebted to all of you for providing me with the perfect lab atmosphere to grow as a researcher and as a person.

A good support system is never complete without my family. Thank you for encouraging me in all my pursuits and being a continuous source of emotional support and wise counsel. Thank you for believing in me and teaching me to keep smiling through all the difficulties in life and that no obstacle is ever a herculean task.

TABLE OF CONTENTS

ABSTRACT.....	ii
ACKNOWLEDGEMENTS.....	iv
TABLES OF CONTENTS	v
LIST OF TABLES.....	vii
LIST OF FIGURES	vii
CHAPTER 1: INTRODUCTION	
1.1 Neural Stimulation Theory	1
1.2 Neural Prostheses.....	5
1.3 Safe Direct Current Stimulator Technology	7
1.4 Thesis Overview	11
CHAPTER 2: MANUFACTURING METHODOLOGIES FOR MICROFLUIDICS	
2.1 Introduction.....	15
2.2 Fabrication Techniques for Elastomeric Structures.....	16
2.2.1 Soft Lithographic Process	17
2.2.2 3D Printing Technology.....	18
2.2.3 Replica Molding of PDMS	28
CHAPTER 3: MICROFLUIDICS FOR SDCS	
3.1 History of Microvalves	32
3.2 Microvalve Classification	35
3.2.1 Passive Valves	35
3.2.2 Active Valves.....	36
3.3 SDCS Valve Requirements.....	44
3.4 Experiment 1: Characterization of Normally-Open Valve Geometry	45
3.4.1 Fabrication Methods	46
3.4.2 Test and Measurement	49
3.4.3 Results.....	50
3.4.4 Discussions	53
3.5 Experiment 2: Characterization of Normally-Closed Valves	54
3.5.1 Fabrication Methods	55
3.5.2 Test and Measurement	57
3.5.3 Results.....	62
3.5.4 Discussions	69

3.6 Experiment 3: Valve Rectification.....	69
3.6.1 Fabrication Methods	70
3.6.2 Test and Measurement	70
3.6.3 Results	70
3.6.4 Discussions	72
CHAPTER 4: NEURAL INTERFACE FOR AN SDCS APPLICATION	
4.1 Introduction.....	73
4.1.1 Historical Implications.....	74
4.1.2 Nerve Anatomy.....	78
4.1.3 Neural Electrodes.....	81
4.1.4 Aims for SDCS	86
4.2 Design Considerations	86
4.2.1 Cuff-Clamp Lead Design.....	95
4.3 Methods.....	98
4.4 Test and Measurements.....	100
4.4.1 <i>In-Vivo</i> Characterization	101
4.4.2 Impedance Testing	101
4.4.3 Pressure Calculations	103
4.5 Results.....	105
4.5.1 <i>In-Vivo</i> Characterization	105
4.5.2 Impedance Testing	107
4.5.3 Pressure Calculations	109
4.6 Discussions	115
CHAPTER 5: CONCLUSIONS	117
BIBLIOGRAPHY	119
CURRICULUM VITAE.....	125

LIST OF TABLES

Table 1: Pressure Calculations.....	112
-------------------------------------	-----

LIST OF FIGURES

Figure 1: Nerve Structure.....	1
Figure 2: Action Potential.....	4
Figure 3: SDCS 1 Design.....	9
Figure 4: SDCS 2 Design.....	9
Figure 5: Functional Layers of SDCS Device	10
Figure 6: Microvalve Design Iterations	12
Figure 7: Neural Interface Design Iterations	13
Figure 8: UV Curing of 3D Printed Molds	26
Figure 9: Absorption Spectrum of Water.....	27
Figure 10: Fabrication Process of PDMS Valves	31
Figure 11: Characterizing the Actuation Mechanisms.....	38
Figure 12: Actuation Principles of Microvalves	43
Figure 13: Depiction of Valve States.....	47
Figure 14: Normally-Open Valve Fabrication Process	49
Figure 15: Testing Setup of Normally-Open Valves	50
Figure 16: Impedance Characterization of Squeeze Valves	51
Figure 17: Impedance Characterization of Plunger Valves	52
Figure 18: Normally-Closed Valve Design and Fabrication	55
Figure 19: Testing Setup of Normally-Closed Valves	58
Figure 20: Impedance Characterization of Normally-Closed Valve Geometry	62
Figure 21: Electrical Actuation of the Plunger-Membrane Valve.	64
Figure 22: Valve States Based on the Shape-Memory Alloy Actuation	66
Figure 23: Long-term Testing of the Valve	67
Figure 24: Leakage Testing of the Valve.....	68
Figure 25: Valve Rectification.....	71
Figure 26: Neural Anatomy	79
Figure 27: Types of Neural Interfaces	82
Figure 28: Closure Mechanisms of Cuff Electrodes.....	91
Figure 29: Stimulation Modes for Cuff Electrodes.....	93

Figure 30: Cuff Electrode Design and Fabrication	96
Figure 31: C-Clamp Design and Fabrication	97
Figure 32: Final Constructed Elements of the Electrode	99
Figure 33: Experimental Setup for Force Testing of the Clamp.....	103
Figure 34: Implantation of Cuff-Clamp Lead System	107
Figure 35: Effect of Area and Electrolyte Composition on Impedance.....	108
Figure 36: Characterization of Clamp's Opening Height	110
Figure 37: Hysteresis Plot.....	111
Figure 38: Characterization of Clamp's Length	114

CHAPTER 1: INTRODUCTION

1.1 Neural Stimulation Principle

The nervous system is the body's electrochemical communication system. It receives information from the environment through sensory stimuli (sensation), processes the stimuli (integration) and generates appropriate responses (signalling and secretion) to this. Nerves provide a primary pathway for the transmission of nerve impulses through specialized cells called neurons. These cells are responsible for numerous processes including generation, conduction and transmission of both electrical and chemical signals throughout the body. Aside from neurons, nervous tissue is also composed of glial cells, which play a supporting role for the tissue and are necessary for the neurons to perform their functions. [1]

There are diverse specialized nerve cells that respond to various stimuli and perform different tasks. However, they have a basic structure that is depicted in Figure 1. A neuron consists of a cell body, dendrites, and an axon. The cell body or soma

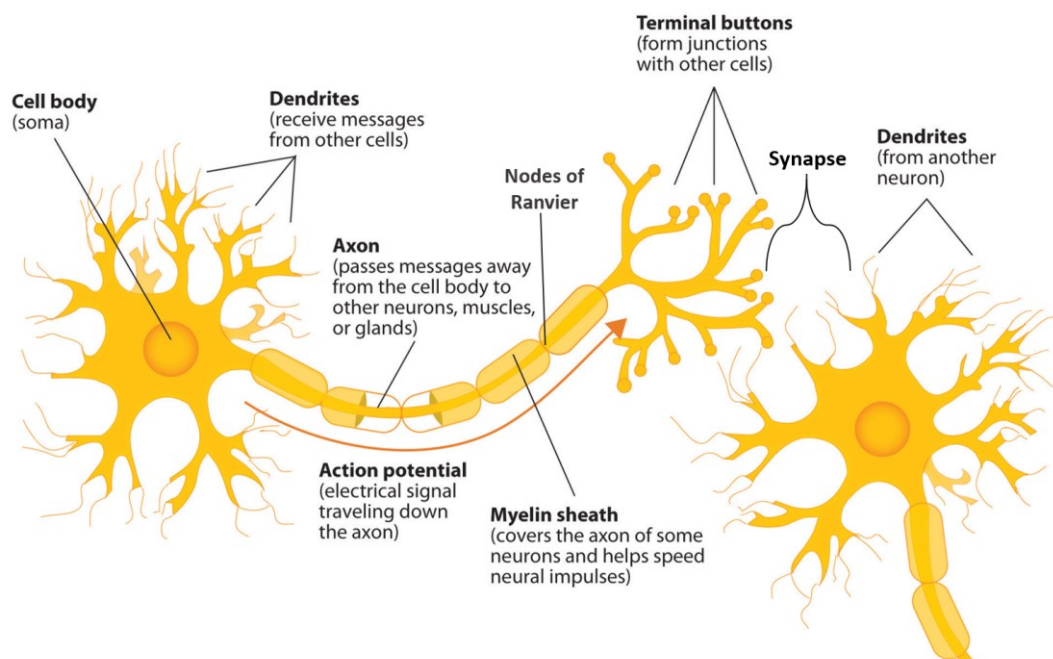


Figure 1. Nerve Structure: The basic structure of a nerve cell. Adapted from [107]

houses several organelles that are vital for the survival of the neuron. Dendrites are cellular extensions that are made up of several leaf-like structures called spines, which is the receiving part of the neuron. They are responsible for conducting the nerve impulses. Axon is a long, tube-like process that emerges from an initial segment called the axon hillock and terminates at the axon terminal. It acts as the transmitting part of the neuron by communicating with many target cells. Some portions are covered with an external, insulating cover called the myelin sheath. In the peripheral nerve, this is produced by a neurolemmocyte called Schwann cell. However, the myelin sheath is not continuous and is interrupted in regular intervals by gaps called nodes of Ranvier. The chemical junction between the axon terminals of one neuron and the dendrite of the next is known as a synapse. The dendrites obtain the inputs from several different synapses and communicates with the cell body. Hence, the neuron is said to have a polarity as the passage for information flow occurs only in one direction.

Neurons convey the messages electrochemically through charged particles called ions. The electrical signal generated at the output of a neuron can cause excitation or inhibition of the neuron. These electrical impulses are known as action potentials. They occur due to shifts in the neuron's transmembrane potential caused by concentration gradients of ions. This potential defines the distribution of charge across the neuron's membrane and is calculated based upon the extracellular and intracellular ion composition. The neuron is surrounded by a semi-permeable membrane that have ion channels that only allow specific ions to cross. Initially, these concentrations are balanced and there is a no net charge. However, any difference of charge across this membrane can result in the generation of action potentials.

During the quiescent state, these ion channels are closed, and the ions are distributed across the membrane in such a way that the extracellular fluid is largely

composed of sodium ions (Na^+) and the intracellular fluid with potassium ions (K^+). This results in a negative concentration gradient of about -70mV known as the resting membrane potential. When the cell is triggered, these voltage-gated channels begin to open, and they allow an influx of Na^+ ions due to the concentration gradient. Subsequently, this causes the cell to depolarize and moves the membrane potential closer to 0mV . When a threshold of about -55mV is reached, an explosion of electrical activity occurs, resulting in neural firing of action potentials of a fixed size. This prompts all the available Na^+ channels to open and permits more Na^+ to enter the cells, resulting in a reversal of the membrane potential. Now, when the potential reaches $+30\text{mV}$, the channels specific to potassium ions are activated, causing a relatively slower outflux of K^+ ions. At this stage, the sodium channels close. The outflow of positive charges restores the electrochemical gradient to the resting state. The repolarization process ends with the closure of the potassium channels, before the resting membrane potential is reached. However, these channels face a delay in attaining full closure. This hyperpolarizes the cell to a more negative potential, thereby producing a small overshoot as seen in Figure 2. Now the active transport is kickstarted to bring the membrane conditions back to the resting state and prepare the cell for the next action potential. This propagation of the action potential applies to an unmyelinated axon and is referred to as a continuous conduction. For myelinated axons, a faster process namely saltatory conduction takes place. As the voltage gated channels are only present at the nodes of Ranvier, the continual process of opening the channels along the axon is eliminated and the action potential jumps from one node to the next.

A distinguishing feature of the action potential is its 'all or none' nature. Hence, the strength of response of the nerve cell is independent of the strength of the stimulus. If the membrane potential fails to reach the threshold, no action potentials are fired.

Another feature is its frequency of activation. An action potential cannot be initiated when one is already under progress. This is determined by the refractory periods of the action potential. During the absolute refractory period, it is impossible to start another action potential, due to the closure of Na^+ channels. In the refractory period, a new action potential can be generated if a stronger stimulus is provided.[2]

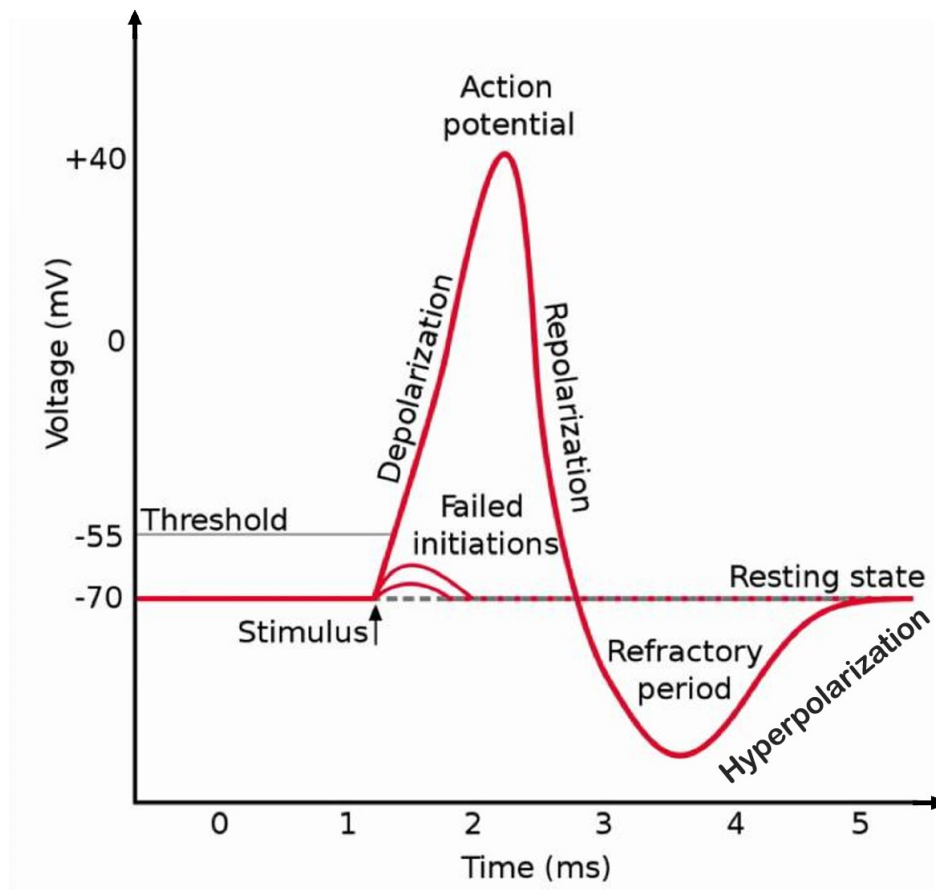


Figure 2. Action Potential: Diagram depicting the generation of an action potential. Adapted from [108]

The entire process from the initiation at the initial segment and its travel down the length of the axon till the synapse takes place within 5 ms.[2] At the axon terminals of the presynaptic neuron (neuron that is sending information), neurotransmitters are released and it is absorbed by the dendrites of the postsynaptic neuron (one that is receiving information), resulting in its sufficient depolarization for generating an action potential in the postsynaptic cell. Basically, the output of the neuron is the secretion of

the neurotransmitter at the synapse. This is received by the receptor, thus forming a unidirectional connection. This chain reaction continues till the stimuli is received by the targeted cell.

While the presence of chemical neurotransmitters can instigate an action potential, an alternative, namely neural stimulation, taps into the electrical features of the nervous system. This viable solution induces action potential firing through electrical stimulation in a localized manner. Moreover, the ability to generate an instantaneous response upon activation and reverse it when the stimulation is disabled proves to be an added advantage over the chemical component. Neural stimulation can use various modalities aside from electrical stimulation, such as magnetic, light and sound stimulation. All these methods subsume under the umbrella of neuromodulation. According to the International Neuromodulation Society, neuromodulation can be defined as ‘the alteration or modulation of nerve activity by delivering electrical or pharmaceutical agents directly to a target area.’ [3] However, the thesis is focussed on a novel neuromodulation technique through electrical stimulation.

1.2 Neural Prostheses

Neuroelectric stimulation plays an essential role in the restoration or replacement of lost neural functions. Neural prostheses work on this principle of artificial stimulation and involve electrodes to interface with the nervous system for re-establishing these functions. They act as a substitute for a modality that has been damaged due to an injury or disease. A few examples of chronically implanted prostheses are pacemakers, cochlear implants, deep brain stimulators, and spinal cord stimulators. Two critical metrics used to define a neural stimulator is safety and efficacy. Safety deals with the prevention of tissue damage and electrode corrosion,

while efficacy relates to the ability of the stimulator to evoke the desired responses, be it excitation or suppression of the action potentials. [4]

The mechanism of electrical stimulation entails membrane depolarization of the excitable tissue through the flow of ionic current between two or more electrodes placed in close proximity of the neural tissue. Current devices employ a series of charge-balanced, biphasic current pulses or other forms of alternating current. These pulses have an anodal and cathodal phase with equal but opposite amplitude polarities that ensures a net zero charge for that pulse. The anodal and cathodal currents result in oxidation and reduction reactions at the stimulation electrode respectively. [5] While the charge-balanced feature of these waveforms plays a part in the deterrence of toxic substance formation at the electrode-saline interface owing to the electrochemical reactions, these devices can only excite the intended neural tissue. With the goal of reducing the action potential firing in mind, these prostheses function through two methods; lateral inhibition or use of high frequency pulse trains. The former engages in an indirect method of inhibition through the excitation of neurons that in turn suppresses the activity of the target neuron itself. [6] Without these set of neurons, inhibition is not possible. Another technique through which action potential propagation is terminated is through the formation of a nerve block by using high frequency, biphasic pulsatile stimulation. However, prior to the application of the stimulation waveform, a comparatively long-lasting, and high-firing rate phase occurs.[7] Thus, these AC neuroelectric prostheses face an immense drawback when they are compelled to inhibit the neural activity. This invokes the need of a neural prosthesis that can both excite and inhibit the neural activity.

1.2 Safe Direct Current Stimulator Technology

A promising solution to this dilemma inspired by the operation of transcranial direct current stimulator is described here. The benefits of using direct current (DC) over pulsatile stimuli for neuromodulation has led to recent advancements in this field. The modulation of neural activity transpires because of the changes in the transmembrane potential by the external neural electrodes. The cathode (negative electrode) induces depolarization, while anode (positive electrode) engenders hyperpolarization. [8] This presents itself as the foundation for the primary advantage of DC, which is its ability to directly inhibit the neural activity. While the anodic DC decreases the conduction velocity of these action potentials and reduces the firing rate, cathodic DC establishes excitatory effects such as an increase in the firing rate and sensitivity of the neurons.[9] Moreover, DC has the added advantage of possessing zero frequency, which deters the phase locking of neural firing to the stimulation frequency. Besides these significant advantages, the use of DC violates the safety metric of a neural stimulator. The standard electrodes used for stimulation are metallic in nature. When the electrode is placed in contact with the neural tissue, an electrode-electrolyte interface is formed. Electrons are responsible for conducting charges in the metal electrode phase, while in the physiological medium, ions carry the charge. Hence, transduction of charge carriers from electrons to ions occurs. Although faradaic processes of reduction and oxidation can be used as a method of charge transfer, it results in the formation of irreversible, toxic products that would eventually corrode the metal surface, and cause changes in the chemical environment surrounding the neurons. A parameter used to keep this in check is the charge injection limit, which denotes the amount of charge that can be transferred across the interface without causing irreversible chemical reactions. Since DC is unidirectional, the safe charge injection

limit is violated. This impediment confines the use of DC to acute laboratory experiments. Overall, direct current provides a can be used to excite, inhibit or modulate the sensitivity of the neurons.

By addressing the concern of safety, the utility of DC can be extended to a wide range of neuroprosthetic applications. Inspiration was drawn from Spelman *et al.*'s work of switching mechanical valves in phase with the stimulating biphasic square waves to deliver ionic DC to the target nerve tissue. This laid the foundation behind the Safe Direct Current Stimulation (SDCS) technology. It aims to safely deliver DC to the neural tissue without adverse reactions occurring at the electrode-electrolyte interface. This is resolved by passing alternating current (AC) through the electrode-electrolyte interface for maintaining the charge injection limit, to a fluid switching network that rectifies it into ionic direct current (iDC), as seen in Figure 3. The iDC is then, in principle, supplied to the tissue through a purely ionic interface, eliminating risks involved with the electrode-electrolyte interfaces. A benchtop setup of the same proved the viability of this procedure to excite and inhibit neural tissue. The first implementation of this procedure, a benchtop setup with hand-operated valves, is denoted as SDCS1. The AC signal prompted the valves to switch states (ie, from open to close and close to open) for each phase. This resulted in a unidirectional ionic current flow through the stimulated tissue. While SDCS1 verified the viability of this procedure to excite and inhibit neural tissue, its large stature and non-ideal valves led to periodic interruptions in the current flow to occur. These disruptions induced unavoidable neural activity with each valve transition. To compensate for this, a second prototype, namely SDCS2, was developed. SDCS2 integrates two SDCS systems as seen in the Figure 4; one system switches the valve states to ensure rectification and the other drives the ionic current through the tissue. Since a proof-of-concept large-scale implementation was

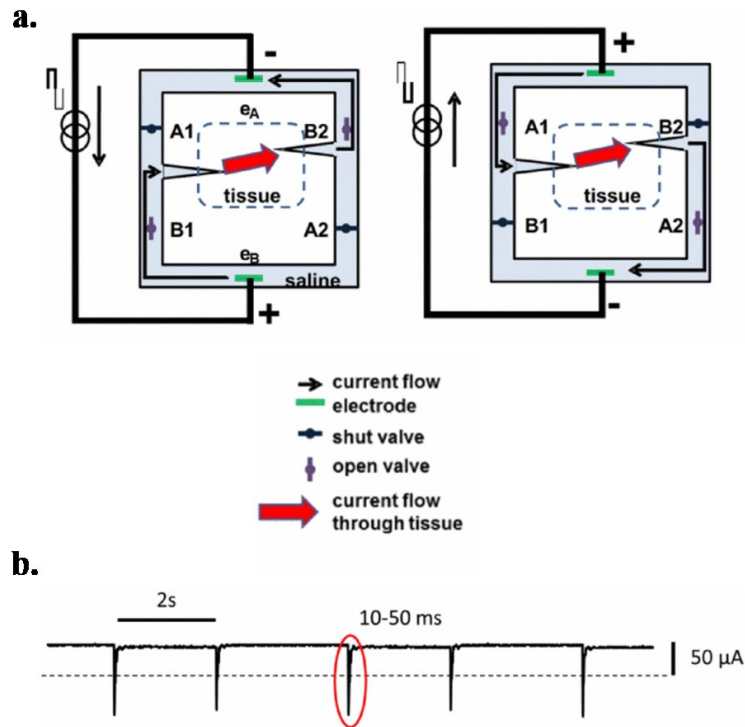


Figure 3. SDCS 1 Design: (a) This depicts the proposed design for SDCS1. It shows two states of the same device. Although the electrodes switch polarities, the current through the tissue remains unidirectional. Hence, iDC is delivered to the tissue. (b) This represents the output current of SDCS1. It can be observed that there are interruptions in the current during valve transitioning. Adapted from [109]

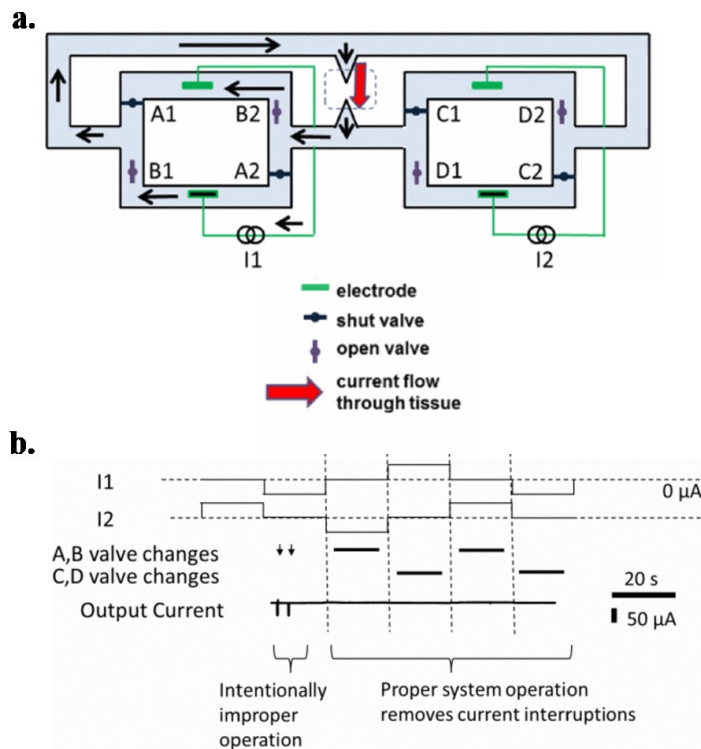


Figure 4. SDCS 2 Design: (a) This depicts the proposed design for SDCS2. It shows the flow of current during a single valve configuration. (b) This shows the output current and the corresponding state changes that occur in SDCS2. Adapted from [110]

established with a series of manually-operated valves and tubes, the next step is focused on designing a miniaturised functional prototype.

Currently, the SDCS device can be divided into four functional layers as delineated in Figure 5: safe DC microfluidics, safe DC electronics, application specific electronics, and power. The first layer is responsible for the rectification of the charge-balanced pulses into iDC. While there are a number of mechanisms through which rectification can be achieved, the requirement of an implantable device imposes constraints, specifically in terms of its size and power consumption. The simplest arrangement that could still perform effectively in a miniature scale were a system of valves with an autonomous actuation mechanism. The various actuators and their advantages and disadvantages are discussed in the upcoming chapter. Among these, the shape-memory alloy-based actuation surpassed other mechanisms in terms of its quick response times, ease of handling and potential longevity. Hence, an isolated fluid network is used for obtaining a rectified ionic current. Accordingly, an ideal miniature valve design using the shape-memory alloy for actuation should fulfil two main criteria;

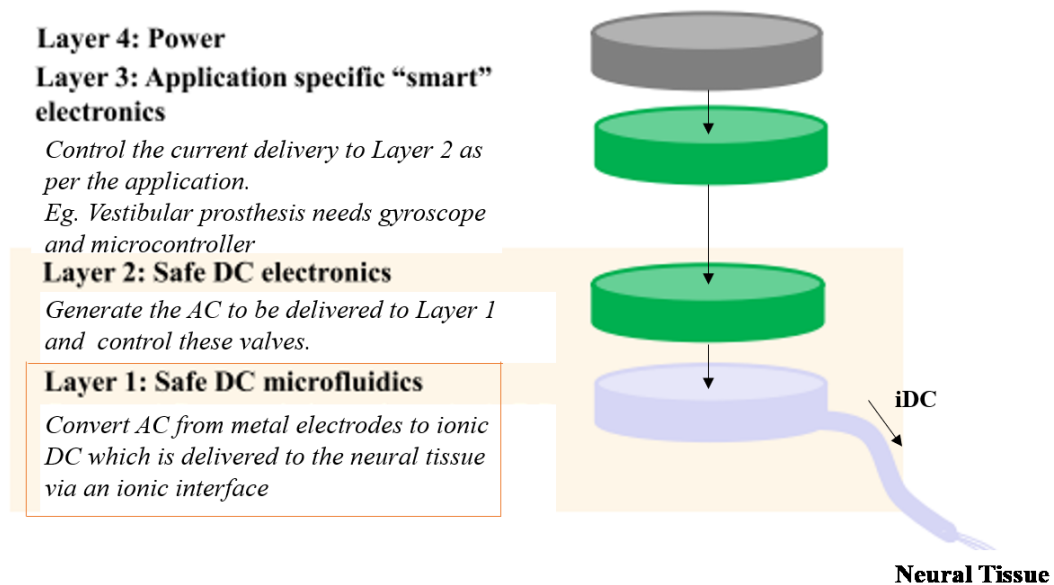


Figure 5. Functional Layers of SDCS Device: The SDCS device can be delineated into different layers. The focus of the thesis is on Layer1, the microfluidics and interface to the nerve for SDCS. Adapted from [111]

a low force to open/close (based on initial valve configuration) and a small linear displacement for achieving the same. Aside from the valves, layer 1 also includes the electrode-tissue interface. Since iDC is to be delivered to the tissue, a purely ionic interface is necessary for safe stimulation. The electronics layer is split into two; layer 2 contains the basic underlying circuitry for the device. It includes circuitry for the systematic operation of valves and for delivering AC to the microfluidic layer and layer 3 deals with circuitry needed for the particular SDCS application. The last layer powers the entire device, ideally through a rechargeable battery or wirelessly.

1.4 Thesis Overview

This novel neuromodulation technology seeks to dramatically improve the treatment of many prevalent neurological deficits. On-going research delves deep into the use of SDCS for chronic pain and asthma attack suppression and as a vestibular prosthesis for balance restoration. This thesis emphasizes on the development of a microfluidic device that can deliver iDC to the target tissue in a safe and reliable way, particularly for the chronic pain application. The prior work undergone in the microfluidic platform for SDCS is illustrated in Figure 6 (left) and Figure 7 (left). Figure 6 demonstrates the various iterations undertaken for designing a miniature valve, which would be a part of the rectifying fluidic network. Figure 6 (left) displays the initial two valve designs which were taken into consideration. The normally-open pinch/squeeze valve has a rectangular channel that is ‘pinched’ close by the contraction of the nitinol wire. However, inefficient valve closure occurred, since a larger pull force of the wire was required to compress the bulk substrate around the valve rather than attaining closure. The next design was a two-layer normally-open ‘gated’ microvalve. Closure was obtained by indirectly compressing the elastomer, using a ‘gate’. A cylindrical/triangular ‘gate’ was placed on the top layer and the shape-memory alloy

wire was looped over this. Contraction of the wire would cause force the top layer to be pulled downwards. This allowed the ‘gate’ to fit exactly in the curve of the channel, resulting in valve closure. Although smaller forces were lost to compressing the bulk, a larger displacement was still required. This design formed the basis of our plunger-membrane microvalve architecture as seen in Figure 6 (middle), which is described in depth in the upcoming chapters. Once the valve design is optimized, the next step would involve the implementation of a full 8-valve SDCS system.

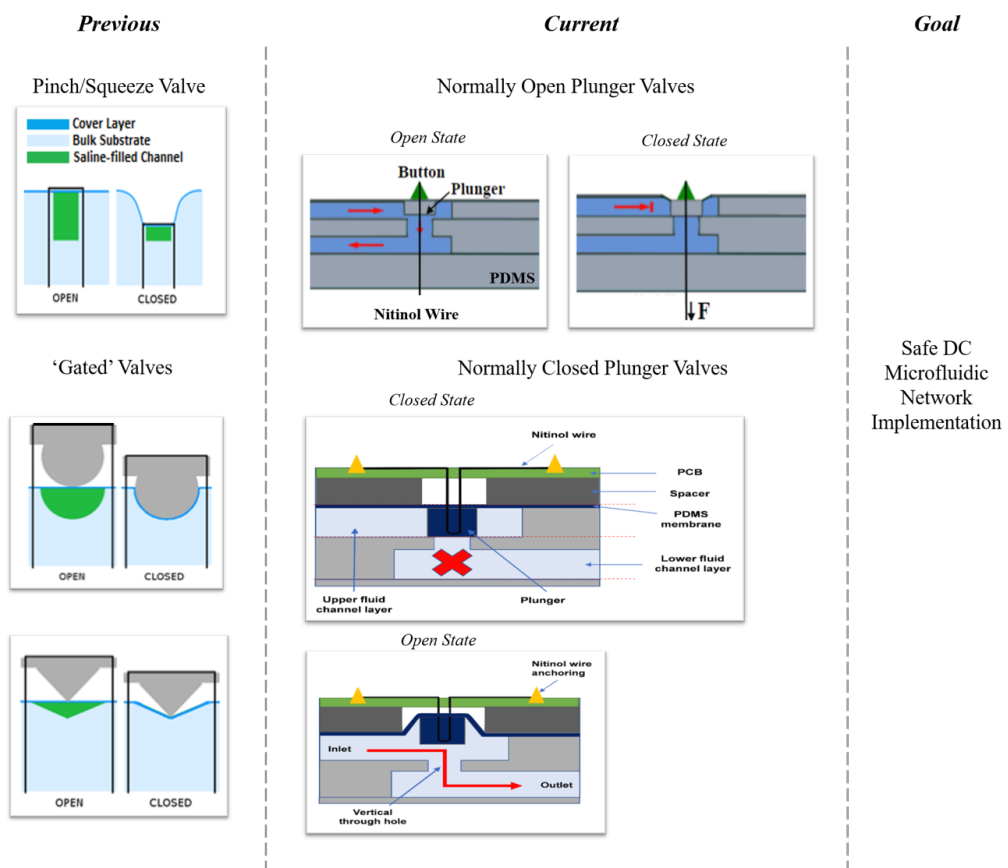


Figure 6. Microvalve Design Iterations: The multiple valve design iterations are shown. The **left** column represents the previous work undertaken in valve design. The **middle** column depicts our iteration to the preceding design, whose development and testing would be described in this thesis. The **right** column embodies the next step that has to be achieved for successful realization of an implantable SDCS device.

The electrode design for SDCS is specific to the application. Figure 7 illustrates the electrodes utilized for interfacing the fluidic system of valves with the neural tissue, in order to deliver the ionic current for suppressing pain. Figure 7 (left) depicts the

currently used micropipette electrode with a 200um channel that is filled with an agar-saline solution and was used for *in-vivo* experimentation. For pain suppression, an interface that would direct the current into the nerve, with limited current spread along the surface of the nerve is required. These *in-vivo* experiments involves positioning the electrode on the nerve in mineral oil, which provides an insulation and prevents the current spread. However, this option is not available for long-term implants. Hence, the micropipette electrode is a rudimentary design, which has to be iterated upon. Although these electrodes are suitable for acute experiments, several concerns based on optimizing the design, the ionic conductive medium, the material of the electrode and its contacts, the orientation and distance between the electrode contacts and many more must be addressed. Thus, I designed and tested the cuff-clamp lead system, shown in Figure 7 (middle) for conformability with the design criteria and this will be detailed in

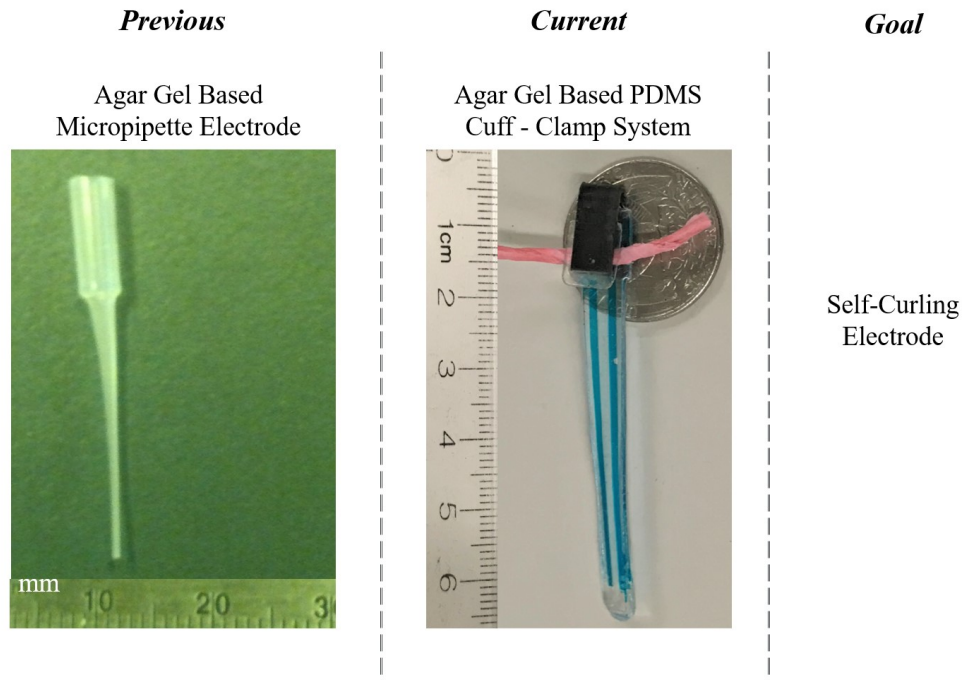


Figure 7. Neural Interface Design Iterations: This figure depicts the various electrode designs taken into consideration for interfacing the microfluidic network with the neural tissue. The figure on the **left** is a micropipette filled with an agar-saline solution, that is currently used for *in-vivo* experiments. The **middle** figure is a PDMS based cuff electrode (placed on a quarter for size comparison) and will be described in the coming sections. The **right** figure represents the goal we are trying to reach for this project.

the following chapters. The Figure 7 (right) represents our vision of a neural interface that can be used for ionic current delivery.

In chapter 2, various techniques for the development of microfluidics is discussed. Chapter 3 focuses on the implementation and testing of the microfluidics for the SDCS device. Lastly, chapter 4 emphasises on the design and development of a potential electrode for delivering the iDC to the tissue.

CHAPTER 2: MANUFACTURING TECHNOLOGIES FOR MICROFLUIDICS

2.1 Introduction

One of the key driving factors in the successful realization of the SDCS technology as a neural prosthesis is miniaturization. The proof-of-concept SDCS prototype consists of a tubing network that conducts ionic direct current through the switching of mechanical valves. With the goal of transforming the current bench-top SDCS prototype to an implantable device, a substantial innovation in valve design is needed in order to reduce the power consumption and footprint of the desired implant. [10] A fundamental step towards the successful miniaturization and commercialization of SDCS is the development of reliable microfluidic valves or microvalves. This downsizing is also contingent on the actuation and interfacing elements that control these valves. As a multitude of actuation principles can be adopted to actuate these microvalves, their design and actuation mechanism is chosen based on the suitability with the given application. A low power consumption, hermeticity, rapid response time, compatibility, high valve conductance, and high reliability are some of the desired characteristics imperative for miniature valve design for SDCS. Thus, the fabrication methodology plays a major role in the successful implementation of microvalves by addressing some of the above mentioned hurdles along with the reliability, energy efficiency and cost requirements.[11] [12]

Currently, numerous valves are designed to have a membrane or diaphragm that is actively actuated.[13] One particular type of active valve, namely the elastomeric plunger-membrane microvalves has been a cornerstone technology for enabling various applications of microfluidic devices in bioanalytical instrumentation [10]. The focus of this thesis chapter will be on miniature plunger valves that are made from elastomeric materials.

Characteristics of PDMS

A popular material widely used in microfluidic devices is polydimethylsiloxane (PDMS). This silicone based viscoelastic polymer is an optically transparent, biocompatible, and flexible material that can be rapidly prototyped via soft lithography.[14] [15] Since PDMS is an elastomer, it will easily conform to the surface of the substrate. Additionally, the surface properties of PDMS can be easily modified by surface treatments. The Young's modulus of PDMS (~750kPa) [16] is three orders of magnitude smaller than that of hard plastics, therefore allowing PDMS based valves to be built smaller and faster. Some other properties include its low cost, non-toxic nature, stability against temperature variations and its low interfacial energy that prevents chemical interactions with other polymers and fluid solutions in the microfluidic channels. Due to these unique properties, PDMS is instrumental in the formation of high-quality patterns and structures that would be required for developing the microvalve prototypes. [11]

2.2 Fabrication Techniques for Elastomeric Structures

These small-scale microfluidic devices would entail high precision micromachining techniques for creating high aspect ratio structures. Due to the lack of a universal, inexpensive and reliable fabrication technology for microfluidics, the market emergence of microfluidic platforms has been slow. Each of the distinct fabrication processes has its advantages and disadvantages and selecting the manufacturing method which is best suited for the application involves several trade-offs or multiple hybrid processes. [17] As this thesis strives to accomplish the course undertaken to produce miniature valves, a hybrid process encompassing both additive

manufacturing for hard molding followed by a soft lithographic process to create the PDMS chips would capitalize on the advantages of both.

2.2.1 Soft Lithographic Process

Soft lithography, a well-developed non-photolithographic silicon-based process is one of the frequently used practices for elastomeric microfabrication. Together, PDMS and soft lithography have started a revolution in the microfluidic community due to their low infrastructure costs and ease of manufacture.[18] In this procedure, microfabrication is carried out via self-assembly and replica molding. [19] Although, this conventional process for creating a PDMS based microstructure follows a standard procedure and is easily implemented without the use of expensive fabrication equipment or clean room facilities, it is a cumbersome process for mass-production manufacturing as it involves a series of steps. [20] There are multiple soft-lithography methods that are adopted presently, particularly microcontact printing (μ CP), replica molding (REM), microtransfer molding (μ TM), micromolding in capillaries (MIMIC) and solvent-assisted micromolding (SAMIM). [19] Collectively, they are known as soft lithography techniques as they follow the basic principle of replicating the patterned structures defined in an elastomeric stamp or mold onto the substrate or master mold, which is typically made of a soft elastomer such as PDMS. This procedure follows the same stages as common photolithography; designing the shadow mask and PDMS based stamps, and production of well-defined templates before molding the stamp on. [16] Complications arise with this process for the fabrication of complex, multi-layer devices. Multi-layer devices would require tedious manual labor for stacking, aligning and bonding of the multiple layers, thereby reducing the range of features that can be created on these molds.[18] Furthermore, this technique builds the 3D architecture by stacking 2D layers, which requires further patterning and bonding steps, increasing the

processing costs and reducing the success rates. [18] As this procedure involves several supplementary methods and involves substantial human labor, an alternative procedure should be surveyed for designing the templates.

2.2.2 3D Printing Technology

A more efficient procedure for template prototyping that is currently emerging is 3D-printing technology. 3D printing is “the fabrication of objects through the deposition of a material by using a print head, nozzle or other printer technology,” as defined by the ASTM International Committee. It is considered to be a ‘solid freeform fabrication’ technique that belongs to a family of additive-based manufacturing technology.[21][22] It is highly integrated with other supporting technologies such as computer-aided design (CAD) and computer-aided manufacturing (CAM). The advantage of 3D printing over the typical technologies is two-fold. It provides an automated method to fabricate three-dimensional structures, thereby eliminating the need of extensive manual processes that had rendered commercialization difficult. This allowed for an unprecedented expansion into the field of microfluidics. Another significant feature is its rapid realization and fabrication of the model under consideration. Depending on the size of the model and complexity of the structure, each microfluidic chip would take anywhere from 10 minutes to hours to be fabricated. This leads to an approach that is regularly adopted by researchers, called a ‘fail fast and often’ strategy. Moreover, the possibility of designing a range of sizes and utilizing various materials garnered the attention of microfluidic device developers.[23] Despite these benefits, there are some universal concerns regarding the resolution of the structures produced, biocompatibility, material availability, shape conformity, and optical transparency. With the focus of this thesis targeted on microvalves, the choice

of fabrication technology should primarily encompass the following features: inherently fast, inexpensive and highly reliable. [18]

History of 3D printing

The earliest 3D printing technologies emerged in the 1980s and were then known as Rapid Prototyping (RP) technologies. These RP processes were quick, automated, and cost-effective procedures for developing product prototypes. The origins of 3D printing can be traced back to Charles Hull, who first constructed a stereolithography apparatus (SLA) in 1983. This device used UV light to cure a photopolymer resin to make the required prototypes. The software slices the 3D object into layers of thicknesses specified by the resolution of the printer and the machine stacks these layers over each other to form the part. Hull faced an issue in translating the CAD file into a format that is easily interpreted by the printer. He, thereafter, developed the stereolithography (STL) file format that is currently used.

Throughout this period, new technologies continued to be introduced which were mainly focused on industrial applications. Scott Crump founded the Fused Deposition Modelling (FDM) process in 1989, along with the acrylonitrile butadiene styrene (ABS) material that is widely used by 3D printers today. Parallel to the advancement of the SLA device, Carl Deckard developed another RP process, namely the Selective Laser Sintering (SLS). SLS and FDM printers were used to create plastic and nylon parts. The SLS printer was also the sole technology that could make prototyping parts in metals. Soon after, in the 1990s, Massachusetts Institute of Technology invented the inkjet 3D printing process. Through the 2000s, an exponential rise in the use of 3D printer technology was observed. The availability of open-source hardware and software has garnered a huge consumer base for such technology.[22][24]

Types of 3D Printing Processes

The need for a commercialization ready, environmentally friendly and economically efficient fabrication procedure resulted in several advancements in the field of 3D printing leading to a wide array of commercial systems.[23] However, not all these processes are suitable for the microfluidic applications as they are unable to create minute structures and have a poor resolution. Commonly used 3D technologies for microfluidics include SLS, FDM, photopolymer inkjet printing, laminated object manufacturing (LOM), SLA and DLP.

Selective Laser Sintering

This additive manufacturing technique utilizes a high-power laser to build the 3D object. In this case, the precursor material can be a blend of polymers in the powder form. Each layer is defined by the heating of the powdered material on the build plate that causes a fusion of small particles of the material into a mass with the desired shape. This thermal treatment is called sintering. SLS is a rapid prototyping technique used to obtain a highly pure print. As this technology requires a high-powered laser, the printer itself is expensive.[23]

Fused Deposition Modeling

FDM, also known as thermoplastic extrusion, works by melting a continuous plastic filament that is fed through a heated extruder, layer by layer, on the build platform. As the layer is deposited, it hardens and bonds to the previous layer.[24] It enables the printing of biocompatible polymers such as ABS, poly (lactic acid) (PLA), polyamide, polystyrene and polycarbonate. The prints have a good thermal and mechanical resistance.[25] However, they are prone to stress fractures as the filaments from adjacent layers may not be bonded properly and would require additional support

structures. Moreover, the melting of plastics at high temperatures leads to the generation of fumes, which poses a health hazard.

Photopolymer Inkjet Printing

In this process, the build materials in their liquid or molten state are jetted onto a build platform via the inkjet print heads. UV lamps are then used to cure the material and causes it to solidify on the build plate layer-by-layer. A range of materials, from soft and hard plastics to elastomers can be printed by this mechanism. Nevertheless, these supplies are expensive and have limited mechanical properties and low durability.[26]

Laminated Object Manufacturing

This low-cost technique stacks and bonds layers of adhesive-coated paper, plastic, or metal laminates through the application of heat or pressure. The desired shape is then cut using a computer controlled knife.[25] While the adhesive or chemical bonding prevents the layers from detaching and fashioning a sturdy model, [23] these models are relatively larger in size.[25]

Stereolithography

SLA is a laser-based process that utilizes photopolymer resins. Parts are created through a layer-by-layer mechanism, wherein the build platform is lowered into a vat containing the liquid photopolymer. Each layer is ‘drawn’ by the laser and is created by the deposition of a continuous stream of filament. A UV laser scans the surface of the vat and in turn causes polymerization of the resin and by this means solidifying it on the build plate. This process results in a very accurate representation of the model with a smoother surface finish and complex detailing. Nonetheless, as it only works with photopolymers, it does not have very well-defined mechanical properties.[24]

Digital Light Processing

This process is very similar to stereolithography as it also works with photo-reactive polymers. The light sources used are mainly conventional sources of lights like arc lamps. Based on the SLA process, a high resolution projector is placed below the resin container and the light pattern powered by the DLP technology projects an entire layer or slice of the 3D object on the build plate. The liquid resin is placed in a transparent vat and when light incidents on it, the resin hardens on the build plate that is lowered into the vat.

This method of printing has excellent resolution and much lesser resin material is required for the production of details in the part, leading to a lower cost and less waste when compared to the SLA process. Furthermore, as the projector or light source remains stationary, there are only a few moving parts, which decreases the maintenance costs. [25] DLP based printing is quicker than its counterpart, since the profile of the entire layer is projected on the build plate, ensuing the conversion of a 2D image into a 3D object. However, with the SLA printer, a 1-dimensional drawing process is followed, wherein each cross-sectional layer is broken down into a series of points and lines that is traced by the laser, resulting in a slower process with possibilites of inaccuracies occuring that would adversely affect the structural strength and surface finish of the print.[27]

Due to these particular strengths, a machine that utilises the DLP methodology is opted for the production of the valve molds. Among the various DLP based printers available, the B9 Creator (B9 Creations, South Dakota) is opted for, as it is relatively faster than other resin based 3D printers and the proprietary resin is less expensive. Besides these advantages, the foremost benefit is the accessibility to a range of

resolutions, which is otherwise not provided by other DLP printers.[28] The printer provides a resolution of 30, 50 or 70 microns along the XY-plane and can go as low as 5 microns in the Z-plane ensuing highly reliable and accurate printing of miniature valves. The B9 Creator utilizes a UV projector as a light source. In addition to this, the printer works with various photopolymer resins; red, black, cherry, emerald, and yellow resins. The resin to be used is chosen as per the desired application. The B9 Cherry, Emerald and Yellow resins are adopted for casting purposes. The Black and Red resins are used for prototyping as they develop accurate, strong and temperature resistant molds. The casting resins enable the production of high-resolution and detailed prints, which can be casted in metals such as silver, gold and platinum with high repeatability and flawlessness. The prototyping resins allow for high-speed printing of durable models and molds that are able to withstand high-temperatures, while maintaining its dimensional accuracy and prototyping strengths.[29] These UV curable resins are widely popular currently due to three reasons. First, since these resins are composed of small molecules called photo-initiators that are activated by light, only photochemical cleavage occurs to produce reactive components that are environmental-friendly. Conventional curing is performed by a solvent evaporation technique involving heat and air drying. This causes shrinkage of the resin and creation of environmental pollutants. The absence of a solvent in this resin material results in a nonappearance of pollutants and no loss of volume. [30] Secondly, they are more energy efficient than thermally curable resins. Thirdly, the UV curing process imparts desirable properties to these parts such as improving their mechanical strength, which is otherwise not achieved through thermally cured resins.[31]

Principle

Although different types of 3D printers incorporate distinct technologies that processes different materials, they all follow the same basic process for building prototypes. The steps are as follows:

- Create a Computer Aided Model (CAD) model of the design using software packages like SolidWorks or AutoCAD
- Convert the model to an STL file format. This format represents the 3D object surface as planar triangles and holds the coordinates of the vertices and direction of its outward normal, independent of the software being used for designing the model.
- Slice the file into 2D cross-sectional layers using a pre-processing software. This user interface allows for changing the orientation, scaling factor and slice thickness of the model. The slice thickness is determined by the resolution of the printer and can vary according to the capabilities of the machine. A smaller slice thickness leads to an increased build time but improves the accuracy of the prototype. Another characteristic of this software enables the generation of support structures, which are vital for part features that involve thin-walled sections and internal cavities. Without these, the part may collapse.
- Build the prototype. After the processing of the STL is completed, the file is sent to the printer. The printer then builds the prototype one layer at a time.
- Clean the model. Once the building process is completed, the finished product can be obtained on the build plate. The post-processing step is the removal of the part and cleaning it to eliminate support structures and other contaminants. Further processing involves post-curing of the photosensitive materials and

surface treatment to improve the appearance, durability or for other functionality.[22]

Post Print Curing Processes

Since the parts printed by the DLP based B9 Creator are created by the lowering of the build plate into the resin; once completed, there will be residual resin that has not been fully cured and support structures present. If supports are used, they leave marks on the surface and may create uneven surfaces. Moreover, when the 3D design has small detailed structures that are crucial for the functioning of the object, these residues can hinder its development and thereby render the part non-functional. Thus, a post processing method is required to get rid of these irregularities for producing precise and robust prototypes.

Ultrasonic Cleaning Bath

The initial step after lifting the print from the build plate is ultrasonic cleaning. Generally, the cleaning of the printed part involves manual removal of the residues assisted by a water jet. This process is extremely time consuming, and takes up to 30% of the total production time.[32] An ultrasonic bath ensures a rapid and accurate removal of the support material from the printed item with the use of low temperatures. The object to be cleaned is mixed with a surfactant like soap and placed in the chamber that contains an aqueous solvent. The ultrasonic transducer in the chamber produces high frequency ultrasonic waves by agitating the liquid in the bath and generates millions of microscopic cavitation bubbles.[32] The sound waves engender a powerful ‘scrubbing brush’ action across the surface of the object, including crevices.[33] Due to the huge burst of energy, these vacuum filled bubbles rapidly increase in size and just as quickly implode against the surface and release their energy. This produces a

shear force that breaks the bonds that hold the contaminants to the part, thus cleaning the part [34].

Ultraviolet Curing

Even after the part is cleaned, an additional curing process is required. Although the desired parts are obtained, the polymerization reaction is still underway, and the necessary mechanical properties are not yet achieved. This is finalized through a photochemical process where UV light of 200nm-400nm wavelength is incident on the print, which hardens the resin and improves the strength and stability of the part. The B9 resin is composed of photo initiators, oligomers, and other monomers like acrylates and methacrylates. On incidence with UV light, these photo-initiators undergo a free-radical chemical process to generate radical initiators or catalysts. These by-products induce cross-linking reactions of the functionalized oligomers and monomers to form a sturdier cured product. This process wherein the liquid resin is transformed into a cross-linked polymer due to the conversion of light energy into chemical energy by the photo-initiators is called photopolymerization. [31]

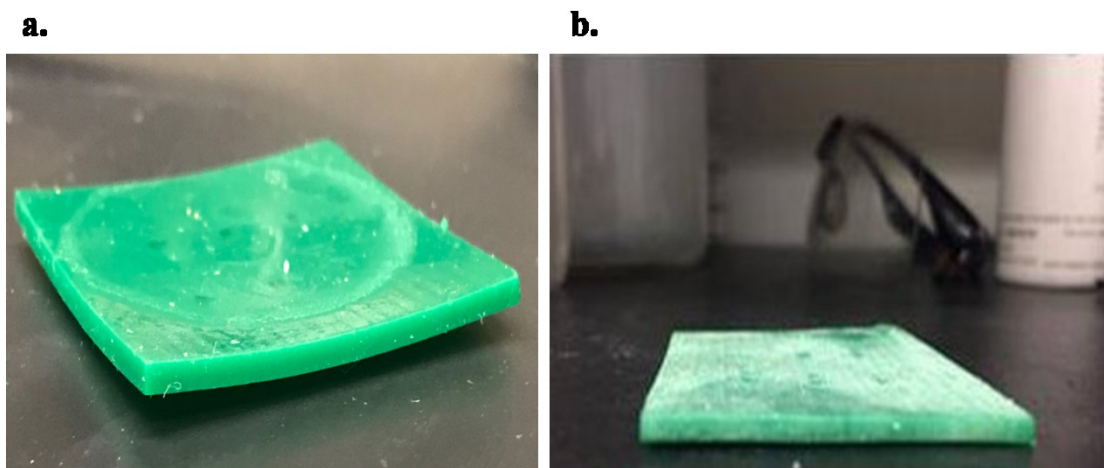


Figure 8. UV Curing of 3D Printed Molds: (a) A mold that was UV cured and shows warping of the edges. **(b)** A mold that was placed underwater and then UV cured showing an almost flat surface.

However, when this process was done in the open air, notable curving or warping of the edges of the print was observed as seen in Figure 8(a). This is due to the

oxygen present in the atmosphere that hinders the free-radical polymerization process. Oxygen reacts with the by-products of the chemical reaction, which is vital for the polymerization process, thus preventing it. Since the edges are smaller in cross-sectional area when compared to the center, the incidence of UV light would have a greater effect on it. Furthermore, volume contraction and shrinkage occurs that causes the surfaces to bend.[35] [36] Hence, the process is done in the absence of oxygen to obtain a flat surface as seen in Figure 8(b).

There are 3 types of UV light in the electromagnetic spectrum: UV-A (wavelengths = 320-400nm), UV-B (wavelengths = 290-320nm) and UV-C (wavelengths = 200-290nm). The curing lamps utilized in this procedure emits UV-A light of wavelengths ranging from 340-380nm. As per the electromagnetic spectrum of water, water is strongly absorbed at most of the wavelengths. As seen in Figure 9, the absorption coefficient of water decreases in the UV-A light region indicating that only a limited amount of UV light is absorbed by water. [37]

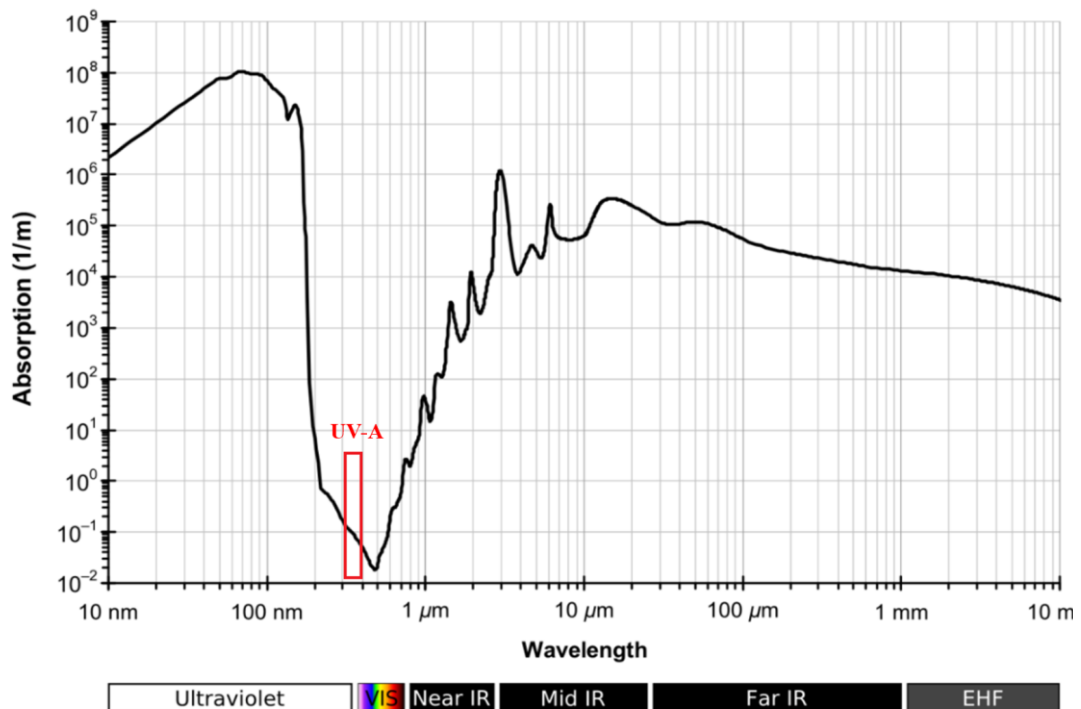


Figure 9. Absorption Spectrum of Water: The absorption spectrum of water as a function of the wavelength of light incident on it. The red box specifies the UV-A wavelength. Adapted from [38]

Moreover, according to Beer's law, the intensity of light penetrating a material decreases exponentially with the distance from the surface. This is expressed by the following equation (1),

$$\frac{I}{I_0} = e^{-\alpha l} \quad (1)$$

where I/I_0 is the fraction of light transmitted through the material, α is the absorption coefficient that is a function of wavelength and l is the length of the light path. From Figure 9, the absorption coefficient of water for UV-A light is between $10^{-1} - 10^{-2}$ per meter. This implies that more UV light can penetrate the material if the length path for the light wave is small. [38]

If the mold is submerged in a deeper dish, more amount of UV-A light is absorbed by water, either preventing the curing process or it would require an extended amount of time for curing. Hence, the mold is placed underwater in a narrow transparent dish and is exposed to UV light for some time. This allows the cross-links to be formed that pull the monomer chains closer to each other very rapidly. During the polymerization, the long-distance connections between the methacrylates, namely Van Der Waals forces are replaced by short and stronger covalent bonds between these monomer units, in this manner creating a fully cured part, as seen in Figure 8(b). However, placing the part underwater for a long time affects the tolerances and details drastically.[39]

2.2.3 Replica Molding of PDMS

Valve molds can be created by following the above steps. To obtain the miniature elastomeric valves, a process known as replica molding is advocated. The replica molding technique is a form of soft lithography procedure that replicates

characteristics, such as the shape, morphology and structures that are present in the master mold. This is done by filling the mold with a prepolymer which cross-links and then the resulting polymer is peeled from the mold.

Preparation of PDMS

PDMS preparation is done using the Sylgard 184 silicone elastomer, which is supplied in a two-part liquid component kit. It consists of a viscous pre-polymer base (part A) and a cross-linking curing agent (part B). The two are ideally mixed together in a 10:1 ratio by weight and can be cured at both room temperature ($RT = 25^{\circ}C$) or at elevated temperatures ($T < 200^{\circ}C$). Temperatures above $200^{\circ}C$ resulted in the thermal decomposition of PDMS. By varying the mixing ratio, distinctive mechanical properties are achieved due to different proportions of cross-linked and non-crosslinked polymers being formed.[40] During mixing, air bubbles are trapped. Hence, the mixture is placed in a vacuum degassing chamber for around 15 minutes, before utilization. [40] After cross-linking, PDMS becomes a hydrophobic elastomer.

Surface Treatment

The process of replica molding is typically carried out by casting the liquid prepolymer over a silicone master rather than a rigid mold. Here, the low surface energy of PDMS comes into play and allows for the quick release of the elastomeric PDMS from its silicone-based master mold. However, this process faces the issue of mechanical deformation of the elastomeric master mold as its flexibility allows for the manipulation of the size and shape of features present on the mold. In the case of 3D printed molds, the master mold is rigid in nature. Thus, appropriate surface treatment is required to enable the quick release. This is accomplished by performing a silanization process on the mold. The photopolymer resin used to create the mold is

hydrophilic in nature and hence, PDMS which is hydrophobic, will have a strong affinity to it, making it arduous to peel off the elastomer. The mold is placed in a dish and few drops of trimethylchlorosilane (TMCS) are added. Through vapor deposition, the mold is made hydrophobic for a while, effectively allowing for easy release.

Multi-layer Assembly

A significant benefit PDMS is the ability of bonding the surfaces to itself without the use of any adhesives. Assembling multi-layered PDMS structures is established by creating a permanent bond between the layers by activating the surfaces with oxygen plasma treatment. The typically used vacuum plasma systems are bulky, expensive and require high maintenance. Therefore, a simpler and more economical means of surface activation is preferred. This led to the development of an inexpensive, effective, and portable hand-held corona treater. [41]

Corona treatment is a type of plasma surface treatment that is used to modify surfaces and increase their surface energy. The corona plasma is generated in room temperature at atmospheric pressure, without requiring additional vacuum pumps or gas cylinders. This low temperature process is conducted by the application of a high voltage to a small diameter electrode tip. This results in a visible and localized 'plasma curtain' called corona discharge being created by the ionization of the air around it. The stable corona discharge surrounding the electrode tip is passed repeatedly over the entire cross-section of the PDMS surface for 5 to 20 seconds, which depends on the size of the surface. When this electric field is applied on the PDMS surface, a bombardment of ions on the surface causes its inherent chemical properties to change, thereby making the PDMS hydrophilic. The different layers are then pressed together and left undisturbed to ensure complete bonding. The effectiveness of this procedure is

verified by contact angle measurements, since the plasma dose is directly proportional to the contact angle reduction of deionized water on PDMS. It is observed that with corona treatment, the contact angles varied from its inherent value of 105° to close to 0° . [41] With smaller contact angles, the PDMS surfaces bonded solidly. The presence of contaminants on the surface can derail the bonding process.

By weighing the pros and cons of the various techniques that can be used to fabricate a multi-layered valve, it is seen that a hybrid process works best. Thus, by following the sequential steps of fabrication as seen in Figure 10, a well-bonded, multi-layer, elastomeric miniature valve can be manufactured.

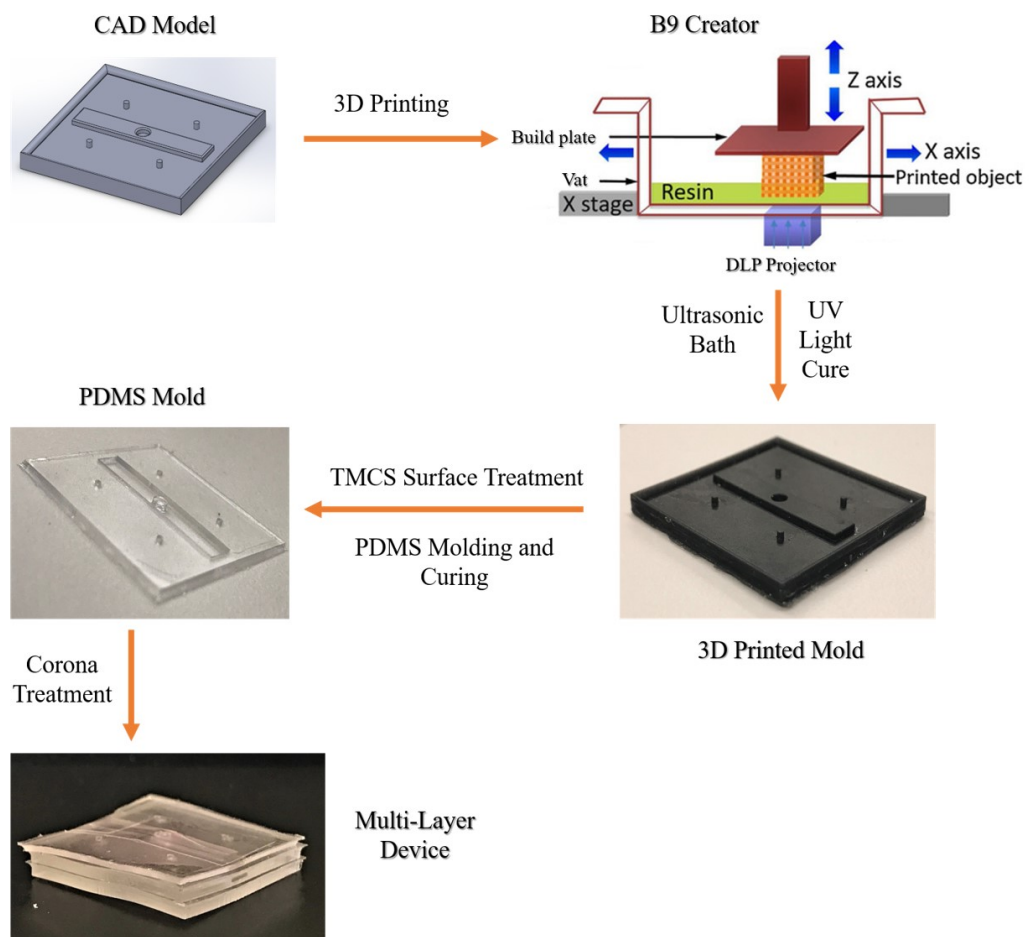


Figure 10. Fabrication Process of PDMS Valves: The flowchart depicts the fabrication process undertaken to produce elastomeric valves.

CHAPTER 3: MICROFLUIDICS FOR SDCS

3.1 History of Microvalves

Although the development of microfluidics started as early as the 1970s, commercialization of these microfluidic valves began only with the introduction of the soft lithographic techniques in the late 1990s. Historically, one of the very first micro-machined valves was a magnetically-actuated, solenoid plunger valve designed by *Terry et al* in 1978 for use in gas chromatography. [42][43][44] These valves were operated by actuating a thin silicon diaphragm that sealed the fluid flow in the microchannel with the help of a solenoid.[44] After a decade, a microvalve was designed that needed no electromechanical actuation. Instead, the disturbances in the inlet pressure and the fluidic pressure on the top and bottom surface of the membrane gave rise to the design of a constant flow-rate valve. [43][45] Since the actuation schemes available at that period were incapable of generating enough mechanical force to actuate the valve, in 1990, *Huff et al* introduced a pressure-balancing strategy in order to augment these forces. This design emphasizes on the balancing force provided on the mobile element of the valve by the fluid pressure. The mobile element here is a plunger, which is composed of a circular base and cap. The fluid pressure simultaneously provides an upward force on the plunger cap, tending to close the valve and a downward force on the plunger plate causing the valve to open. Hence, the actuation scheme, in this case electrostatic actuation, requires only a small force to open the valve. [46] The first commercially available microvalve was based on a thermal-pneumatic actuator system.[45] Soon after, microvalve array systems were fabricated that used electrostatic actuators. Since then, a myriad of microvalves have been manufactured for different applications. The boost in fabrication technology for

microfluidics in the recent years have shown an increase in the number of such systems that have been developed for point-of-care diagnostics.[10]

However, the miniaturization and commercialization of these microfluidic systems are far overdue because of the emergence of new challenges in their production. From a practical viewpoint, the lack of reliable and low-cost microfluidic components, especially microvalves, have hindered the progression of such devices in the healthcare industry. [47][48] In order for these miniature valves to accurately meter flows, certain specifications are to be satisfied by the valve.

- i. *Leak Rate*: This term refers to the rate of leakage of the valve. An ideal valve, when open, would allow a fluid flow and prevent leakage when it is closed. The leakage rate can be denoted as follows from equation (2),

$$LR = \frac{Q_c}{Q_o} \quad (2)$$

where Q_c and Q_o are the flow rates in the closed and open state respectively during a constant pressure operation of the valve. [44] However, the construction of valves is laden with defects, which consequentially incites leakage. This calls for measures to be taken for limiting the leakage rate to obtain an efficiently functioning device.

- ii. *Valve Conductance*: This denotes the maximum rate of fluid permitted through the valve. It is also a function of applied pressure, which is a direct consequence of the valve design.
- iii. *Response Time*: In general, the response time is defined as the time taken between actuation of the valve and the signal output. It ranges from hundreds of microseconds or faster to tens of seconds, based on the actuation mechanism. [44]

- iv. *Energy Efficiency*: Since these valves are designed for implementation in portable platforms, a low energy footprint is crucial. This energy requirement also depends on the type of actuator used.
- v. *Actuation Pressure*: An order of decrease in the size of the device results in twice the increase in actuation pressure required to maintain the flow rate. This can be observed in equation (3) for pressure P,

$$P \propto \frac{1}{A} ; P \propto \frac{1}{L^2} \quad (3)$$

where A is the surface area of the valve and L is the length scale. [48]

- vi. *Reliability*: A valve with mechanical parts is considered reliable when it effectively functions over a long duration without any failures. In terms of PDMS based valves, the shelf life of the device is critically shortened by the aging of the polymeric material due to exposure to sunlight and other factors.

General Valve Structure

With these specifications, the general structure of a valve can be built. The basic structure of a valve entails three-layers: a fluidic layer containing the fluidic pathways, an elastomeric membrane which is deformed to manipulate the fluid flow and a control layer to actuate the membrane.[48][49] The deflection of the membrane allows for a change in the initial state of the valve. A valve can be molded into three possible configurations: normally open, normally closed and bi-stable. A valve in the bi-stable configuration can remain in either the open or closed states and the transition between these stages requires only a power input and no energy consumption. [50] Microvalve systems differ based on their geometry, actuation mechanism, material used to form the

membrane, and fabrication technology. Among these factors, the actuation mechanism is widely used as a parameter for classification.

3.2 Microvalve Classification

Within the last 30 years, a multitude of microvalves have emerged that satisfy the criteria mentioned above. Broadly, these microvalves can be categorized into two major groups based on their actuation principle: passive and active microvalves. Further classification involves the use of mechanical or non-mechanical parts and external actuation in the case of active valves. The passive valve operation is maintained with the help of the fluid flow itself. On the other hand, active valves function through an actuation mechanism for permitting, stopping or controlling the fluid flow through the system. [51]

3.2.1 Passive Valves

These microvalves are basically check valves that are used to block the fluidic flow in one direction. Most passive valves function by the action of pressure on mechanical elements that obstruct the passage of the fluid, sanctioning the fluid flow during favorable pressure conditions and remaining closed under the reverse pressure conditions.[52][42] This results in a high flow rate in one direction and a relatively smaller flow rate in the opposite direction. As they do not include any form of actuation, these valves cannot be controlled externally.[53] The passive mechanical valves are generally based on a beam, membrane, spherical ball or other mobile structures that are displaced by this fluid flow caused by the application of a forward pressure. The most commonly used one is a simple system that consists of an elastic beam as the mobile element that blocks an orifice. The fluid pressure applied causes the beam to rise up and let the fluid flow through and in the reverse direction, the beam elastic member seals the orifice, prohibiting the flow.[42][52] The passive non- mechanical valve

system uses surface tension properties and changes in flow resistance due to changes in channel dimensions to control the flow of fluids. [51] The hydrodynamic valve follows this principle. Since this kind of valve has no moving parts, it cannot sustain a back pressure due to which it is normally open. Instead, the opening and closing states of this valve is obtained by the asymmetry in the forward and reverse flows that can be implemented in the valve geometries.[42] Nevertheless, they have extremely slow reaction times and are susceptible to fluid leakages.

3.2.2 Active Valves

The active valves have two major modes; switching mode where the valve either allows the fluid flow and thereby the current flow or it shuts off this flow and a controlling mode, where the valve is coupled with a sensor or microcontroller to control a fixed pressure or fixed flow rate within the system. Most active microvalves have either a beam or membrane that blocks the fluid path when the valve is inactive. The mechanical active microvalve couples a mechanically movable membrane with a type of actuation mechanism, being magnetic, electric, piezoelectric or thermal actuation. In the non-mechanical active system, the flexible membrane is actuated due to the phase change of the smart materials that the system is composed of. [47] External active valves use external bulky systems as a method of actuation. There is no universal actuation mechanism that can fit all the microvalve applications, consequently one can decide on the best method based on the microvalve system requirements.

Valve Actuation Mechanisms

Actuators have several functions for enabling proper valve operation. The actuator needs to provide enough force and displacement for moving the membrane to the desired position. It should also be able to hold the membrane in that necessary position for a particular period. Akin to the valve specifications, certain aspects

regarding the actuation mechanisms also must be addressed for efficient valving process. Actuation pressure plays a vital role in the valve performance. Based on the generated pressures, the actuators can be divided into three categories: high-pressure, medium-pressure and low-pressure actuators.[48] Some examples of these actuator groups are as seen in Figure 11(a): a stack-type piezoelectric actuator engenders a high pressure, pneumatic, shape memory alloy and thermomechanical actuators produces medium pressure and electromagnetic, piezoelectric, electrochemical and chemical actuators belong to the low-pressure group. Besides the intensity of pressure being generated by these actuator procedures, the response time is another such selection criteria. The electrostatic actuators have a value of $t_{\text{response}} < 10^{-4}\text{s}$, which results in a fast switching between the open and closed states. Pneumatic, shape-memory alloys and chemical actuators represent the other end of the spectra with a value $t_{\text{response}} > 1\text{s}$ as seen in Figure 11(b). The energy density of the actuator forms another imperative element. It is determined by the work generated by the actuator and the volume of the actuator as shown in equation (4). Since work is a function of the force supplied (F) and the resulting displacement (d) as defined by equation (5), the energy density can be improved when the actuator delivers a large force over a small displacement or vice versa.

$$\text{Energy density} = \text{Total work generated} / \text{Volume of the actuator} \quad (4)$$

$$W = F * d \quad (5)$$

As seen in Figure 11(c), piezoelectric and shape memory alloy actuators provide a high energy density. This implies that they can store a large amount of energy within a small volume. Though the energy density does not scale with miniaturization, a small actuator size will be able to contribute only a limited amount of energy. [48] Apart from

these characteristics, parameters such as size, lifetime, power consumption and manufacturing requirements ought to be considered. Hence, the pros and cons of each actuation mechanism must be weighed before selecting one for the preferred application.

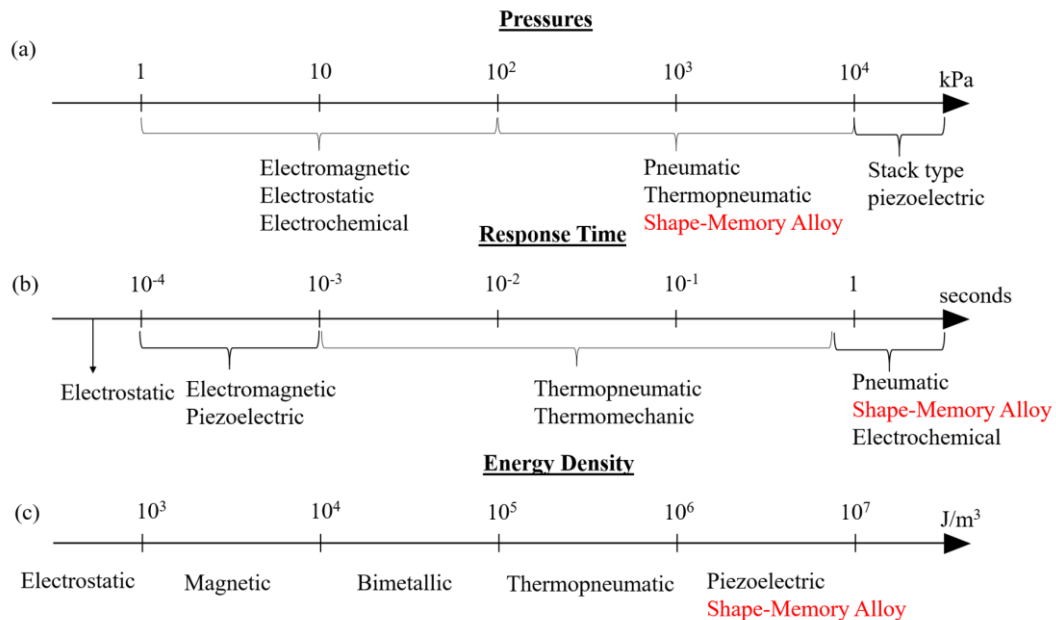


Figure 11. Characterizing the Actuation Mechanisms: The operational ranges for different parameters involved in the selection of the actuation mechanisms used in microfluidic valves. **(a)** Actuator generated pressures **(b)** Response times for actuators to allow switching between open-close or close-open states **(c)** Energy density range. The shape-memory alloy method is highlighted as it will be used for actuating the miniature valves. Adapted from [48]

(a) Active Non-Mechanical Microvalves

These miniature valves are established on the principle of phase change effect. Various phase transformation materials, such as hydrogel, sol-gel, paraffin and ice have been suggested for actuating membrane valves, making them suitable for portability. These materials exhibit volumetric changes which in turn is used to control membrane deflections.[10] The popular phase change microvalves include the use of wax [54], thermoresponsive polymers (pNIPAAm), hydrogels (PEG-diacrylate),[55] alginate, or temperature-sensitive liquid(FC-40).[56] While the fabrication process for these valves is challenging due to the need to integrate these materials inside microchannels, the

valves are indeed compact, leak-proof and self-actuated.[57] These valves are characterized by small volume change upon phase transformation and slower response times of tens of seconds to several minutes. Because of these limitations these valves are typically designed to operate for microchannels on the order of tens of microns.[10]

(b) *Active Mechanical Microvalves*

Alternative on-board approaches that overcome these challenges consist of the following actuation mechanisms for use with active mechanical microvalves.

(i) *Electromagnetic Actuation*

This form of actuation relies on the magnetic force generated by an electromagnet, permanent magnet or a hybrid attached to the membrane.[51] By using an external electromagnet for actuation, large magnetic fields can be generated that can actuate multiple valves simultaneously. However, several external components such as electromagnet solenoid coils and cores are desired, which snowball the overall size of the valve, resulting in an increased power consumption and complex microfabrication process. [42] The hybrid-integrated valve uses a relatively lower power to increase the magnetic forces. The mobile element can be integrated with coils or mounted with permanent magnets that is propelled by actuating external coils as seen in Figure 12(a).[48] Aside from membranes, ball-type valves exist. They consist of a spherical metal ball that is placed on the outlet orifice and prevents the fluid flow. When an external magnetic field is applied, the micro-ball moves upwards, hence opening the valve. [47] These types of microvalves face the three principal drawbacks: they are composed of rigid electromagnetic components, which prove to be ineffective for soft microfluidic valve applications, they are relatively expensive and scaling down of the

electromagnetic forces is disastrous. The induced force of a conductor in a magnetic field is governed by Faradays' law. It can be expressed as equation (6),

$$F = iLB \quad (6)$$

where i is the current passing through a conductor of length L in a magnetic field, B . As the conductor is scaled down by a factor of l , the current, magnetic field and length scales correspondingly as in equation 7.

$$i \propto l^2 ; B \propto l ; L \propto l \quad (7)$$

As the size decreases, it is more difficult to generate large magnetic fields with small cross-sectional area conductors. The proportional relationship between the force and the fourth power of the size of the valve makes the miniaturization of these valves arduous. [58]

(ii) *Electrostatic Actuators*

When a voltage is supplied to the actuator, an attractive force develops between the oppositely charged electrodes, which in turn causes the valve to shut. These electrodes are placed on the membrane and the valve seat as observed in Figure 12(b). [42] Some of the advantages surrounding this actuator includes the very fast response time for switching between states and low power consumption. The electrostatic force is expressed by equation (8), where A is the area of the plates, d is the spacing between the two plates, ϵ_r is the relative dielectric coefficient of the plates and ϵ_0 is the permittivity of vacuum. [42], [47], [48]

$$F = \frac{1}{2} \epsilon_r \epsilon_0 A \left(\frac{v}{d} \right)^2 \quad (8)$$

One significant disadvantage is that electrostatic actuation is suitable only for obtaining small displacements. As per this equation, the force is inversely proportional to the square of the distance between the two electrodes. For a smaller displacement, a larger force can be produced. As this actuation requires a high voltage to be supplied, the electrodes should be insulated, since direct contact with the fluid would result in electrolysis. Thus, this method is limited to gas applications.[51]

(iii) Piezoelectric Actuators

Piezoelectricity refers to the concept of applying an electric field to certain crystalline materials, such as zinc oxide and lead zirconate titanate (PZT) for producing a mechanical strain of less than 0.1%.[42] Figure 12(c) shows that an applied voltage can cause the membrane to expand or contract, mirroring the process on the valve diaphragm. As these materials have a high Young's modulus, the induced stress is in the order of several megapascals. Hence, piezoelectric actuation is widely used in applications that require a large force and small displacements, such as micropumps. Furthermore, deposition of these materials as a thin film on the membrane is tricky. Also, as thin-film actuators lack the ability to deliver enough force necessary for microvalves, external actuators are required, leading to bulky sizes.[48]

(iv) Bimetallic Actuators

Bimetallic strips are two bonded solids with a mismatch in the thermal coefficients of expansion. When the actuator is heated, they bend or morph the membrane to which it is attached to and this is observed in Figure 12(d). This is often known as thermal bimorph actuation. The heat required for actuation is provided by integrated heaters. However, they consume a lot of power and have a slow response time.

(v) *Pneumatic/ Thermo-pneumatic*

Pneumatic actuations are highly favorable in microfluidic applications. In this process, the flexible membrane is displaced within several hundred milliseconds by the application of pressure from an external pressure source. [42] A positive suction is used to deflect the thin elastic membrane to open the valve, whereas pressurized air is used to seal the valve.[10] Regardless of the reliability of this method, it necessitates off-chip apparatus such as compressed air supply, gas regulators and a vacuum pump. Thus, these valves are useful in applications where off-chip actuation is available. It proves to be insufficient for some point-of-care technologies where on-chip actuation is preferred.

Thermo-pneumatic microvalves involves a volumetric thermal expansion of gas, liquid or solid to apply pressure on the valve membrane. This temperature-controlled, phase change process allows high actuation pressures to be applied against the membrane, ensuring the closing, or opening of the valve. However, as seen in Figure 12(e), it requires a heat source in the actuation chamber and a slow phase change mechanism, it consumes a lot of power.

(vi) *Shape-Memory Alloy Actuators*

As the name suggests, shape-memory alloy (SMA) actuators undergo a phase transformation under the influence of temperature (Figure 12(f)). It transforms from a mechanically deformed state called martensite ('soft' state) at low temperatures to its original undeformed shape, austenite ('hard' state) at temperatures higher than its critical temperature. Some popular alloy systems include titanium/nickel (Nitinol), nickel/titanium/copper and nickel/titanium/palladium. For microvalves, the heat required to bring about this change is generated by passing electric current directly

through the alloy wire. With a response time of tens of milliseconds and a power consumption of a few hundreds of milliwatts, these actuators prove to be superior to the above mentioned processes for successful implementation in microvalves.[48] Moreover, they have the highest energy density among all the other methods.

The shape-memory alloy-based actuation offers a potential solution in this context owing to its fast response times. *Vyawahare et al* were the first to use a Nitinol ‘muscle’ wire for operating a PDMS based microvalve.[59] The Nitinol actuator exhibited a phase transition upon passing electrical current through it and generated a pull force to open/close the valve. Their device could open and close a 10 μ m channel

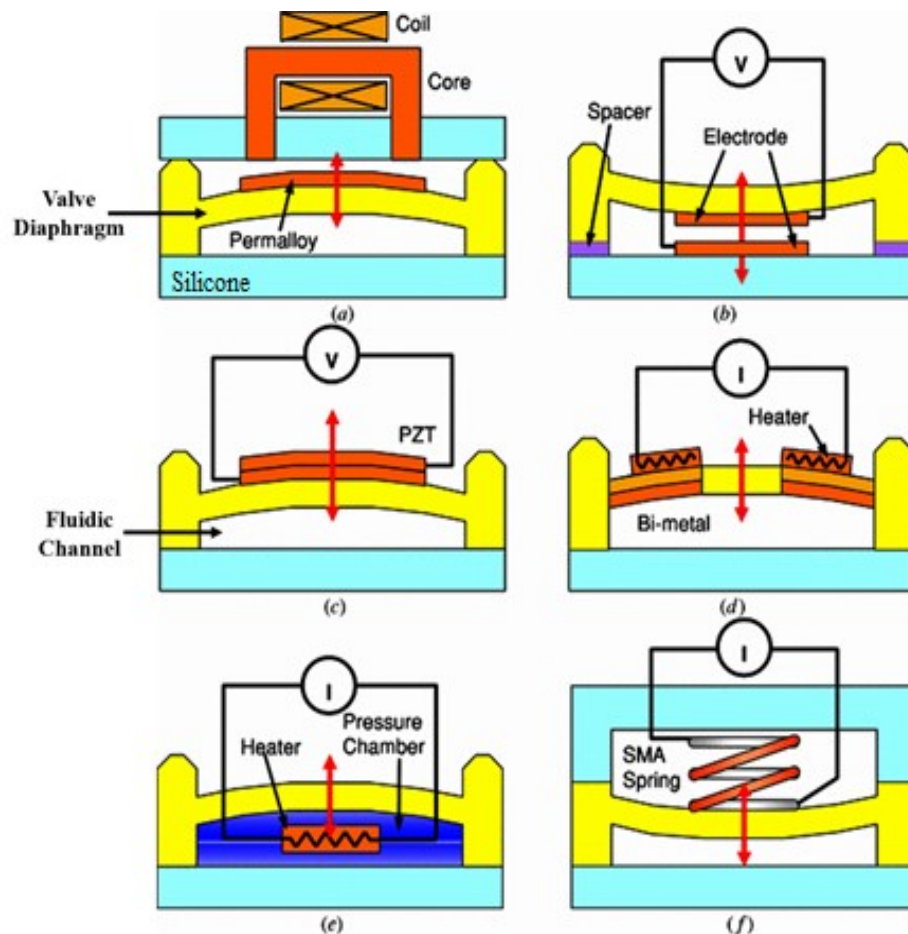


Figure 12. Actuation Principles of Microvalves: Diagrams illustrating some of the widely used actuation principles for active microvalves. (a) Electromagnetic (b) Electrostatic (c) Piezoelectric (d) Bimetallic (e) Thermo-pneumatic (f) Shape-memory alloy actuation. Adapted from [47]

by passing 230 mA currents through the wire. Similarly, *Gui and Ren* used a coiled Nitinol wire to build normally open and normally closed microvalves in PDMS. [10]

3.3 SDCS Valve Requirements

While these reports mentioned above show preliminary promise of electromechanical actuation for making autonomous microvalves, a microvalve design with lower power consumption would make it suitable for portable and field-deployable applications. [59] The valve needs to be operated entirely in an autonomous way with the power consumption consistent with the use of a small battery, without the use of any external apparatus. The geometry of the valve should minimize the overall force requirements for the flexible membrane. The actuation mechanism for SDCS must be on-chip, energy efficient and should easily interface with the valve material. The entire assembly should be capable of being packaged in a relatively compact manner while maintaining a robust operation. [10] Thus, this thesis focuses on a popular valve architecture, the plunger-membrane microvalve.

Actuation Mechanism

The mechanism of actuation for the valves is vital for the viability of the device. Out of several possibilities of valve actuation mechanisms, the shape memory alloy actuators are ideal candidates considering their current based reversible actuations. Specifically, the Nitinol muscle wire exhibits a remarkable shape memory property by contracting its length by approximately 4% under the application of electrical current and returning to its original shape after the withdrawal of the driving current. If the current passed through the wire is under a threshold value provided by the manufacturer, the wire can withstand millions of repeated stress cycles. At optimal actuation conditions of driving current, a 50 μ m diameter Nitinol wire can generate a

maximum pull force of 36 grams. Although the pull forces can be increased by passing more current, the wire suffers from irreversible shape changes due to excessive thermally induced stresses, limiting its long-term use. A miniature valve constructed with an actuation trigger force of 36 grams or less can potentially lead to the development of a miniaturized SDCS implant.

Impedance Requirements

Moreover, the impedance requirements for the microfluidic valve imposed by the SDCS system design stem from the necessity to maintain a maximum safe 30V compliance voltage within the device but still deliver up to 200 μ A of output current. Due to this constraint, a maximum limit of 35k Ω was imposed for the open valve state and a minimum of 10x increase in impedance from the open to closed state is required to ensure efficient device operation.

These requirements form the basis on which the miniature valve is designed. The following sections mention the different experiments carried out for optimization and testing of these plunger-membrane structures for validating their use in the SDCS technology.

3.4 Experiment 1: Characterization of Normally-Open Valve Geometry

To satisfy the pull force criterion, the geometry and material of the valve plays a significant role in determining the force needed for a complete and effective valve closure. Based on the microfluidic valve design from *Vyawahare et al.*, [59] abbreviated as squeeze valve (SV), a comparison was carried out between four distinct miniature fluidic valves made from PDMS and capable of being actuated with a Nitinol muscle wire. Two implementations of this squeeze valve are examined; one with a 0.5mm diameter (SV_{0.5}) and the other with a 1.5mm diameter (SV_{1.5}) lumen. The designs are

further modified into a multilayer plunger valve (PV_{0.75} and PV_{0.85}). These two valve designs, named squeeze valve (SV) and plunger valve (PV) are initially pictured to be in normally open states. Each valve has a thin layer of flexible membrane that is deformed under the action of the pull force generated by the Nitinol muscle wire. When the membrane is sufficiently deflected, it physically blocks the adjacent fluidic channel, thereby increasing the overall ionic impedance. The feasibility of using these four valve types for SDCS technology is tested.

3.4.1 Fabrication Methods

Valve Construction

There are key structural differences between SV and PV valves. Firstly, the SV valve has a single layer of fluidic channel underneath its thin elastic membrane, whereas, the PV valve has two fluidic channels stacked on top of each other, connected via a vertical through hole. Secondly, the plunger valve is designed to include an additional structural element, called plunger, which is a small block of PDMS attached to the thin elastic membrane. The mechanism by which that pull force is translated in the valve closure is slightly different for both designs. In case of a closed SV valve, the entire fluidic channel is squeezed by the deformed membrane thereby blocking the ionic flow. On the other hand, the vertical through hole is blocked by the downward motion of the plunger in closed PV valve. Figure 13 shows schematic representations of cross-section of each type of valve. Other critical structural details such as fluidic channels, the plunger, the placement of nitinol wire etc. are also highlighted and labelled in the same figure. The right column in Figure 13 shows the conformational changes in the cross-sections when these valves are switched to a closed state. For effective operation

of the PV valves, the nitinol wire is looped over a resin button bonded to the thin membrane.

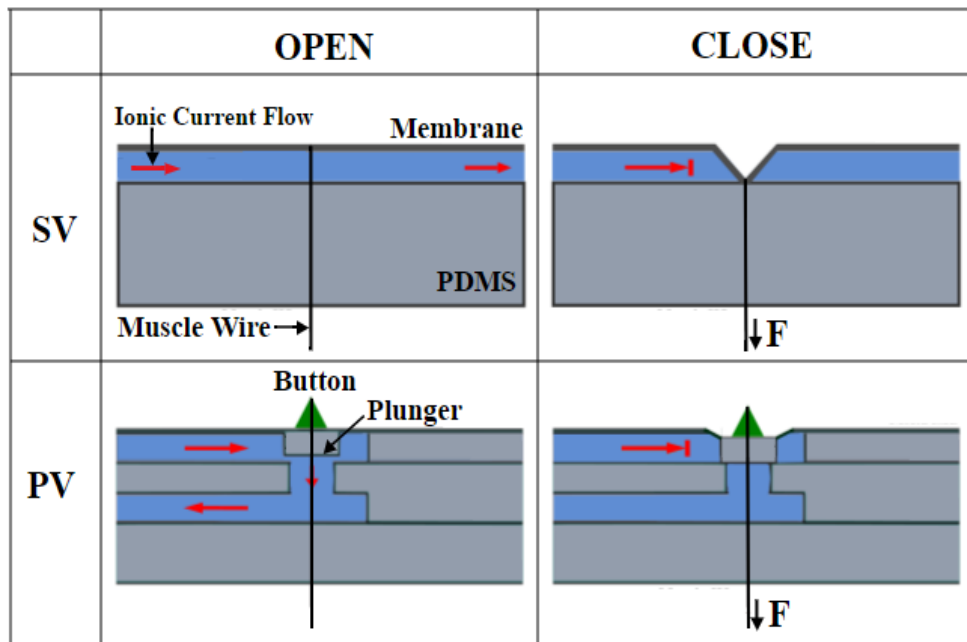


Figure 13. Depiction of Valve States: The top row shows the schematic of the open and closed states of a squeeze valve. The bottom row shows the schematic of the open and closed states of a plunger valve.

For an SV valve, the change of the cross-sectional area is governed by the overall bending characteristics of the thin membrane and in turn is a strong function of the channel depth. Hence, a valve with shallower channel will need a small trigger force for its complete closure than a valve constructed with a deeper channel. To test this hypothesis, two squeeze valves were designed and tested, each with a different channel depth, while keeping the membrane layer thickness constant at 0.1 mm. The valves are denoted as $SV_{0.5}$ and $SV_{1.5}$, where subscript denotes channel depth of 0.5 mm and 1.5 mm respectively. The fluidic channels were half rounded for effective valve closure compared to a rectangular cross-section.

Unlike the SV valve, the bending of the membrane is translated to the downward motion of the attached plunger in case of PV valves. Even if the membrane does not

block the entire fluidic channel, the plunger effectively blocks the vertical through hole, thereby making this design very sensitive to the applied external force. This became the foundation for the hypothesis that stated that this modified valve structure will require lesser closure force than the SV valves and is strongly dependent on the height of the plunger. Two PV valves, PV_{0.75} and PV_{0.85}, where the subscript denotes plunger height of 0.75 mm and 0.85 mm respectively were constructed and tested. The membrane layer thickness and fluidic channel layer depth were held constant at 0.1 mm and 1 mm respectively. The connecting vertical cylindrical through hole was 1.6 mm in diameter and 0.75 mm in height. For a perfectly closed valve, the impedance measured across the valve should be infinite in theory. For this study, an increase of 10-fold from the open valve impedance value was selected as the criterion for representing a closed valve state. The feasibility test for SDCS was conducted by measuring the closure force required to close the valve and valve impedances for all four valve designs as the valve is being closed.

Valve Fabrication

The valves were fabricated by replica molding of poly-dimethyl siloxane (PDMS). The squeeze valve was constructed by bonding two separately molded layers of PDMS, namely fluidic channel layer and the thin membrane. On the other hand, the plunger valve consisted of a total of four layers: 2 fluidic channel layers, an intermediate layer for the vertical through hole connecting the two channels and a membrane layer with a plunger. The molds for each layer were created using a 3D printer (B9Creations, South Dakota), which used a photo curable polymer resin (B9R-2 Black Resin, B9Creations, South Dakota). The printed molds were rinsed with distilled water to removed uncured polymer traces. The masters then were post cured using a UV lamp for 12 hours. For an easy peeling-off of cured PDMS blocks, the molds were first treated

with a corona treater (BD-20AC, Electro-Technic Products) followed by silanization using vapors of trimethylchlorosilane (Sigma-Aldrich). A 10:1 wt./wt. mixture of pre-polymer mix of PDMS and curing agent (Sylgard 184 Elastomer Kit, Dow Corning) was poured over these molds and cured on a hot plate at 80°C for 12 hours. For the membrane layer, PDMS mixture was spin coated at 1000 rpm for 10s using a spin coater. The cured PDMS layers were then plasma treated again and carefully stacked on top of each other, maintaining the alignment. As the final step, a button was mounted on the uppermost membrane layer and a nitinol wire was looped around this button. This fabrication procedure is depicted in Figure 14.

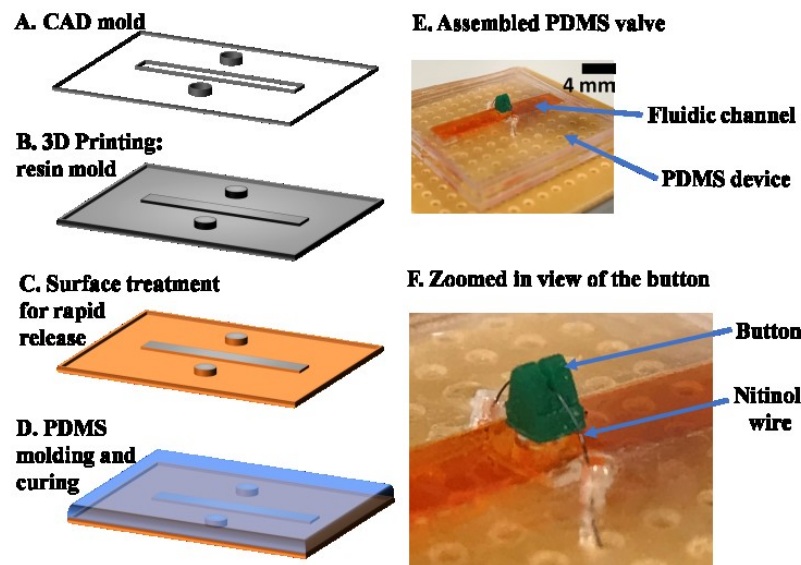


Figure 14. Normally-Open Valve Fabrication Process: (A)-(D) General steps involved in the fabrication process of the chip. (E) Photograph of an assembled PDMS valve. The fluidic channel was visualized using an orange colour food dye. (F) Zoomed-in view showing the resin button around which the nitinol wire is looped.

3.4.2 Test and Measurement

A schematic of the experimental setup along with the test circuit to measure valve impedances is shown in Figure 15. Before each test, the fluidic channel was filled with a 0.9 M NaCl saline solution that served as a medium for ion conduction. The nitinol muscle wire was looped around the button and both the ends were securely

attached to a micromanipulator. A 5V, 1kHz waveform was applied across the channel and a digital force gauge was used to displace the wire tip in a controlled manner. The resulting pull force on the button was recorded at every step along with the voltage measured across the sense resistor. Testing experiments were repeated three times with a newly fabricated valve for each test to encompass the experimental uncertainty in valve manufacturing.

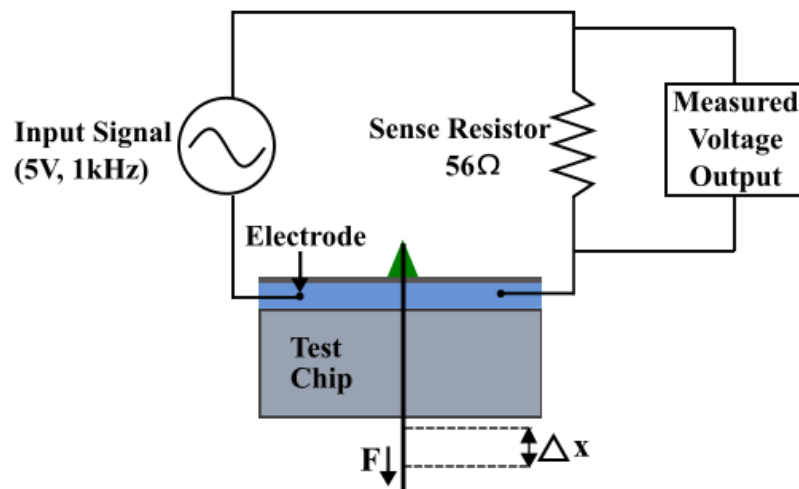


Figure 15. Testing Setup of Normally-Open Valves: Experimental setup where a sinusoidal input signal is applied to the test chip. The displacement of the muscle wire is varied, and the corresponding force is obtained from the force gauge. The change in amplitude of the output voltage signal is used to calculate the magnitude of the impedance.

3.4.3 Results

Through the above impedance measurements test set-up, the pull force required for a complete valve closure was determined for all the four valve designs, i.e. squeeze valves, $SV_{0.5}$, $SV_{1.5}$ and plunger valves $PV_{0.75}$ and $PV_{0.85}$. Figure 16 (top) shows the impedance vs force characteristics of squeeze valves. The general upwards trend of the force-impedance curves can be explained simply by replacing the impedances by ionic resistances.

The $SV_{1.5}$ valve impedance was measured to be $9.5k\Omega$, satisfying our set design criterion for maximum open valve impedance for SDCS. However, even with a force

as large as 120 grams, the valve could not be closed completely, as indicated by a 3-fold increase in final valve impedance. In contrast, closure force for $SV_{0.5}$ was found to be 52 grams, which is close to the 36 grams design valve criterion. However, its open valve impedance was measured to be around 95 k Ω , substantially higher than the allowed maximum open valve impedance. These results conclude that both squeeze valve designs fail the feasibility test for SDCS and considerable design improvements are needed.

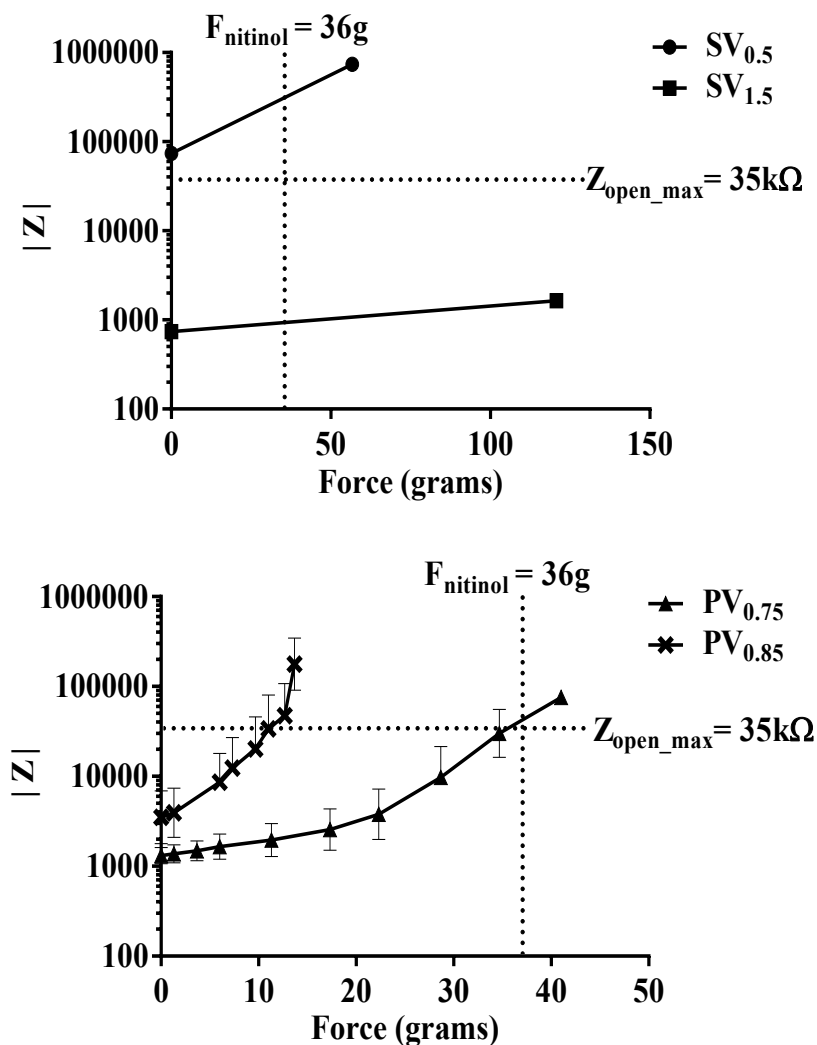


Figure 16. Impedance Characterization of Squeeze Valves: (top) Impedance vs applied force characteristics with for the two squeeze valves, $SV_{0.5}$ and $SV_{1.5}$. $Z_{\text{open_max}}$ refers to the maximum impedance for an ideal SDCS open valve. (bottom) Impedance vs applied force characteristics for the two plunger valves, $PV_{0.75}$ and $PV_{0.85}$ with a plunger height of 0.75mm and 0.85 mm respectively.

The force-impedance analysis of PV valves with the plunger height of 0.75 mm and 0.85 mm can be seen in Figure 16 (bottom). For the PV_{0.75} valve, the initial open valve impedance was measured to be 1 k Ω , while for the PV_{0.85} valve it was 5 k Ω , both passing the initial test for the low open channel impedance.

Figure 17 (top) shows the plot of applied force vs normalized impedance for both PV valves. In the same plot, the 10-fold valve increase is highlighted to visually

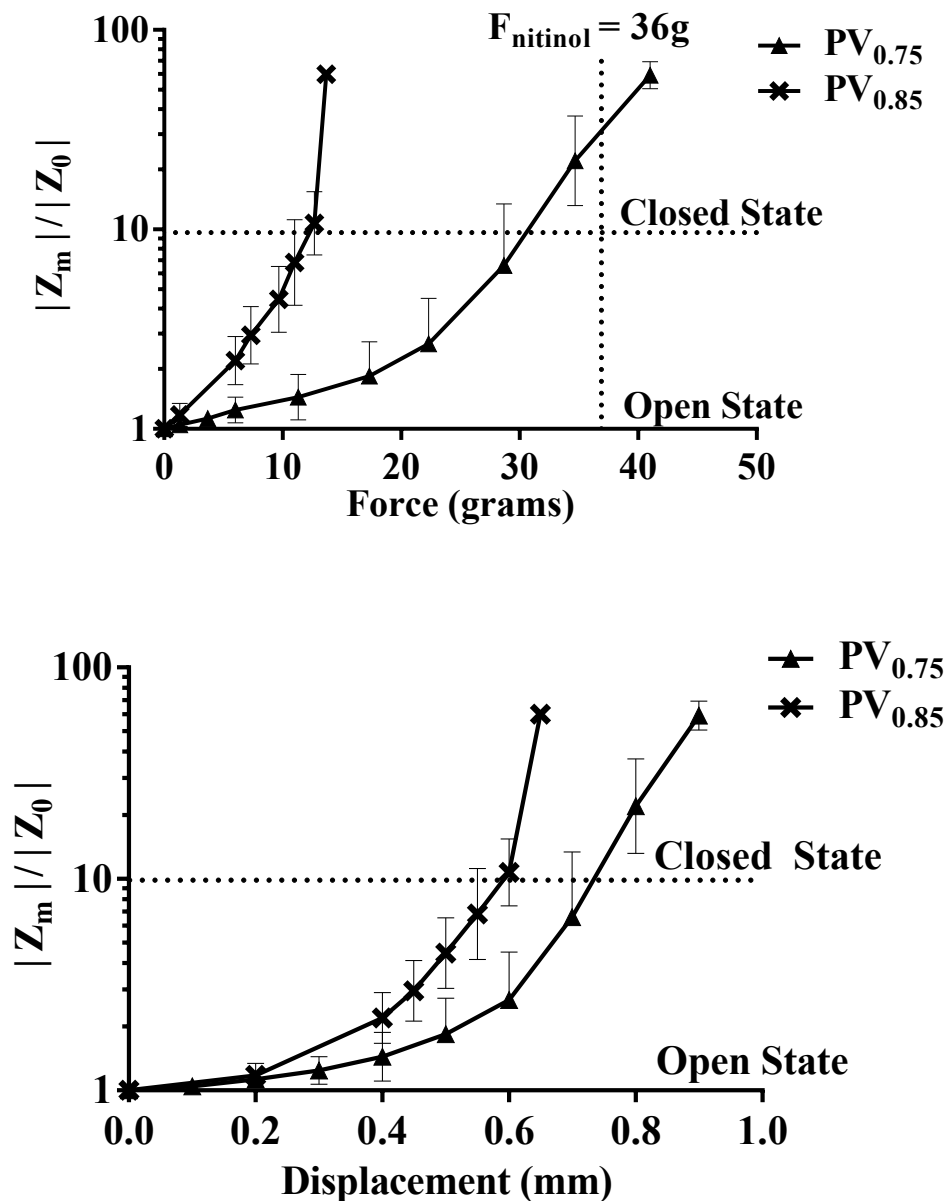


Figure 17. Impedance Characterization of Plunger Valves: (top) Normalized impedance characteristics for the plunger valves PV_{0.75} and PV_{0.85} with varying actuation force. (bottom) Normalized impedance characteristics for the plunger valves with respect to wire displacement.

depict the closure criterion. Both PV valve designs were found to be much more sensitive than the SV valves, with PV_{0.85} requiring lower force and a smaller displacement to close as compared to PV_{0.75}. The PV_{0.75} valve with a plunger height of 0.75 mm required a force of 32 grams for 10-fold impedance increase. The PV_{0.85} valve with a longer plunger height of 0.85 mm, required only a force of 14 grams for its closure. This drastic change in the valve sensitivity can be attributed to the structural design and improved bending characteristics by incorporation of the plunger on the membrane.

For understanding the membrane deformation of the SV and PV valves, we plotted the normalized channel impedance values as a function of the nitinol muscle wire displacement in Figure 17 (bottom). While it is difficult to measure the displacement of the plunger, the plot gives an insight to the amount of displacement needed for the required closure. The PV_{0.75} and PV_{0.85} valve required a displacement of 0.6 mm and 0.75 mm respectively to achieve valve closure. These results confirm the hypothesis that by increasing the height of the plunger, the valve sensitivity is enhanced. However, there is an optimal plunger height beyond which further increase will violate the initial open valve impedance criterion for SDCS.

3.4.4 Discussions

This experiment examined two valve designs for their practicability in SDCS technology. Two feasibility criteria were used other than the valve footprint: 1) maximum allowed initial open valve impedance of 35 k Ω as dictated by safety and power requirements of the SDCS system design and 2) maximum complete valve closure force of 36 grams as set by the nitinol wire manufacturers for reversible long-

term actuation. It was ascertained that both the squeeze valve designs could not satisfy the feasibility test, whereas the PV valves designs passed the feasibility criterions.

3.5 Experiment 2: Characterization of Normally-Closed Valves

From the results obtained in Experiment 1, it was safely concluded that the channel depth and plunger height are two of the most crucial parameters that dictate the PV valve performance. By increasing the height of the plunger, the required pull forces can be decreased but at the same time the initial open valve impedances increases. An optimization screen is thus needed as a next step to minimize the power requirement of operating PV valve. Power delivery for the SDCS device is contingent on the application. Since they devices are intended for in-vivo animal studies, it should be powered by 3.7V, which corresponds to the voltage supplied by rechargeable lithium-ion batteries. Aside from the power requirements of SDCS, various microvalve architectures designed for such in-vivo and point-of-care diagnostic application requires larger channels, autonomous actuation, and portability. This can be achieved by improvising the normally-open design into a normally-closed valve that is capable of a fully autonomous actuation for wide diameter microchannels (tens to hundreds of μm). It was further speculated that this type of valve design would require a smaller force to open the valve, in comparison to the normally-open valve layout. A 50 μm Nitinol shape memory alloy wire is incorporated into the device and can operate the valve when actuated with 100 mA current delivered from a 3 V supply. The valve is characterized for its actuation kinetics using an electrochemical assay and its reliability is tested at 1.5s cycle duration for 1 million cycles, during which no operational degradation was observed.

3.5.1 Fabrication Methods

Valve Construction

For this experiment, a normally-closed multilayer plunger-membrane valve is constructed and actuated with a shape-memory alloy. Figure 18(a),(b) shows a schematic representation of the cross-sectional view of the valve. The microvalve consists of three conceptual parts: (1) a thin elastic PDMS membrane with an attached cylindrical plunger, (2) an upper and a lower fluidic channel, and (3) a vertical through-hole connecting the two channels. A Nitinol shape-memory alloy wire was embedded in the membrane layer right above the plunger base. The SMA wire undergoes a phase transition when an electrical current is passed through it. This results in contraction of its length, thereby generating a pull force on the attached PDMS membrane and subsequently lifting the plunger, opening the valve. The wire relaxes back to its original

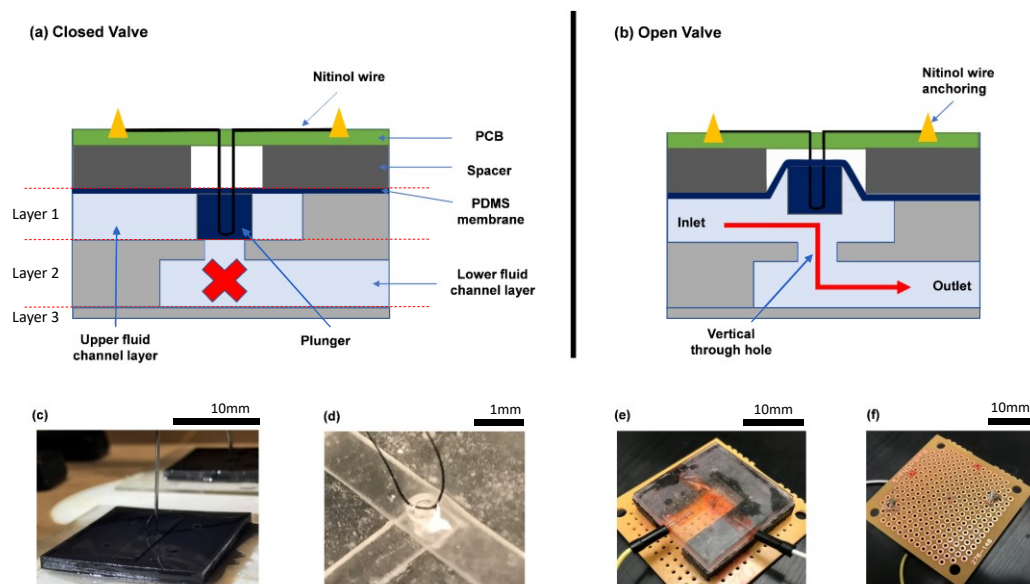


Figure 18. Normally-Closed Valve Design and Fabrication: (a) Schematic representation of the microvalve cross section. Under no electrical actuation, the valve is in closed state. The layers 1, 2, 3 delineate the parts of the valve that were manufactured from the same molds. (b) When the Nitinol wire is actuated electrically, pull force generated on the membrane lifts the plunger upward thereby opening the valve. (c) Image shows the process of embedding 50- μm surgical suture wire in the uncured polymer matrix. The Nitinol SMA wire was looped around this suture in the final assembly. (d) Image showing the embedded surgical suture wire in the PDMS membrane layer after the polymer has cured. (e) The assembled microvalve with bare metal electrodes embedded in the inlet and the outlet for electrochemical impedance testing. (f) Nitinol wire anchoring for electrical actuation using low temperature solder.

shape upon withdrawal of the electrical stimulus, allowing the miniature valve to close. The driving current and the geometry of the valve determine the amount of force generated and the resulting displacement of the plunger.

Valve Fabrication

Reagents and materials

Nitinol SMA “muscle” wires of 50 μm diameters, 3–130 MW Flexinol 050 HT, were purchased from Dynalloy, Inc. (Irvine, USA). A two part 184 Sylgard elastomer kit containing poly-dimethylsiloxane (PDMS) pre-polymer mix and a cross-linking agent was purchased from Ellsworth Adhesives (WI, USA). A photocurable polymer resin, B9R2, was purchased from B9 Creations (South Dakota, USA). Sodium chloride (NaCl) was purchased from Sigma-Aldrich. Chlorotrimethylsilane was purchased from Sigma-Aldrich and used for surface treatment.

Device Fabrication

The normally closed microvalves are made from PDMS using a soft lithography fabrication protocol. Each valve layer was manufactured separately and assembled. First, CAD designs were created using the SolidWorks software, and molds for each layer were 3D printed (B9Creations, South Dakota) using the photocurable resin. The manufactured valve layers corresponding to the specific three molds are delineated in Figure 18(a). Layer 1 contains the upper channel, the top membrane, and the plunger. Layer 2 contains the through hole and the lower channel. Layer 3 is a nonpatterned PDMS base layer. The printed molds were then rinsed thoroughly in an ultrasound bath with DI water containing a commercial surfactant (dish washing liquid) to remove uncured polymer traces. The molds were then post-cured under UV light for 12 h for further solidity. To peel off the casted PDMS layers easily, the mold surfaces were

treated with a corona discharge (BD-20AC, Electro-Technic products) followed by salinization with trimethylchlorosilane. A 10:1 wt.% mixture of PDMS pre-polymer and curing agent was degassed in a vacuum chamber to remove any air bubbles and poured over each mold. A 50- μm surgical suture wire loop (approximately 5 mm diameter) was carefully embedded in the uncured polymer in the membrane layer using micromanipulators to position the loop inside the plunger. The assembly was put on a hot plate to cure at a temperature of 90 °C. Initially, the nitinol SMA wire was intentionally embedded in the membrane layer to avoid the thermal damage to the actuator while the PDMS cures. Instead, the Nitinol actuator was looped through this suture wire before fixing its ends on a breadboard. All the other layers were then baked in an oven at 90 °C for curing. The PDMS layers were carefully peeled off, then aligned using the alignment marks, and sequentially bonded together using a corona discharge to form the microfluidic valve as shown in Figure 18(c), (d). The assembled PDMS chip was mounted on top of a single sided breadboard. The free ends of the embedded Nitinol SMA wire were then anchored to the breadboard nodes using a solder (Rosin Core, Alphasmetals Inc.). It was made sure visually that the wire did not have any sag before anchoring it to the breadboard.

3.5.2 Test and Measurement

Electrochemical assessment of valve opening and closure

An electrochemical assay was used to study the microvalve performance, tantamount to a previously described study [50]. This electrochemical assay compared to a flow-based assay that offers a higher-precision monitoring of valve leaks. To assess the valve performance during its operation, an AC signal was applied across the fluidic channel containing an electrolyte solution as shown in Figure 19(a). In the closed state (Figure 19(b)), the available cross-sectional area at the valve seat for ionic transport is

minimized, resulting in larger impedances when compared to an open valve (Figure 19(a)).

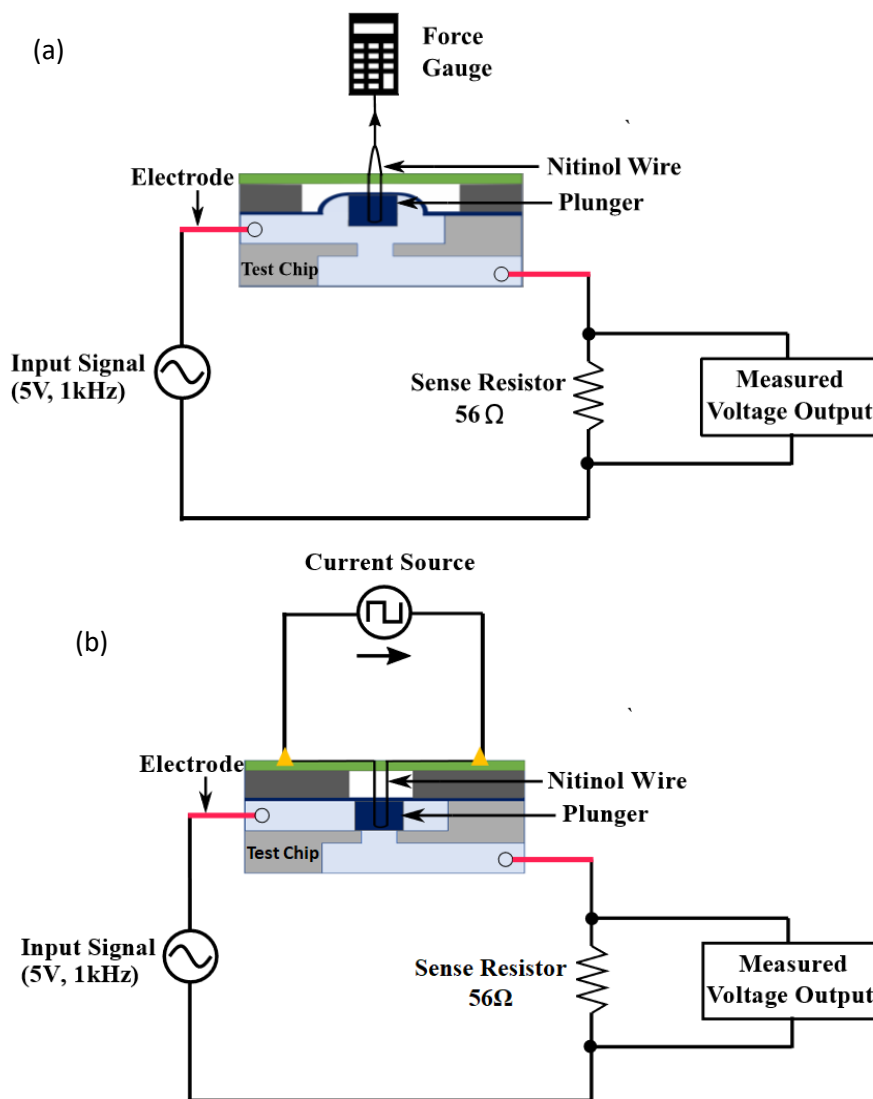


Figure 19. Testing Setup of Normally-Closed Valves: (a) Schematic for the characterization setup and electrical test circuit for optimizing pull force for the plunger-membrane microvalve. Inset image shows valve carrying a 1-M NaCl electrolyte solution in the channels along with two bare metal electrodes for electrochemical assay. **(b)** Test setup showing the electrical actuation of Nitinol SMA wire using a pulse generator.

The different valve states: open, closed, and partially open/closed can be differentiated by comparing the strength of ionic currents flowing through the channel. After the valve fabrication step, the channels were filled with an aqueous electrolyte, containing 1-M sodium chloride dissolved in deionized (DI) water. It was ensured that there were no air bubbles in this pre-filling step, as they significantly alter the electrical

resistances, thereby impacting the results. Two bare metal electrodes were inserted upstream and downstream of the valve in the upper and lower fluidic channels, respectively. The electrodes were connected to a function generator, which provides an input signal of 5 V at 1 kHz across the embedded electrodes. The current was measured from the voltage measured across a 56- Ω m sense resistor using an oscilloscope. The electrical test circuit used is shown in Figure 19(a). The input signal frequency of 1 kHz was chosen to minimize the damage to the electrodes during the measurements. Such electrode damage occurs at lower frequencies owing to the irreversible Faradaic reactions. The kinetics of valve operations including valve opening times, closing times, and percentage of valve opening were determined by observing the temporal changes to the output signal as a function of several actuation parameters. The open state of the valve was defined such that it was indicated by an impedance of under 2 K Ω and the closed state to be indicated by 20 K Ω or above (10 \times the open state impedance). Based on the calculation of charge per unit time at 5 V, the number of sodium ions that flow through the valve is 2.7 nmol/s in closed state.

Effect of plunger radius and height

The required pull force necessary to open the valve must be minimized to lower the power consumption. Even though there are several parameters in the valve design that affect the pull force, the plunger diameter and height as the key parameters that dictate the bending characteristics of the flexible membrane. A thinner membrane requires less pull force to open the valve fully, but owing to our large channel width, the thin membrane can potentially sag into the channels. Membrane sagging can lead to a pre-stressed membrane valve, heavily influencing the valve performance. Thus, the membrane thickness was kept constant at 100 μ m for this study. No visual sagging was observed in the membrane at this thickness. Three valves with different plunger heights

were fabricated to study their effect on the required pull force. These valves were designed with plunger heights of 0.9, 0.95, 1, and 1.05 mm, while keeping the plunger radius constant at 1.2 mm (12 valves total). Similarly, to test the effect of plunger radius, three valves were fabricated each with radii 1.2, 1.4, 1.6, and 1.8 mm, while keeping the plunger height constant at 0.95 mm (12 valves total). The valve opening, and closing were assessed using the electrochemical circuit. The two free ends of the SMA wire were attached to a micromanipulator and displaced to mimic the shape memory alloy actuation. The resulting pull force on the wire was recorded using a force gauge, while observing the valve states electrochemically.

Effect of driving current amplitude and its frequency

The effect of the driving current signal on the valve performance was studied. In this case, a function generator was attached to the soldered ends of the Nitinol SMA wire to vary the driving current signal's amplitude and frequency. The resulting effect on the valve performance was reflected in the measured electrochemical current. The amplitude of the driving current determines the contraction length of the Nitinol wire and significantly affects the generated pull force. Then, the current amplitudes were varied from 0 to 150 mA keeping the frequency fixed at 0.67 Hz (1.5 s period). The voltage across the SMA wire ranged between 0 and 3 V for this experiment. For evaluating the response time of the valve, the frequency of the actuation pulse was changed, while keeping its amplitude fixed at 95 mA.

Valve leakage test

A leakage test of the microvalve was performed to determine the threshold pressure beyond which the valve leaks substantially. Owing to its geometrical asymmetry, the valves were tested in both directions to determine the forward and the

backward leakage pressure. In the “forward” direction, the inlet (layer 1) was pressurized using fluid pressure upstream of the valve, while maintaining the atmospheric pressure downstream at the outlet (layer 2). Analogously, in the “backward” direction, the outlet was pressurized relative to the valve inlet, which was kept at atmospheric pressure. The leakage was determined by measuring the change in the electrical impedance across the microvalve, and corresponding pressure was monitored by a pressure gauge.

Long-term reliability test

The microvalve design was subjected to long-term reliability test to identify failure mechanisms. Two possible scenarios of valve failure were recognized. One is the fatigue failure of the actuator SMA wire itself owing to irreversible changes upon long-term electrical actuation. In this case, the wire can become permanently elongated or break. The second possible failure point is the joint between the SMA wire and the PDMS membrane at the embedding junction. To verify this, two tests were carried out where the Nitinol wire was actuated with a driving current of 105 mA ($N = 2$) and 160 mA ($N = 1$), respectively, while keeping the cycle duration at 1.5 s. Its performance was recorded at intermediate time points using the electrochemical impedance assay as described earlier. It is known that higher current can accelerate the fatigue failure process, owing to an increased heating of the shape memory alloy. Thus, the valve test with 160-mA actuation current also served as the negative control to validate the assay. Electrode degradation and electrolyte evaporation posed a challenge in this experiment. To overcome this issue, new electrodes and a freshly made electrolyte had to be inserted at each time point during the measurements.

3.5.2 Results

Effect of plunger radius and height

The effect of plunger size on the required pull force is summarized in Figure 20 (a),(b). The electrochemical impedance assay was used to assess the valve opening and closure. The measured open valve impedance of each variant was found to decrease by two orders of magnitude as the valve changed its state from closed to open upon the application of force. Figure 20(a) indicates that the pull force needed to open the valve declines with the decreased plunger height.

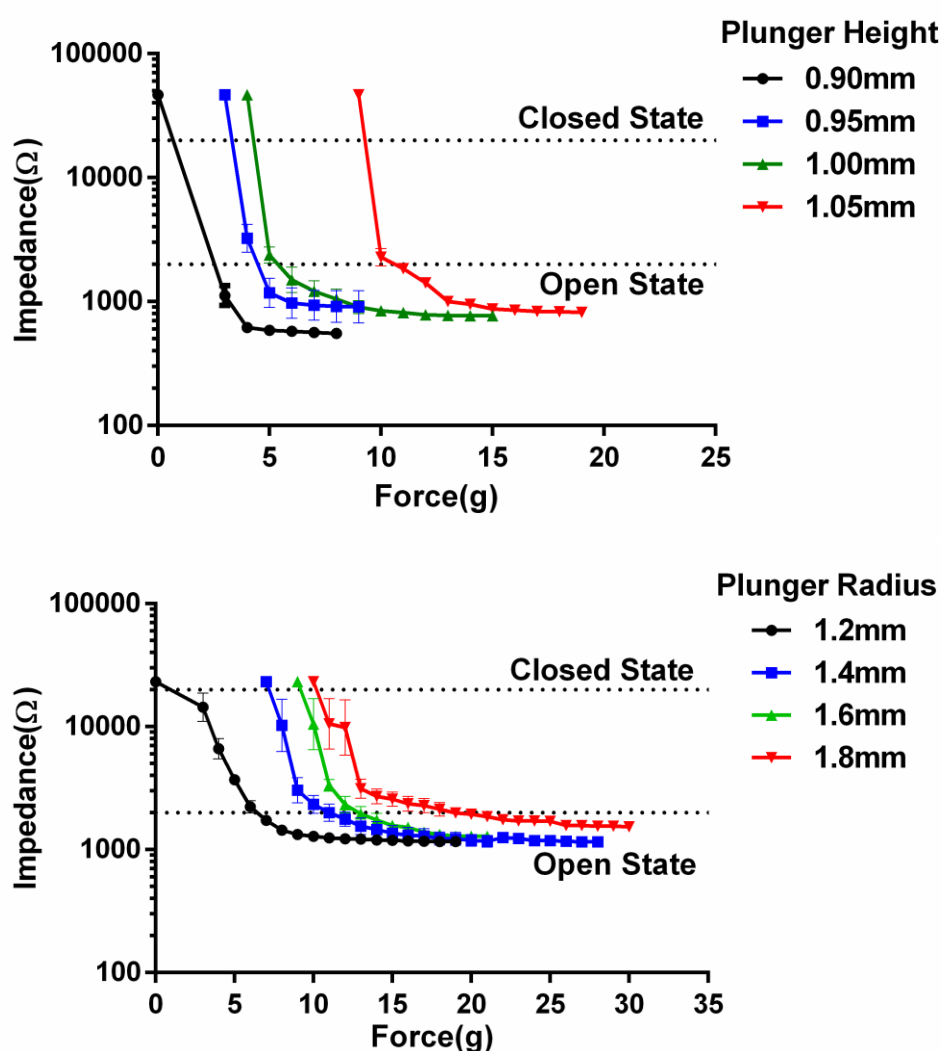


Figure 20. Impedance Characterization of Normally-Closed Valve Geometry: (a) Force–impedance characteristic plot for plungers of different heights. (b) Force–impedance characteristics plot for plungers of different radii. N = 3 chips tested for each plunger height in a and each plunger radius in b. Error bars represent standard deviation of the measurements

For a plunger with a height of 1.05 mm, the required pull force for a complete valve opening was found to be around 20 g, whereas for the plunger height of 0.9 mm, the force was around 7.5 g. This trend can be explained by considering that the opening covered by the plunger was slightly elevated during the manufacturing process due to surface tension. During curing, this surface tension created a meniscus at the part of the mold filling the opening. The result was that the higher height plungers created a stress on the top membrane that was greater than that due to the smaller height plungers in their resting state. This tension, therefore, required a larger force to lift the higher height plungers. At 0.9 mm plunger height, the impedance when no pull force was applied was very near the limit for closed state impedance (20 K Ω), whereas for the higher height plungers, this closed state impedance was reached at higher forces. This plunger height was selected as the lower limit for this parameter because reducing the plunger height beyond this point may not be desired owing to the increase in the closed state leakage currents, thereby violating one of the feasibility criteria.

The effect of the plunger radius on the valve performance is plotted in Figure 20(b). The required pull force increased with the radius of the plunger. At 1.2 mm, the force required to fully open the valve was found to be around 10 g, whereas for the radius of 1.8 mm, it was around 20 g. This direct relationship between the plunger radius and the force necessary to open the valve could be due to the added contact area around the valve opening, resulting in surface area tension due to stiction. Based on these characterizations, the height of 0.95 mm and radius of 1.2 mm were selected as optimum parameters (i.e., requiring minimum force, while being able to fully open and close) for the subsequent electrical tests.

Measurement of valve opening and closing times

The opening and closing kinetics of the optimized microvalve design are shown in Figure 21. The plot shows the time course of measured electrochemical current flowing through the valve as a function of the applied electrical stimulus in the Nitinol actuator. A time delay of $\tau_{\text{onset}} = 0.265$ s was observed from the point of the application of the trigger to the point where the valve starts to respond. This observed time lag is composed of two components. When an electrical current is passed through the actuator, there is an intrinsic time delay associated with the phase transition within the shape memory alloy. Secondly, there is a bonding force (stiction) initially present between the plunger base and the channel. If the applied force on the membrane is not greater than this bonding force, the valve remains in a closed state. However, as soon as the pull force is greater than this threshold value, the membrane is lifted from the surface and the reactionary force component disappears leading to a rapid membrane motion in response to the electrical trigger. This membrane motion is reflected in the rise of the electrochemical current as seen in the plot. For the valve undergoing testing,

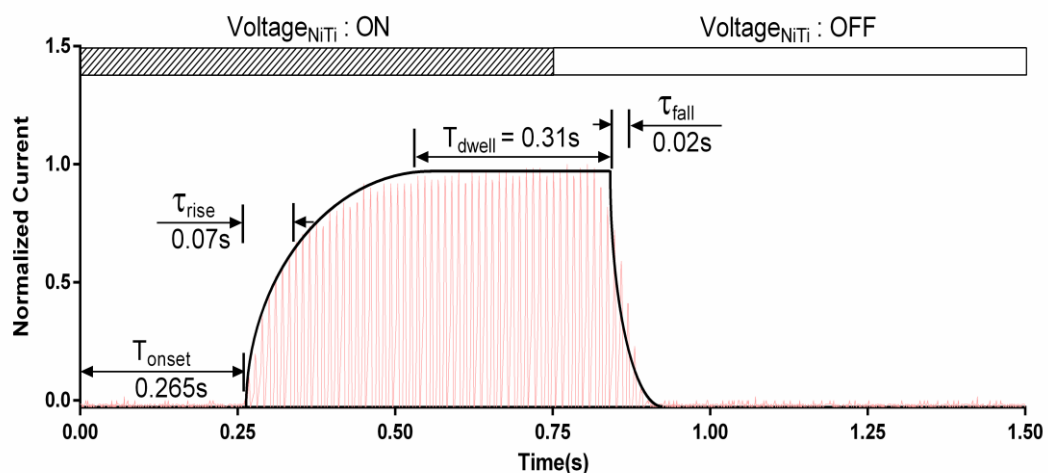


Figure 21. Electrical Actuation of the Plunger-Membrane Valve. A current response of the microvalve for Nitinol actuation current of 100 mA for a driving current pulse width of 0.75 s at 95 mA followed by a relaxation time of 0.75 s at zero current.

the time constant for this process was found to be $\tau_{\text{rise}} = 0.07$ s. For the applied pulse width of 0.75 s, the valve remained in the fully open state for $\tau_{\text{dwell}} = 0.265$ s.

As the electrical pulse was withdrawn after 0.75 s, the measured electrochemical current diminished to its baseline value reflecting the closed valve state. The relaxation time of $\tau_{\text{offset}} = 0.09$ s was observed from the withdrawal of the current from the wire to when the valve responded to this change. This time lag represents the time associated with the cooling of Nitinol muscle wire to the temperature below its phase transition of ~ 78 °C. Once the muscle wire is sufficiently relaxed the time constant for closing the valve due to its elasticity was found to be $\tau_{\text{fall}} = 0.02$ s.

Effect of driving current amplitude and its frequency

Figure 22(a) shows the effect of driving current amplitude on the valve performance. The plot indicates that the current driving the SMA wire needs to be greater than 95 mA to open the valve. The transition between open and closed states is rather sudden, occurring within only 10 mA, between 90 and 100 mA. This sudden transition is attributed to the bonding force between the plunger base and channel surface as explained in the earlier section. Figure 22(b) shows the variation of open valve impedances as a function of frequency, while maintaining the optimized current amplitude of 95 mA flowing through the SMA actuator. The valve remained in the closed state for frequencies higher than 4 Hz. For the driving frequencies in the range of 2–4 Hz, the valve opened partially. And for frequencies lower than 2 Hz, the valve could fully open. This observed frequency behavior can be explained by considering onset time lags as discussed in the previous section. The amount of contraction and the resulting force in Nitinol actuator strongly depends on the pulse duration. At higher

frequencies, there is not enough time for the shape memory alloy to fully contract, resulting in the valve maintaining its idle closed state. At low frequencies, the actuator has enough time to contract fully, thereby opening the valve completely. At the intermediate frequencies, the actuator contracts only partially, subsequently making the valve partially open.

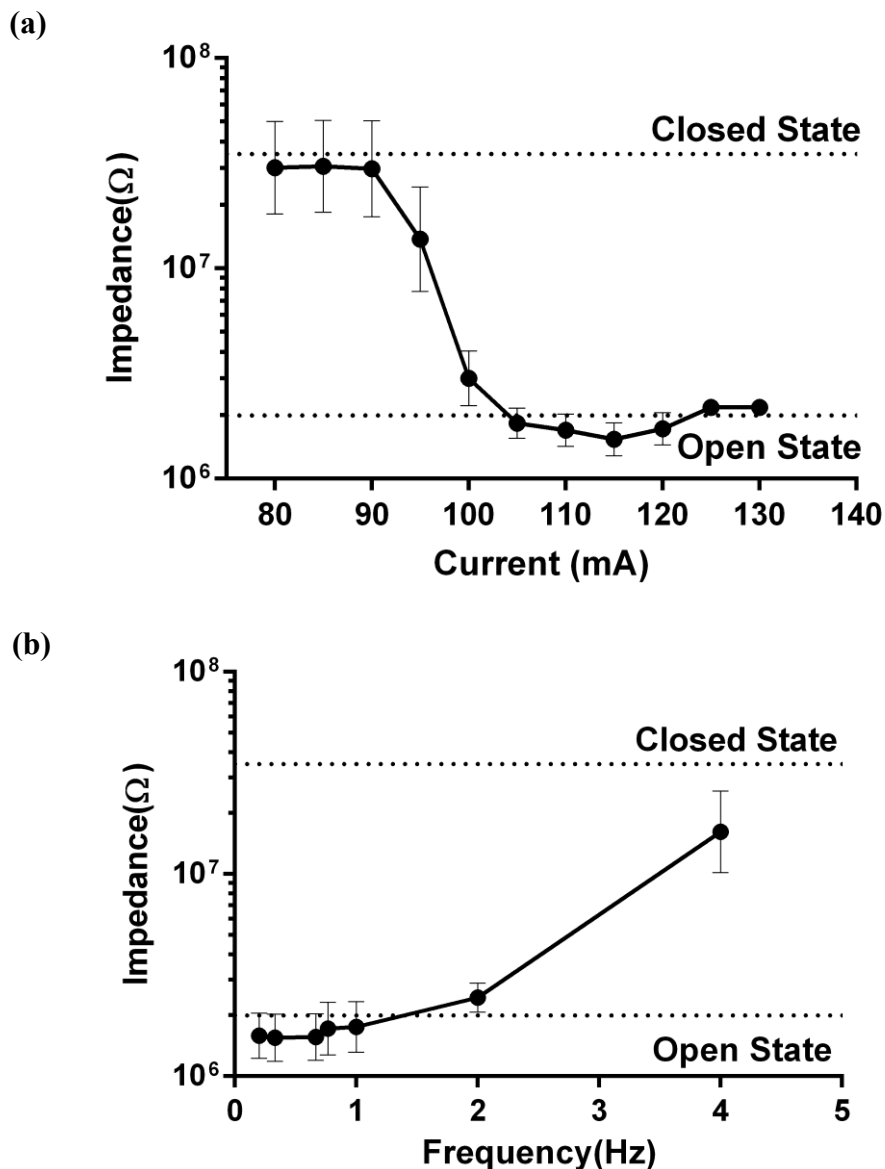


Figure 22. Valve States Based on the Shape-Memory Alloy Actuation: (a) The valve impedance as a function of amplitude of driving current flowing through the actuator. (b) The minimum valve impedance as a function of frequency of the applied pulsed signal passing through the actuator. We identify a closed valve when the measured impedance values are at least an order of magnitude higher than impedance values for the open valve. The error bars represent standard error mean for $N = 3$ chips tested.

Long-term reliability test

Figure 23 shows the variation of normalized current flowing through the valve in its open state as a function of the number of actuation cycles. For the optimized driving current of 105 mA through the actuator wire, there was no appreciable change in normalized current for one million cycles. In contrast, when the valve was driven at 160 mA, there was a significant decrease in the open valve current only after 3600 cycles, indicating that the valve did not open afterwards when it was actuated again. The failed microvalve was inspected to identify the possible sources of failure and it was confirmed that the joint between the wire and the PDMS membrane was intact. However, the Nitinol wire itself was found broken as the result of the higher driving current, in turn failing the valve actuation.

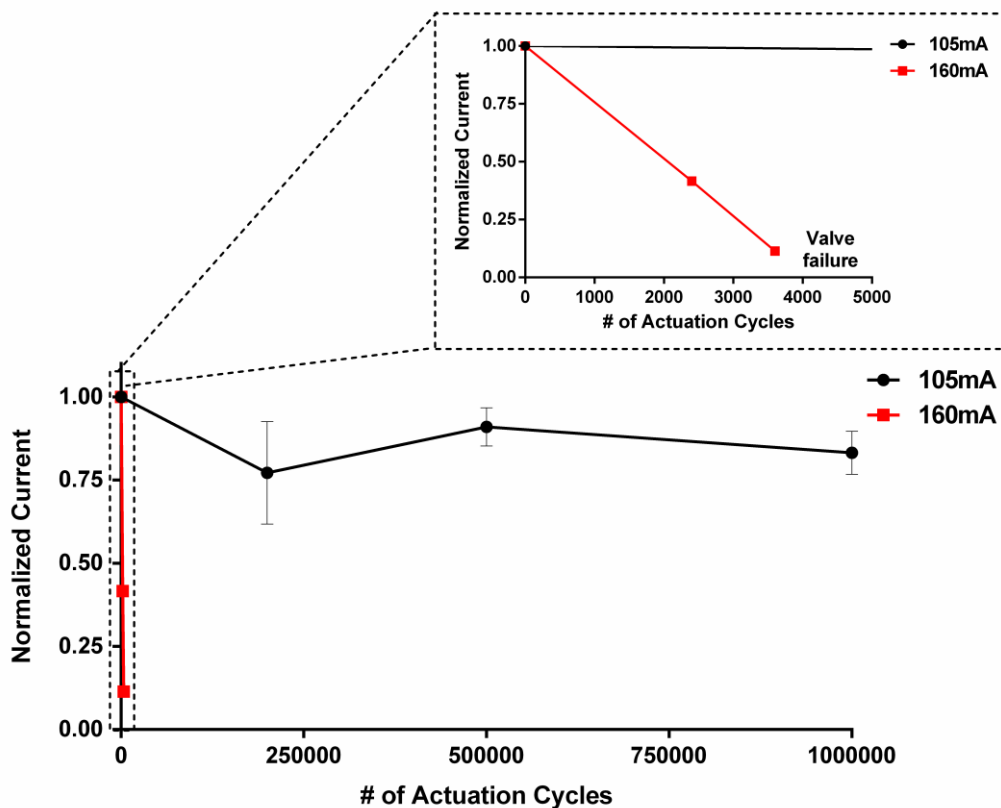


Figure 23. Long-term Testing of the Valve: Plot showing long-term testing of the plunger-membrane microvalve at 105 and 160 mA driving current. The open valve electrochemical current is shown on the y-axis, normalized to the starting current. N = 2 for 105 mA test and N = 1 for the 160 mA control.

Thus, the longevity of the valve is a strong function of the driving current and that the test and the assay are sensitive enough to detect valve failure. For optimal operation, the miniature fluidic valve design appears to reliably operate for one million cycles, when operated at driving currents of 105 mA.

Valve leakage test

The electrochemical current measured when the valve is closed represents the leakage value in our experiments with zero back pressure and was found to be substantially lower than when the valve is open. The effects of positive and negative back pressure on the overall valve leakage is important for applications which involve fluids under flowing conditions. The pressure–impedance plots are summarized in Figure 24. As the applied pressure increased from either the inlet or the outlet, the valve impedance decreased indicating the valve leakage. A threshold pressure of 1 psi forced the valve to open from the normally closed position in the forward direction (when the pressure was applied at the inlet), whereas that threshold pressure in the backward direction (when the pressure was applied at the outlet) was found to be 3 psi.

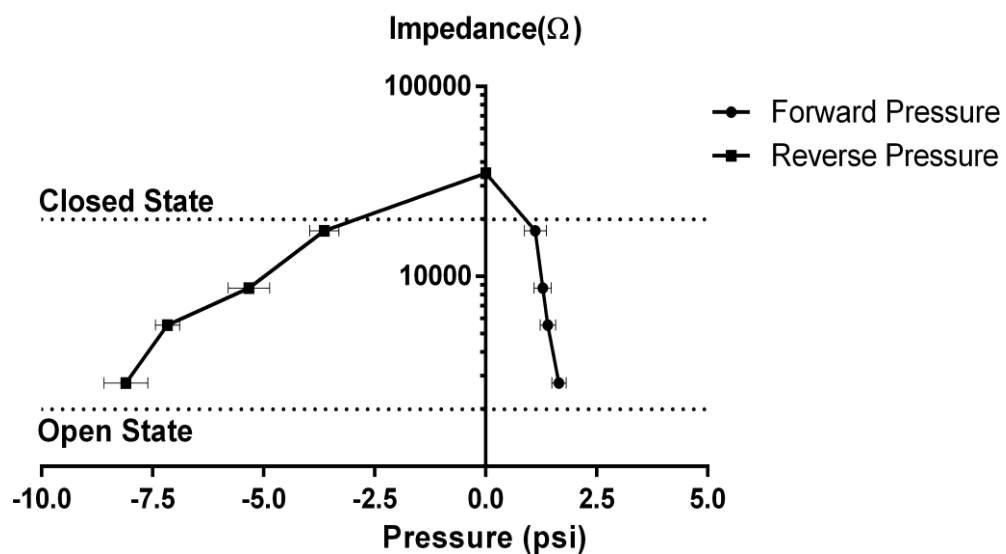


Figure 24. Leakage Testing of the Valve: Plot showing pressure–impedance characteristics of the plunger-membrane microvalve during the leakage test. The valve impedance decreases with increasing inlet (positive or “forward”) pressure or with increasing outlet (negative or “reverse”) pressure reflecting the leakage incurred. The data were obtained for N = 3.

3.5.4 Discussions

Through this experiment, a normally-closed microfluidic design for a self-actuated SMA wire actuated valve was presented. Some features of this design that contribute towards a successful implementation for the SDCS technology are mentioned. The valve is designed for larger caliber microfluidic channels ranging from 10 to 100 μm in diameter and it can be operated at up to 2 Hz at 95-mA activation current. The time taken to open the valve is ~ 0.5 s, and it takes ~ 0.25 s to close the valve. The valve is designed for a switch type of operation rather than a gradual flow control. The reliable operation of the valve was confirmed for 1 million cycles. The microvalve was manufactured using standard microfabrication steps in PDMS and thus can be integrated with other microfluidic or valve systems employing these materials and manufacturing techniques. This efficient, self-actuated valve design is the first step towards the realization of SDCS

3.6 Experiment 3: Valve Rectification

As the main purpose of the miniature valve in SDCS is basically the ability to rectify the charge-balanced alternating current (AC) waveforms into ionic direct current (iDC), it is important to scrutinize the rectifying property of the valve. For this experiment, it is hypothesized that the nitinol wire microvalve when synchronously actuated with respect to the input AC waveform, a half-wave rectification of the ionic electrochemical current flowing through the microfluidic channel would occur. As per the SDCS principle, the proposed device would utilize eight valves and four electrodes to produce a rectified iDC that is delivered to the neural tissue. The electrodes are supplied with the charge-balanced waveform and by conducting a proper switching of the valves, ionic current can be outputted.

3.6.1 Fabrication Methods

The normally-closed plunger-membrane valve system is used in this experiment for demonstrating its current capability for iDC delivery. Its fabrication has been described in the previous experiment.

3.6.2 Test and Measurement

To test the feasibility of the valve switching, a monophasic square waveform was supplied to the SMA wire, enabling it to periodically shrink and elongate. This generated a periodic force, which switched the valve between closed and open states. The state switching was observed by driving a small electric signal through the fluidic channel and the change in impedance and current through the channel was monitored. The experimental setup from experiment 2, as seen in Figure 19(b) is utilized. An input waveform of amplitude 5V at 0.5Hz was supplied to the bare metal electrodes that are embedded in the upper and lower microfluidic channels, which are filled with a 0.9M NaCl electrolyte solution. The muscle wire was also actuated by a 5 V at 0.5 Hz square waveform. Synchronization of the muscle wire actuation and the output waveform was carried out manually. For verifying the rectification process, the experiments were carried out by using both square and sine waves across the fluidic channel. A 5V input signal at 0.5Hz was applied in both the cases.

3.6.3 Results

The plots in Figure 25 shows the rectification results of an input square wave (A) and an input sine wave (B) applied across the electrolyte solution, by measuring the output across a sense resistor. As observed, there is a delay in the opening of the valve, although the signals to the nitinol wire and the fluidic channels were synchronized. This is because the nitinol muscle wire requires an onset time to undergo

phase transition, as well as a relaxation time to revert to its original length upon the withdrawal of the current. These onset and relaxation times can be clearly seen in the plots which dictate the rectification profiles significantly. The delay caused by the nitinol wire actuation results in the spike formation in the negative half-cycle. These spikes would lead to the valve being open for a while longer than required, which could potentially result in a less efficient valve. Aside from these spikes, it is observed that the valve converts the input signal into a rectified output. However, future efforts will focus on finding the accurate phase lag between the two actuation signals for more efficient ionic half wave rectification.

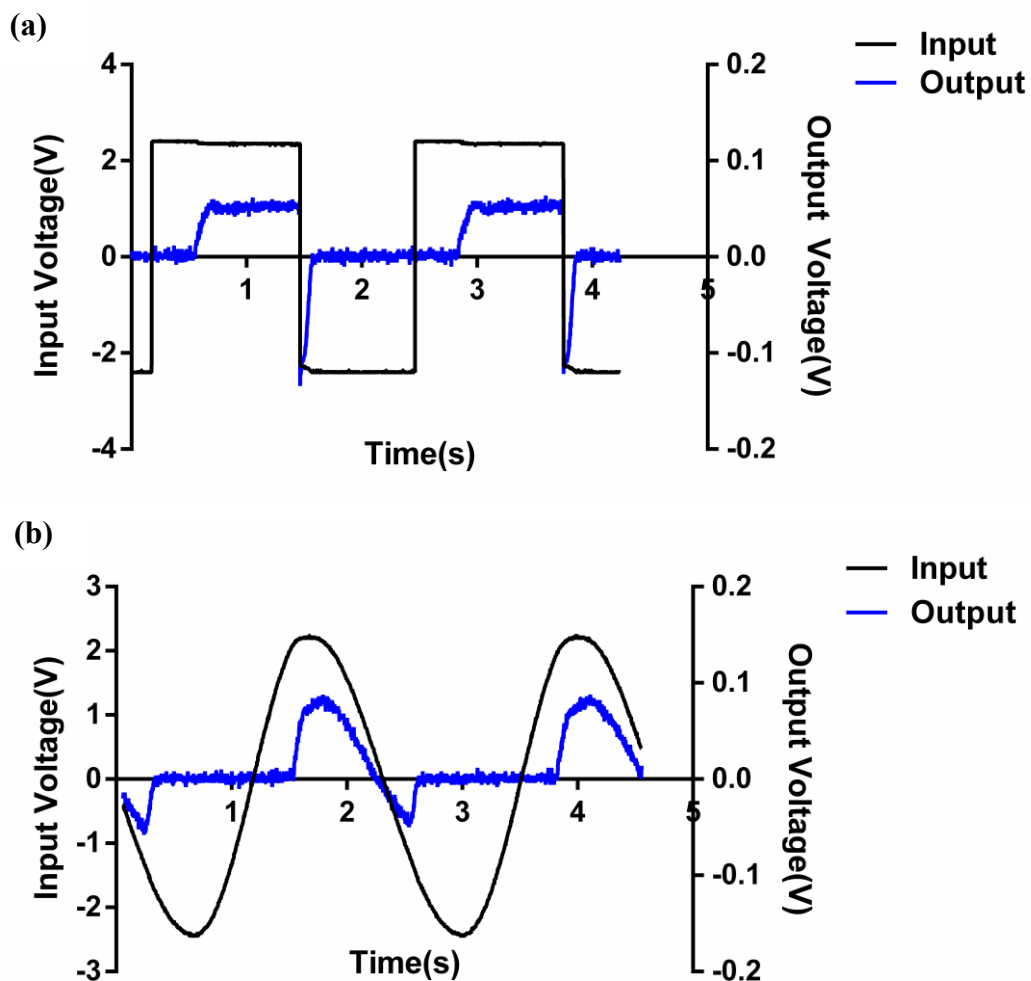


Figure 25. Valve Rectification: (a) Half wave rectification is observed when an input square wave is supplied to the fluidic channel. (b) Similar results are obtained with the application of a sine wave.

3.6.4 Discussions

These findings suggest that the designed miniature mechanical valves actuated by the shape memory alloy can be used to rectify a charge-balanced, biphasic waveform into monophasic iDC. Further experimentation is required to determine the reliability and longevity of the system, as the lifetime of each prototype device is limited by the maximum Nitinol wire operational cycles. This layered design establishes a path toward miniaturizing this valve further towards an implantable solution. Additional constraints are placed on the device that are application-specific. Current applications involve the use of DC for improving the vestibular prostheses, treating asthma attacks and for chronic pain suppression, which is the focus of this thesis.

CHAPTER 4: NEURAL INTERFACE FOR AN SDCS APPLICATION

4.1 INTRODUCTION

With over 20% of the population worldwide suffering from chronic pain, the development of various treatment modalities such as pharmacology, surgical interventions and psychological approaches to pain management have provided some respite to the suffering.[60][61] However, these methods have proven to be ineffective in a significant group of patients. An alternative technique, namely neuromodulation is often considered. Neuromodulation is defined as “the alteration or modulation of nerve activity by delivering electrical and pharmaceutical agents directly to a target area through a range of invasive and non-invasive means.” [62]

Neuropathic pain that arises from the locality of peripheral nerves is treated by several mechanisms that can be executed transcutaneously by TENS (transcutaneous electrical nerve stimulation), percutaneously by PENS (percutaneous electrical nerve stimulation) or by surgically implanted electrodes as observed in peripheral nerve stimulation (PNS). [63] Transcutaneous electrical nerve stimulation is a non-invasive, analgesic technique that delivers electrical current generated by a portable pulse generator across intact skin to activate the underlying nerves via conducting electrodes.[64] Percutaneous electrical nerve stimulation is a minimally invasive methodology performed by delivering the stimulus to needle-like temporary electrodes, which penetrate into the subcutaneous tissues close to the pain generating nerves for the course of the stimulation and are then later retracted. However, these procedures are quite cumbersome, require higher stimulation parameters due to the electrode placement away from the nerve and are more effective for the temporary suppression of pain. This led to the development of an invasive technique, namely peripheral nerve

stimulation (PNS) that overcame the shortcomings of the previous procedures and could be used for chronic pain suppression. PNS is a unique neuromodulation modality that delivers electrical impulses directly to the peripheral nerve with the aim to activate the neurons with sufficient specificity to mimic the natural activity of the nerves. [1] Here, the electrodes are implanted across or along the nerve and induce tingling sensations known as paresthesias that overlap the sensation of pain. [65]

4.1.1 Historical Implications

The feasibility of using electrical stimulation to treat pain dates back many centuries when Ancient Greek and Egyptian practitioners first used the natural physiology of an animal, such as the electrical discharge from a torpedo fish as a method for pain relief. [66] This proved to be a defining moment in history as it set the course for achieving electrical nerve stimulation for therapeutic purposes. [63], [67] Over time, the efforts towards the creation, storage and delivery of electrical energy by Alessandro Volta (battery), Pieter van Musschenbroek (Leyden jar), Michael Faraday, Benjamin Franklin and others resulted in the invention of several nerve stimulating devices. The discovery by Faraday in 1833 that an electric current can produce a magnetic field and vice versa led to the development of the *inductorium*, which served as the basis for neurostimulation for a while. The direct current inductorium device was first used to demonstrate ‘Faradization’ on a human subject. By 1863, a true precursor to the modern TENS device was constructed by Gaiffe. However, its efficacy was limited by its low electrical output of 3mA in contrast with the 90mA provided by the modern TENS unit. These early centuries of neurostimulation were centered on the phenomenon, namely ‘media medicine.’ The initial example of this concept would be of the ‘Faradaic Electrifier’, which was publicized to cure a handful of diseases, ranging from rheumatism to diseases of the liver, stomach, kidneys and even nervous disabilities.

Another such consumer-based device for pain was manufactured in 1919, known as the Electreat, turned out to be the very first high-output, battery-operated TENS unit. [68][69] However, the scientific and clinical credibility of electrical stimulation was achieved through the experimental studies conducted by Shealy *et al* for the long-term stimulation of the dorsal column more than 50 years ago.[70][71]

This 50-year old history of peripheral nerve stimulation (PNS) can be divided into several periods. The early years of using PNS for chronic pain began with the ‘Gate-Control’ theory of pain by Dr. Melzack and Dr. Wall in 1967 that described the inhibitory and excitatory relationships in pain pathways.[66] They postulated that innocuous sensory stimuli that activate the large diameter, non-nociceptive (non-painful) nerves can relieve pain. [72] They suggested the presence of a ‘pain gate’, which is closed when the pain is absent. When pain is present, the ‘gate’ is open due to the stimulation of the high-threshold peripheral afferents that conducts information about the pain. The closure of this ‘pain gate’ is due to the activation of low-threshold nerve fibres, which transmits information about the non-painful stimuli. By inserting needle electrodes through their skin to stimulate the large peripheral nerve fibres, Wall and Sweet showed that electricity could artificially close the pain gate and thus reduce pain.[73] This led to a period of semi-experimental use of PNS that lasted for around 20 years. A number of patients were implanted with neurostimulators for treatment of neuropathic pain syndromes even though PNS surgeries were quite uncommon, due to the lack of commercially available equipment. The outcomes of these procedures were not favorable. A few patients experienced prolonged remission after several weeks of stimulation and others reported device malfunctions. Another major milestone in this period was the development of implantable dorsal column stimulators that would later be known as spinal cord stimulators (SCS). [62], [63], [69]

In the mid-1980s, a surgical procedure for PNS was established. Although SCS was relatively more accepted than PNS, it still remained a preferred option when a single and easily accessible nerve was responsible for the cause of pain. In 1991, a radio-frequency (RF) SCS system was developed for the treatment of chronic neuropathic pain. The transcutaneous or RF systems were designed such that the power module, control unit and impulse generator were located externally. As the receiver is implanted subcutaneously and connected to the electrode through cables, the impulses are conveyed through the skin via a RF transmitter that overlays the receiver.[74][61] Although these RF systems delivered high-power stimulation and allowed for quick recharging through batteries, it required carrying an external stimulator and the reattachment of the transmitting antennae to the skin. [75] The introduction of the implantable pulse generators (IPG) solved the above mentioned problems and provided an appealing substitute for long-term stimulation. [69] [76] Ironically, these RF-coupled systems are the sole FDA approved devices that can be used for PNS to treat chronic pain. [75]

Three features play a huge part in fulfilling the purpose of PNS; precision of stimulation, stimulation patterns and the reliability and safety of the interface to deliver the current. For PNS to achieve its desired function, the interface has to stimulate a particular population of fibres in the peripheral nerve. This depends on the physical interaction and localization of the interface with the nerve and the anatomical organization within the nerve. The interface should not adversely affect the nerve or the surrounding tissue. Stimulation patterns are governed by the timing and frequency of the action potentials that are generated by this method and various other factors.[76] Thus, the neural interface plays a vital role in determining the efficacy and efficiency of the device.

Evolution of Neural Interfaces

Alongside the device evolution, advances in the technology of electrodes were made too. The initial electrodes used were typically wires that were inserted into the nerve or placed next to it. [74] Wall and Sweet implanted needle electrodes in their infraorbital nerves to test their gate control theory. These were later substituted by cuff-type and button-type electrodes. [73] The former is wrapped around the nerve and the latter is sutured such that it is in direct contact with the axons of the nerve. During the late 1960s, RF generator-based devices were commonly used with the nerve cuff electrodes. Although cuff-type and button-type electrodes were found to be suitable for long-term stimulation, a multitude of issues surrounding them made PNS less appealing in the early 1980s. These issues included the complexity of surgical procedures needed to expose the targeted nerve, nerve injury from electrode insertion, fibrosis, scarring, difficulties in maintaining the adequate positioning of contacts and the lack of dedicated equipment. [74]

The progression of spinal cord stimulator technology resulted in the adaption of the SCS electrodes for the PNS procedure, by mid 1980s. These electrodes were flat plate, multi-contact, ‘paddle-type’ leads that were placed adjacent to the nerve or in direct contact with the nerve trunk.[65] Prevention of the scar tissue formation between the nerve and electrode is facilitated by attaching a mesh to the paddle base, which allowed the nerve to be encased with the electrode rather than struggling with suturing issues.[63] The multi-contact feature of this innovation led to a versatility in stimulation patterns. A massive benefit of this paddle structure is its unidirectional nature of stimulation, as the contacts on the paddle are shielded by the insulative paddle backing, thereby inhibiting the possibility of stimulating the adjacent sensitive tissue. Moreover, the geometry of the paddle allows for a lower electrode migration rate.[65], [76]

However, the drawbacks, mainly the invasive implantation procedure, that eventually led to fibrosis in the long-term and the higher incidence of electrode fracture, outweighed its advantages. [75], [76]

This led to the percutaneous era, which began with the pioneering work of Weiner and Reed in the early 2000's, towards the development of a percutaneous electrode insertion technique. In this method, the electrode is placed in the proximity of the region of pain. The electrode is inserted epidurally with the help of a curved Tuohy needle and is positioned over the peripheral nerve. This ingenious technique was not only simple and minimally invasive, but also just as effective as the previously mentioned designs. [63]

Despite its vast history where some early technical complications were addressed, further snags are expected to arise with the development of any new PNS device or electrode.

4.1.2 Nerve Anatomy

The peripheral nervous system is a portion of the nervous system that is made up of cable-like structures called nerves and nerve cell clusters, also known as ganglia, that lie outside the brain and spinal cord. As peripheral nerves are associated with movement of limbs, they have a highly complex structure. The peripheral nerve trunk is well vascularized and has blood supply systems both exogenously and endogenously. Small arteries and veins from neighboring tissue space and muscular blood vessels make the exogenous vascular system and supplies nourishment to the tissues. The trunk comprises of three distinct types of connective tissues that house the exogenous blood supply as seen in Figure 26. Each axon is individually wrapped in a layer of glycoprotein, polysaccharide and collagen fiber known as endoneurium. The axons are

further surrounded by Schwann cells that create its myelination. The endoneurium also houses blood capillaries to provide the nerve with its own supply of nutrients and oxygen.[77] The individual nerve fibres are surrounded by the endoneurial fluid that acts as a blood-nerve barrier/interface and is a marker for nerve irritation or injury. It is delimited by the endoneurial vascular endothelium and the enclosing perineurium. This barrier regulates the exchange of blood-borne material such as proteins and molecules between the extracellular space and the endoneurial microenvironment.[78] [79] Homeostasis in the nerve fiber is also sustained by the endoneurium. By maintaining a small positive gradient in the endoneurial space, the exchange of material across the blood-nerve interface can occur.

The endoneurium is circumscribed by the perineurium, which encapsulates the bundle of axons collectively into a fascicle.[80] The perineurium is a connective tissue

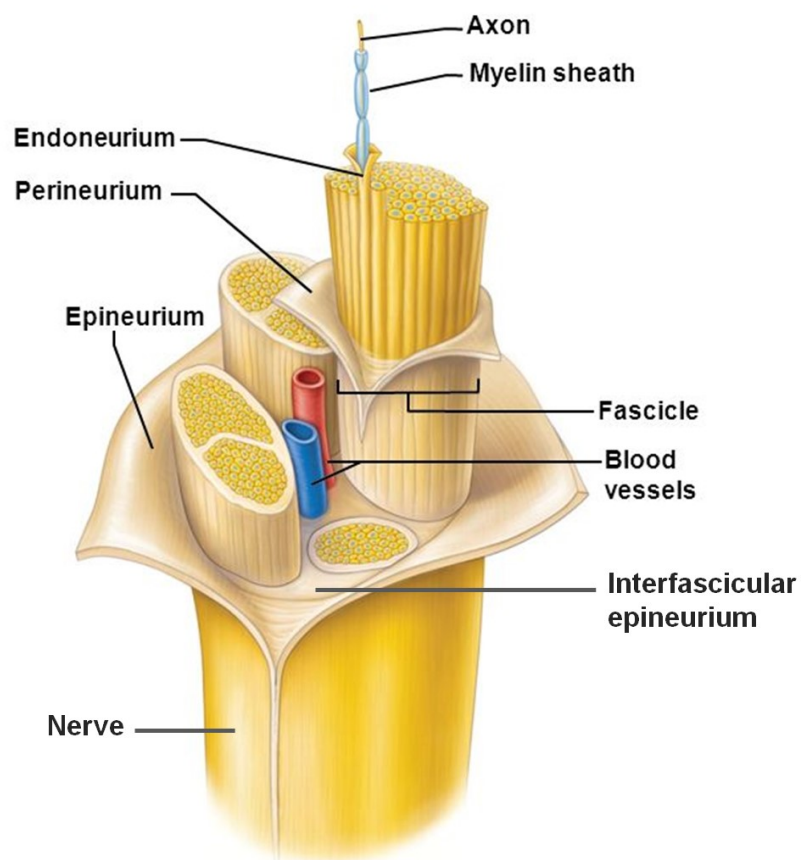


Figure 26. Neural Anatomy: The structural anatomy of a nerve fibre. Adapted from [112]

sheath composed of collagen and elastin fibers. Due to the compression-resistant characteristics of these underlying fibers, the perineurium protects its contents, the endoneurial tubes, from tensile forces. Aside from its shielding function, it serves as a diffusion barrier, guarding against foreign neurotoxic compounds.[81] When the nerve is subjected to extreme forces, the perineurium is the last to disintegrate.

Lastly, the nerve is surrounded by an outer dense sheath of connective tissue made up of irregularly arranged collagen fibres, elastin and scattered fibroblasts, called epineurium. It has both internal and external components. The internal component allows for the distinct fascicular arrangement in the nerve, while the external epineurium surrounds the nerve trunk. The internal layer also facilitates gliding between the fascicles when the nerves stretch. Both these components help in the protection of the nerve from tensile and compressive forces. Due to the lack of epineurial and perineurial layers in the spinal nerves, they are more susceptible to chronic and acute trauma.

Peripheral Nerve Injury

Although nerves have considerable tensile strength, straining them beyond a physiologically-set limit would result in the breakdown of the integrity of the nerve fiber. Deviations in their conduction properties and intraneural blood flow would occur that could ultimately lead to a loss of function.[81] A common cause of peripheral nerve injury is nerve compression. The pathological, electrophysiological and functional changes due to peripheral nerve compression have been extensively studied through animal experiments, ideally with a rat sciatic model owed to its multi-functionality.[82][78] Moreover, the rat peripheral nerves are comparable to that of a human morphologically, excluding its size and connective tissue density.[83] These

clinical experiments have shown that even a moderate increase in the pressure applied on the nerve significantly affects the peripheral nerve due to its highly vascularized structure. Compressed nerves initially show mechanical injury and nerve ischemia at the site of neural injury. Further compression results in nerve hypoxia, edema and increased vascular permeability gradually. Severe and persistent compression disturbs the neural microcirculation and cause nerve death. [78] It was seen that the chances of symptoms of nerve trauma to occur were greater extrafascicularly rather than intrafascicularly. This is because the epineurial vessels are relatively vulnerable to mechanical injury and reacts with permeability changes. However, due to the blood-nerve barrier and perineurium, the endoneurial vessels are resistant to change. As a result of neurovascular mechanical injury, there is an increase in vascular permeability that destabilizes the endoneurial microenvironment.

4.1.3 Neural Electrodes

The neural electrode is a limiting component required for achieving an efficacious link between the SDCS device and the nerve. Though neural interfaces allow for bidirectional communication through stimulation and recording, this thesis chapter is mainly focused on stimulating electrodes. The success of the SDCS prostheses is governed by its ability to elicit the necessary sensory and motor functions within the physiological limits. The positioning of a peripheral nerve interface is based on the proximity required for neuron activation, the degree of invasiveness acceptable, and the risk/benefit ratio. The two vital characteristics to be considered for a stimulating peripheral nerve interface are the following.

- (i) *Selectivity*: This term describes the population size of the units (nerve fibers/fascicles/axons) that the electrode can stimulate, without stimulating

the neighboring units. An ideal electrode requires a high selectivity. Multiple stimulating electrodes that are placed in the nerve fascicle can be distinctly stimulated if a separation of about 250 μ m between them is maintained, 'due to the stochastic nature of the distribution of axon diameters and nodes of Ranvier.'[1]

- (ii) *Invasiveness*: This refers to the implantation procedure of the electrode and the amount of penetration that is required. The degree of invasiveness can be measured by the amount of surgery required to access the site of implantation, the amount of manipulation of the nerve and surrounding tissues needed for implantation and the amount of healing time. [1]

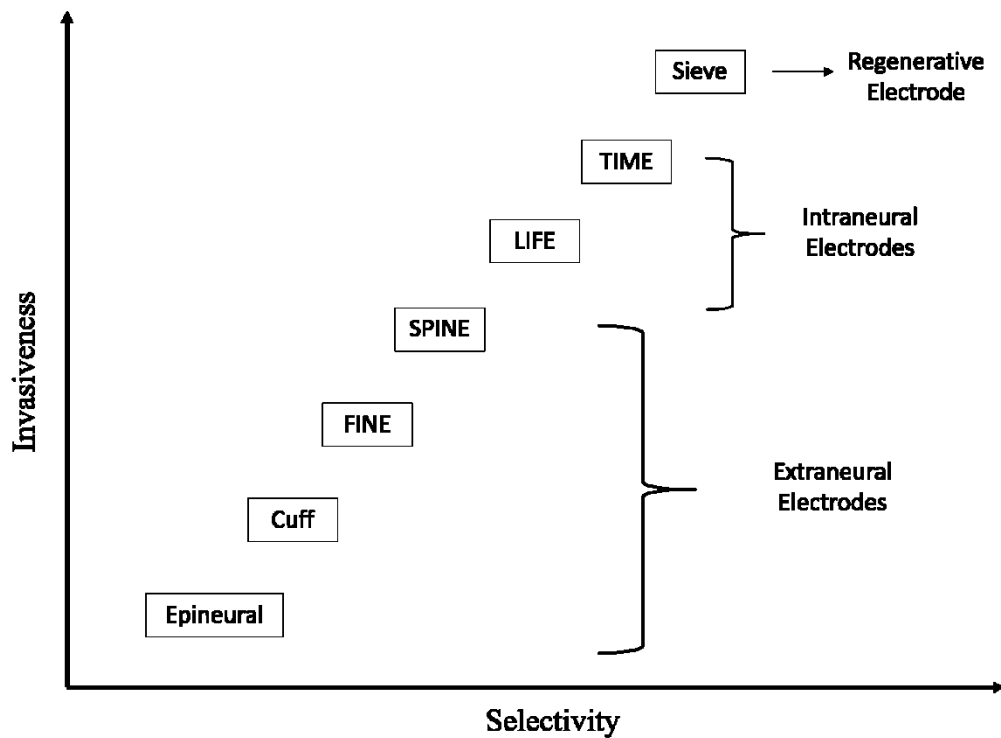


Figure 27. Types of Neural Interfaces: A plot depicting the how higher selectivity is obtained at the expense of various neural interfaces.

Efficient stimulating electrodes can be better designed through a thorough understanding of the existing interfaces and their pros and cons. Based on the degree

of invasiveness, these interfaces can be generally categorized into three: intraneural/intrafascicular, extraneural and regenerative electrodes as seen in Figure 27.

A. Intraneural Electrodes

These electrodes penetrate the epineurium sheath and are implanted within the nerve. One common type of electrode penetrates the perineurium also, such that it is in direct contact with the nerve fascicle bundles that has to be activated. These electrodes are known as intrafascicular electrodes. While the process of implantation is exceedingly risk-prone and laborious, some of the major advantages of this design includes its enhanced stimulation selectivity of fascicular bundles and the stipulation of only a small stimulus to generate the desired response. Cross-talk between the adjacent fascicles is avoided due to its fascicular specificity for stimulation and complete recruitment of the nerve fascicle can occur at low intensities. Two of the established intrafascicular electrode designs are the following:

(i) Longitudinal Intrafascicular Electrode (LIFE)

LIFEs are ribbon-like interfaces that are implanted longitudinally through the nerve fascicles such that they are weaved parallel to the nerve fibers. They offered seemingly good selectivity for stimulation of separate axonal fascicles within the nerve and its geometry renders it suitable for long-term implantation. [84]

(ii) Transverse Multichannel Intrafascicular Electrode (TIME)

TIMES are implanted transversally in the nerve so as to interface the axons within the fascicles. Their multichannel feature allows a single TIME to stimulate multiple fascicles. If the electrode contacts are aptly spaced out along the interface, different population of nerve fibers can be activated. They are relatively more invasive

than LIFE, which electrodes to a higher risk of nerve damage, but a fewer number of implanted electrodes are required when compared to LIFEs. [84]

B. Extraneural Electrodes

These interfaces are implanted externally on the nerve trunk. As seen in Figure 27, their non-invasive characteristic is directly related to its stimulation selectivity, resulting in a reduced selectivity. A few examples of this class are mentioned below.

(i) Epineural Electrodes

The epineural electrodes are a form of extraneural interfaces that are placed on the nerve and are anchored by suturing to the epineurium. Although this would not damage the nerve and allows for selective activation of nerve fascicles, improper surgery techniques can consequently result in the electrode being ripped away from the nerve.

(ii) Cuff Electrode

These are designed such that they completely encircle the nerve and they have activation sites on the inner surface, which is in contact with the nerve. Their advantages include its non-invasiveness, simplicity in handling and lesser current spread. Moreover, the electrodes can be precisely positioned over the nerve and this minimizes the mechanical distortion and probability of electrode failure. However, due to its extraneural characteristic, the selectivity is limited to large myelinated fibers or superficial fibers of the nerve. Its non-specificity leads to the need of implanting several cuff electrodes for achieving the required selectivity, ensuing intricate implantation risks. Micromotions of the cuff electrode can further damage the delicate nerve. Different configurations of cuff electrodes exist: cylindrical, spiral and helix. Two key

attributes a cuff electrode should encompass in order to accommodate for stretching and compression of the nerve are flexibility and ability to self-size.

(iii) *Flat Interface Neural Electrode (FINE)*

To address the challenge of selectivity while maintaining minimum invasiveness, a variant of the cuff electrode was designed. It targeted the elliptical shape of the nerve. The FINE was constructed such that it gradually applied a relatively high force on the nerve in order to transform the nerve from an elliptical shape to a flatter oval shape, which allowed greater access to the fascicles within. Despite a comparatively higher selectivity, without proper moderation of the applied force, nerve damage can be easily induced. [85]

(iv) *Interfascicular Electrodes*

This extraneural electrode aims to integrate the promising features of both extraneural and intraneural electrodes, mainly the design simplicity and stimulation specificity respectively. These electrodes penetrate the epineurium, without compromising the integrity of the perineurium. Hence, the electrode contacts are placed within the nerve trunk, but external to the nerve fascicle. It is also known as the Slowly Penetrating Interfascicular Nerve Electrode (SPINE), which consists of radially-extended blunt components that penetrates the epineurium. Its placement within the nerve permits for additional recruitment of nerve fibers. [85]

C. Regenerative Electrodes

This is a peripheral nerve interface design that latches on the advantages of the other two groups of electrodes. It indicates to a more biocompatible alternative, which maintains an efficient and effective neuron-electrode contact.[86] These electrodes are

placed on the proximal stump of a severed nerve allow for the regeneration of the nerves through suitable guidance channels. They are generally multi-perforated sieve electrodes that consist of an array of holes with electrodes contacts through which the axons from the stump grow.[87]

Despite the development of several approaches for stimulating the peripheral nerve fibers, a trade-off between the invasiveness of the electrode and the selectivity of stimulation exists as seen in Figure 27. To improve the feasibility of using these electrodes for SDCS, an optimization between a highly invasive electrode that provides adequate selectivity and another which is minimally invasive with reduced selectivity has to be reached.[85]

4.1.4 Aims for SDCS

By weighing the relative advantages and disadvantages of the various electrodes types and configurations, a bipolar cuff electrode was chosen for this application of pain suppression using the SDCS device. The impedance requirements for the cuff electrode was imposed by the SDCS system design from the necessity to maintain a maximum safe compliance voltage of 30V within the device, but still be able to deliver up to 200uA of output current. Due to this constraint, an impedance value of 100k Ω was assumed for the electrode to ensure efficient device operation.

4.2 DESIGN CONSIDERATIONS

An ideal electrode is hard to define, as there are a variety of parameters to be considered that vary based on the site of implantation or the application. Power consumption is another important aspect that governs the design of the electrode. The power required for the electrode to stimulate the peripheral nerve must be minimized.

This is because a reduction in the power consumption would decrease the size of the implantable device and prolong the battery life. Thus, the design and shape of the electrode are dependent on the following factors.

(a) Pressure Requirements

The implantation of the cuff electrode is a very tedious process. Care must be taken to ensure the prevention of nerve injury. Mechanical nerve injury is typically caused by a combination of factors like compression, tension, friction, traction, shear, and laceration. Although nerves are elastic in nature and have a substantial ability to resist such forces, over-expression of any, especially tension and compression can lead to serious consequences. When these forces are applied within a set boundary, the nerves respond with characteristics of an elastic material. As soon as the linear limit is reached, the nerve tissue undergoes histological changes. Initially, the endoneurial tubes rupture. Further loads damage the epineurium and perineurium layers, increase the endoneurial fluid pressure and compromise the vascular supply of the nerve. This leads to a total loss of the elastic properties for the nerve.

The extent of nerve injury is dependent on the force of compression and time of compression. Through several nerve compression studies in rat models,[81] it was observed that compression-induced trauma can lead to the demyelination and degeneration of the axons, before ultimately leading to neural death. This demyelination was observed at pressures as low as 10 mmHG (0.13 g/mm²). The intraneural blood flow was also significantly affected. When acute pressures of 20 - 30 mmHg (0.27 - 0.4 g/mm²) were applied, decreased venular blood flow and intraneural edema with epineurial scarring was detected. Further application of pressures of 40- 50 mmHg (0.54 - 0.68 g/mm²) impaired the arteriolar and interfascicular capillary flow. The capillary

flow ceased at higher pressures of 60 - 80 mmHg (0.82 – 1.08 g/mm²). This caused a fourfold increase in edema and ischemia. The threshold for acute nerve damage was observed to be around 20 mmHg (0.27g/mm²). [88] Hence, a vital parameter to be strictly followed by any neural electrode design, in this case the nerve cuff electrode is that it should apply pressures well within this pressure range after implantation, in order to ensure safety.

(b) Mechanical Compliance

A critical facet impeding the use of conventional metal electrodes for implantation is the physical and mechanical mismatch between the neural tissues and the man-made electrode. Neural tissues are in general much softer than the electrode material. [89] A measure of the stiffness of a material is provided by the Young's modulus (also known as modulus of elasticity). The Young's modulus describes the elastic properties of the material by defining the extent to which a material can withstand compression and tensile forces. A low modulus of elasticity is associated with a flexible material that changes its shape considerably under the application of stress. Neural tissue is an example of this. It has a Young's modulus of around 2.5kPa, while metals have a value that is several orders magnitudes higher. The incongruity in stiffness can cause changes in the mechanical properties of the surrounding tissues. This mechanical contrast can result in micromotion of the supposedly static electrode, which leads to inflammation at the implant site. Moreover, the response of the tissue to the recurrent motion is influenced by certain other factors such as the probing technique, geometry of the electrode, and the insertion speed of the probe. Rigid electrodes have to undergo rapid insertion speeds (>1 mm/s) for preventing vascular damage and neuron tearing.

(c) Materials

Construction of the cuff neural interface is feasible using conductive and insulative materials. To limit the current distribution profile to that of the targeted region, it is necessary to isolate the electrode from the extracellular conductive medium. This is accomplished by constructing the electrode with an insulative material such as polymers. While the polymer forms the electrode substrate for the cuff electrode to provide isolation from the surrounding tissue, the electrode contacts that stimulate the nerve must be conductive. This constitutes an application-specific problem. With the SDCS technology in mind, a material that has a high ionic conductivity is desired for the electrode contacts. The ionic property is an essential feature of this electrode, as it will be used to interface the microfluidic layer, which outputs an ionic DC, with the neural tissue.

The emphasis on the creation of a stable and conductive interface led to experimentation with a biopolymer gel, agar. Agar is a polysaccharide obtained from seaweed. Due to its high elasticity ($E = 116\text{kPa}$), low cost, environmentally-safe, porous nature, and biocompatibility, agar can be a potential substitute to the metal contacts. The agar-based hydrogel, ‘a semiflexible water filled gel with a 3D porous structure’, is formed through a hydrogen-bonded, cross-linking, self-assembly mechanism. The resulting structure is a soft and moldable medium with a high ion mobility.[90] The ionic properties of this gel can be enhanced by the introduction of sodium and chloride ion pair [91]. The ions are incorporated into the hydrogen-bonded cross-linking gel and further stabilization occurs due to the intermolecular hydrogen bonding, thus forming optimized ion transport channels. The functional enhancement is a consequence of 3 factors. Firstly, the mechanical properties of the gel are ascribed to the agar skeleton. The hydrogen-bonding augments the mechanical stability through the 3D network

formation. Secondly, this water-filled submicrometer pore network creates an ionic pathway, thereby increasing the ionic conductance. Thirdly, by adding NaCl to this gel, the ionic conductivity can be enhanced.[91]

(d) Compatibility

Biocompatibility can be defined as ‘the ability of a material to perform with an appropriate host response in a specific situation.’ [92]Biocompatibility of the neural interface is the integrative result of both the structural and the surface biocompatibility. It is quantified in terms of chemical stability and toxicity. The structural biocompatibility deals with the mechanical properties of the interface material such that it mimics the biological structure of the peripheral nerve. The surface biocompatibility is associated with the interaction of the physical, chemical and biological properties of the material with the target nerves. Hence, a material is deemed as biocompatible only if the neural environments responds with a mild to no foreign body reaction and little to no encapsulation of the interface by connective tissue occurs. Beyond its chemical and mechanical biocompatibility, the electrode should be geometrically compatible, such that its shape and size match the dimensions of the implant site.

(e) Electrode Size

All these above requirements are dependent on the size of the electrode. Some effects of a smaller electrode is the following; improved selectivity, reduced bending rigidity, decreased pressure applied on the nerve, and an increased impedance.

(f) Closure Mechanisms

Regardless of the surgical techniques involved in the electrode implantation, the high mobility of the soft neural tissue calls for proper anchoring of the electrode over

the nerve. This is especially required in cuff electrodes for circumventing the issue of electrode migration and shifts. [93] Some of the available closure mechanisms for the cuff electrode, as seen in Figure 28, involves suturing of the open ends of the cuff shut, creating hinges, following a buckle and belt clasp mechanism, or even constructing a self-adjusting spiral cuff. [94]

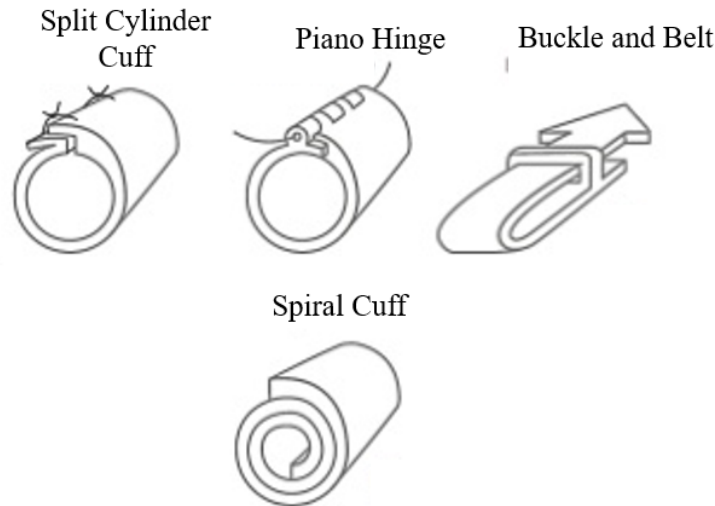


Figure 28. Closure Mechanisms of Cuff Electrodes: The figure illustrates different methods of securing the cuff electrode on the nerve. Since the inner diameter of the cuff is greater than the nerve's diameter, the cuff will not slip. The split cylinder cuff is held together with the help of sutures. Piano hinges and the buckle and belt cuff would fit like puzzle pieces. The spiral cuff adjusts its diameter based on the nerve diameter and self- curls. Adapted from [94]

(g) Bending Rigidity

While soft implants diminish the impact of the effects of mechanical mismatch on the nerve, it faces another hurdle, namely buckling. This is a form of instability caused due to the electrode geometry. As these flexible electrodes lack the mechanical stiffness needed for the initial insertion, they easily buckle or bend at the surface of the tissue. Through Euler's buckling formula, the critical load needed to cause a slender element to buckle is directly proportional to its Young's modulus.[95] Since polymers have a lower modulus of elasticity, a smaller compression load tends to cause buckling. Hence, prevention tactics in the form of supporting structures, stiffening of the electrode, or mechanically adaptable materials should be considered. Insertion aids that

function analogous to that of a Tuohy needle, wherein the catheter is introduced into the desired location through the needle and left there even after the needle is removed. A similar backing can be provided for the polymer-based electrode. The electrode stiffness can be increasing the cross-sectional area to greater than 1mm^2 or by coating the electrode surface with a thick layer ($>100\mu\text{m}$) of biodegradable polymer or sugar. After implantation, the coating would dissolve, and the electrode would return to its original thickness. An upcoming alternative to the above-mentioned techniques is a biomimetic approach inspired by the sea cucumber. These bioengineered adaptive polymers can shift from a stiff form ($E \sim \text{GPa}$) to a soft matrix ($E \sim \text{MPa}$) within minutes *in vivo*. Other such adaptive materials are shape-memory polymers and smart nanocomposites. [96]

(h) Tissue Response

Surgical actions required for the implantation of the biocompatible electrode damage the targeted neural tissues. This results in a foreign body response/reaction (FBR) that over time contributes to the reduced functionality and ultimately could lead to electrode failure due to persistent inflammation, and demyelination.[97] The intensity and duration of the inflammation and healing process is governed by the physical and surface properties of the electrode. The tissue responds to this intrusion by gradually forming a glial scar around the electrode, causing an encapsulation by connective tissue, and leading to the isolation of the electrode from the nerve.

(i) Stimulation Modes

Intrinsic consequences of the implant design are current spread and channel interaction. Current spread denotes the unintended recruitment of the neural population beyond the targeted region. The channel interaction refers to the activation of the

overlapping neural populations that are targeted by the neighboring electrodes. These factors overtly affect the electrode performance. Besides the electrode geometry, the distribution profile of stimulation along the nerve is dramatically altered by the electrode configuration. Three types of configuration exist: monopolar, bipolar and tripolar electrodes. Monopolar electrodes deliver either anodal or cathodal current. These single-pole electrodes are reliable, have a high fatigue resistance and face no complex risks during implantation. Monopolar stimulation is carried out through the current flow from the active electrode to the return electrode as seen in Figure 29. Here, the reference electrode is placed further away from the active electrode and is grounded so that the current spreads over a wider area, that could lead to recruitment of nerve fibers that are outside the target region. [98] The surface area of the reference electrode

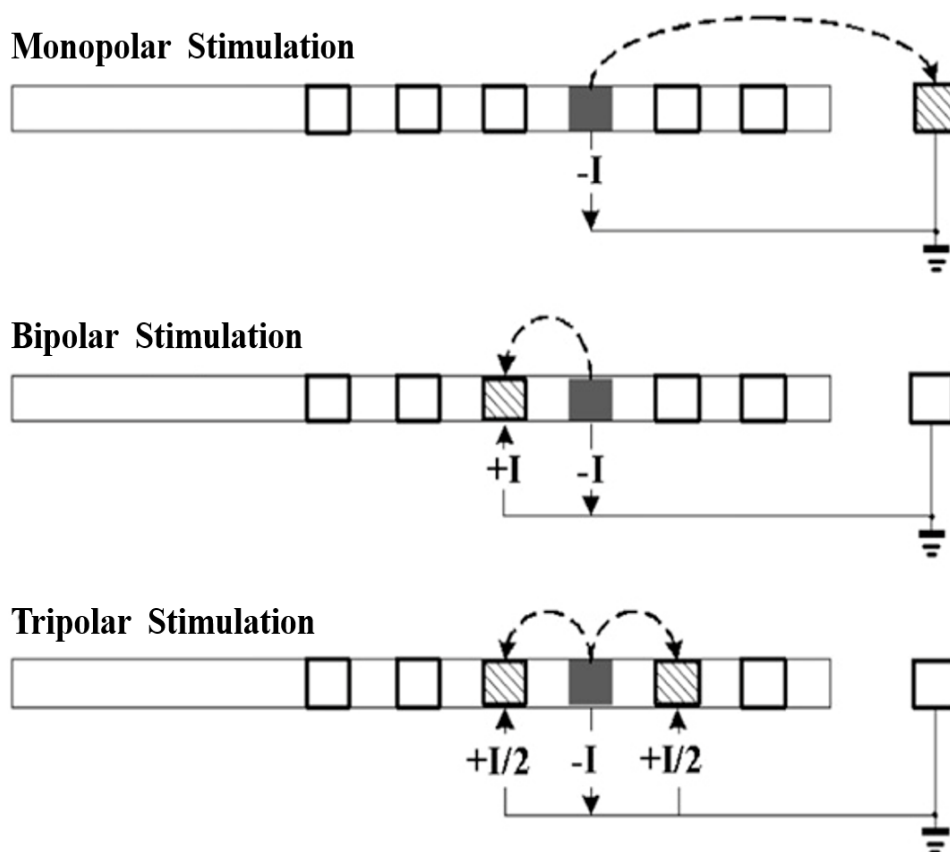


Figure 29. Stimulation Modes for Cuff Electrodes: A schematic diagram illustrating the different neural stimulation modes. The grey bars represent the active/working electrodes and the hatched bars signify the return electrodes. The solid line represents the electric circuit involving the electrodes. The dashed line indicates the current path from the active to return electrode. Adapted from [113]

is generally much larger than that of the electrode contact. This allows for a higher current density at the contact.

Current steering and focusing techniques are employed by bipolar and tripolar electrodes to limit the area of the stimulated field and allow for higher spatial selectivity of fascicles. Bipolar electrodes have two adjacent contacts, one which acts as a cathode and another as an anode, between which the current flows. The positioning of these contacts allows for a tightly focused stimulation. [98] *Comte et al* developed a simple mathematical model which calculated the spread of stimulation. He described the relationship between current spread and distance from the electrode contact. For a monopolar electrode, the current spread is an inverse squared function of distance, while for a bipolar electrode, it is a cubic function. Hence, the stimulation spread drops more for bipolar configuration than monopolar configuration, causing a localization of current.[99], [100] In tripolar stimulation, three contacts are stimulated, a central cathode that is flanked by a pair of anodes. The current amplitudes are such that the current through the flanking contacts is half of that flowing through the cathode. This results in similar potential at each end and thereby the current is contained within the electrode configuration. When the current amplitudes at the anodes are unequal, it can lead to arresting the action potential propagation. This stimulation strategy consumes at least twice as much as power as monopolar stimulation.[101] The stimulus spread also depends on the electrode material and the type of stimulating pulse employed.[99]

(j) *Implant Procedure and Removability*

An optimal design would minimize the invasiveness of the implant procedure and take into consideration the possibility of removing the electrode. This should be

carried out without damaging the neural tissue. Furthermore, it should accommodate a replacement interface. Inert polymer materials allow for this.

4.2.1 Cuff-Clamp Lead Design

Among the various electrodes types mentioned above, the cuff model was found to be well-matched with several of the essential requirements. However, designing of the same was limited by the chosen material, namely PDMS. Due to the mechanical property of PDMS and the manufacturing procedure undertaken, issues were faced with the closure of the cuff. This is because PDMS is flexible only along a dimension. Hence, the potential electrode design was unable to maintain its ‘cuff’ shape. Several closure mechanisms as mentioned earlier; suturing, buckle and belt, and buttoning were tried, but they failed to hold its structure and tearing of the PDMS membrane occurred frequently. Arising from the observation of these experimentations, a clamp was opted as a means of securing the electrode. Thus, this thesis presents a cuff-clamp lead system, which is ionically conductive and conforms to the nerve shape.

(i) Cuff Electrode Design:

Figure 30(a) represents the CAD model for the current electrode design. It has two parts connected by a thin flexible membrane, which allows the two parts to be placed on top of one another to obtain the cuff shape. Part A has two supporting structures, namely stoppers that holds the cuff in position. Part B consists of two ionic channels with extended leads needed for contact with the microfluidic device. Four design parameters were altered for the obtaining a suitable cuff electrode; length along the nerve (l_1), width (w_1), thickness (t_1), and height of the stoppers (h_1), as observed in Figure 30(c). These parameters were based on the dimensions of the rat sciatic nerve, which was used for experimentation purposes. The diameter of the sciatic nerve is 1.25

± 0.25 mm with a cross-sectional area of 1.54mm^2 . [102] According to the AAMI American National Standard for Implantable Peripheral Nerve Stimulators, the internal cuff diameter to nerve diameter ratio should be 1.5 in order to ensure safe implantation. [103] The length of the cuff (l_l) is limited by the implantation site, desired number of contacts, and contact size. Ideally a length of around 5 - 20 mm would be suitable. The width, w_l is chosen such that a distance of 0.5 mm was maintained between the edges of the cuff and that of the nerve. Height of the stoppers and the electrode thickness were selected to ensure the total height of the cuff was at least 0.5 mm greater than the cross-sectional area of the nerve. As this was an initial basic design, research was mainly focused on only certain aspects such as the optimization of the size of the electrode, while other vital features like the electrode contacts would be investigated in future trials. Due to the implant site constraints, a length l_l of 6.5mm was considered with a 2 mm spacing between the potential electrode contacts. The other parameters were

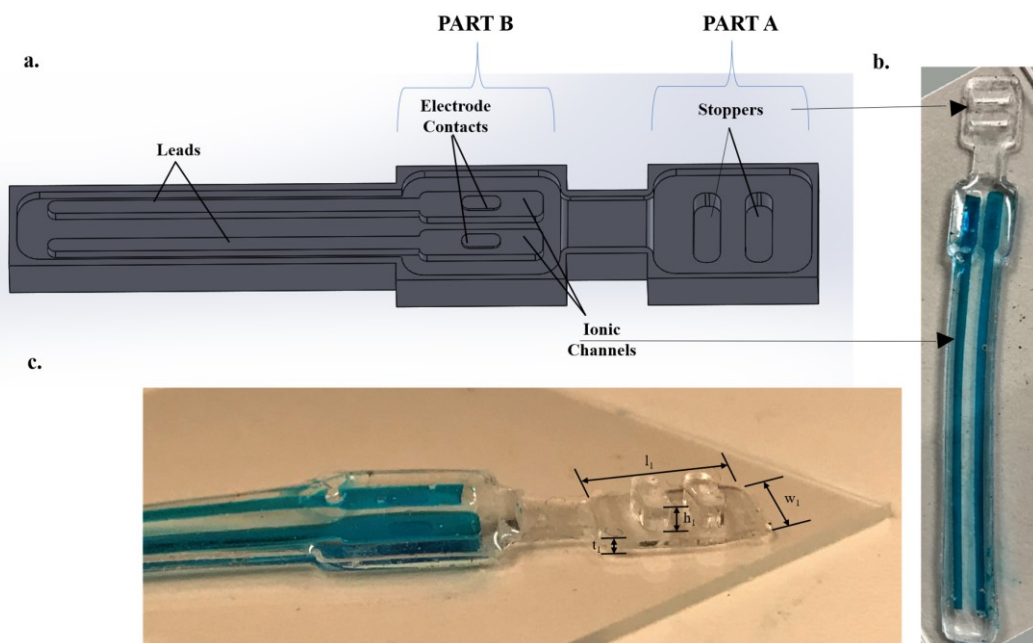


Figure 30. Cuff Electrode Design and Fabrication: (a) The 3D CAD model for the cuff electrode is shown here. (b) The image shows the result of the replica molding process with PDMS. The electrode has two fluidic channels that are visualized using a blue food dye. (c) The diagram depicts the dimensions taken under consideration for the electrode.

gauged as follows: $w_1 = 5\text{mm}$, $t_1 = 0.72\text{mm}$ and $h_1 = 1.25\text{mm}$. Therefore, a total thickness of approximately 2.7mm was obtained when the electrode was bent to form the cuff shape. The length of the leads was arbitrarily chosen as it would depend on the location of the desired SDCS implant with respect to the nerve.

(ii) C-Clamp Design:

Since the closure mechanism established for the electrode involves the use of a c-clamp, certain aspects pertaining to the length of the clamp (l_2), width (w_2), height (h_2), and thickness (t_2) are assumed to change the relative forces applied on the nerve. By adjusting these parameters of the c-clamp as seen in Figure 31(a), the forces exerted on the nerve could be controlled, while guaranteeing no movement artifacts of the cuff

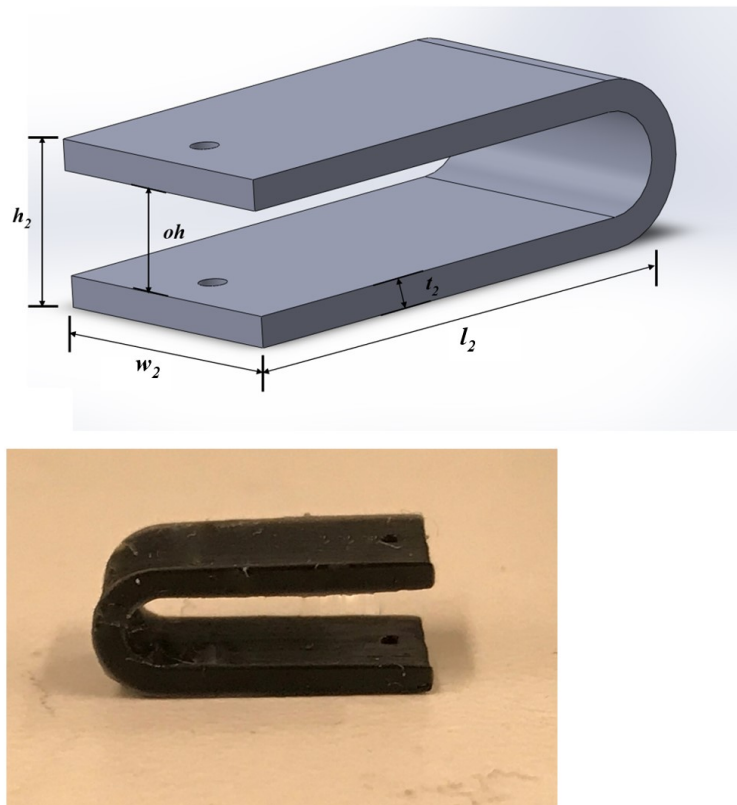


Figure 31. C-clamp Design and Fabrication: (a) The diagram shows a 3D CAD model of the clamp used to prevent electrode movement on the nerve. Described within are the parameters that are considered for the design of the clamp. (b) The photograph displays the 3D printed model of the clamp used for experimentation.

occurred. Hence, alterations to the clamp are responsible for determining if this cuff-clamp system abides to the nerve pressure threshold.

4.3 METHODS

Materials:

A photocurable polymer resin, B9R2, was purchased from B9 Creations (South Dakota, USA). Sodium chloride (NaCl) was purchased from Sigma-Aldrich. Chlorotrimethylsilane was purchased from Sigma-Aldrich and used for surface treatment. A two part 184 Sylgard elastomer kit containing poly-dimethylsiloxane (PDMS) pre-polymer mix and a cross-linking agent was purchased from Ellsworth Adhesives (WI, USA) to be used for encapsulation. Agar powder was obtained from Sigma-Aldrich and used as an electrolyte for the electrodes.

Electrode Fabrication

The cuff electrodes are made from PDMS using a soft lithography fabrication protocol, while the clamp is constructed through 3D printing. PDMS was chosen as its Young's modulus is similar to that of the neural tissue and it allows for a higher conformability than other polymers.[104] The electrode layer and the c-clamp were manufactured separately and then later assembled during testing. First, CAD designs were created using the SolidWorks software, and molds for each layer and the clamp were 3D printed (B9Creations, South Dakota) using the photocurable resin. The manufactured layer corresponding to the electrode mold is seen in Figure 30(a). Layer 1 contains the two channels, the top membrane, and the stoppers. Layer 2 is a nonpatterned PDMS base layer. The printed molds were then rinsed thoroughly in an ultrasound bath with DI water and a commercial surfactant (dish washing liquid) to

remove the uncured polymer traces. Strength of the molds were improved through post-curing them under UV light for 12 h for further solidity. The manufactured clamp is seen in Figure 31(b). To peel off the casted PDMS layers easily, the mold surfaces were treated with a corona discharge (BD-20AC, Electro-Technic products) followed by salinization with trimethylchlorosilane. A 10:1 wt.% mixture of PDMS pre-polymer and curing agent was degassed in a vacuum chamber to remove any air bubbles and poured over each mold. The assembly was baked in an oven at 90 °C for curing. The PDMS layers were carefully peeled off, and sequentially bonded together using a corona discharge to form the electrode as shown in Figure 30(b) and Figure 32(a). The assembled device was placed over a quarter dollar coin for comparison purposes in

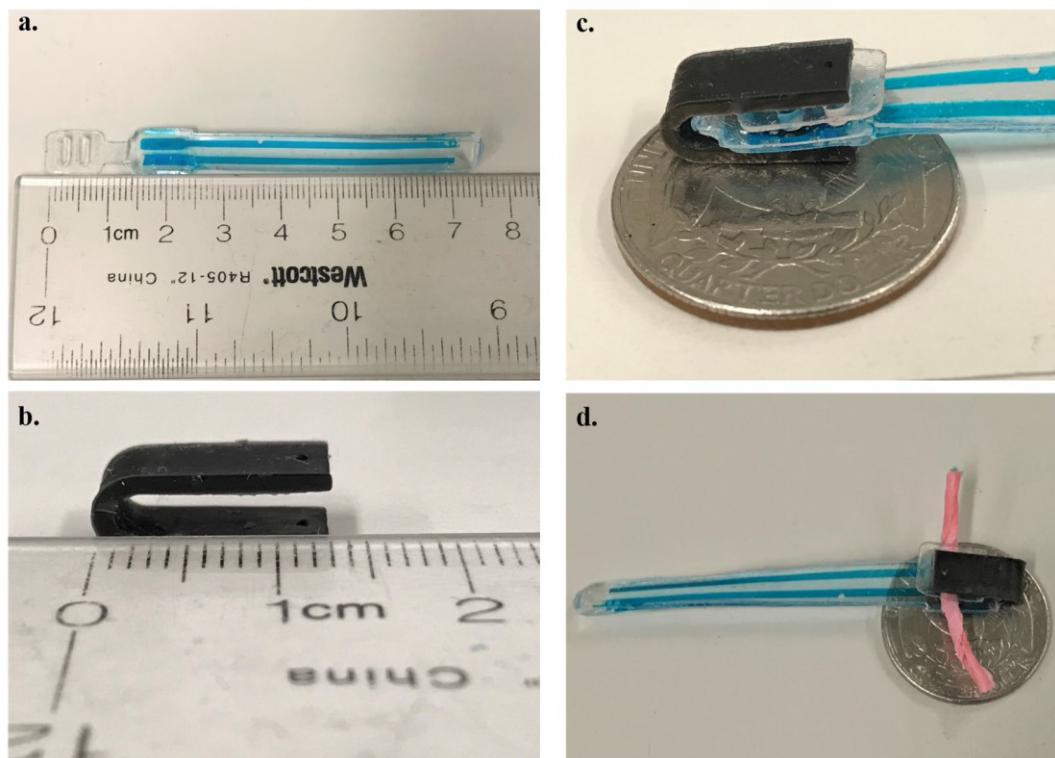


Figure 32. Final Constructed Elements of the Electrode: (a) This photo denotes the size of the cuff electrode, including its electrode wires. The two fluidic channels are filled with a blue food colouring dye. (b) Image of a 13mm wide clamp. (c) The electrode and clamp are placed over a US quarter for comparison purposes. (d) This represents the entire setup. The red piece is a wet tissue dipped in some red food colouring dye for substituting a real nerve for ex-vivo experimentation. The clamp is fixed over the nerve and the cuff electrode.

Figure 32(c) and 32(d). Further miniaturization is also possible, but its effect on the pressure of the system has to be validated.

Preparation of Gel Electrolyte

While NaCl alone can be used as the electrolyte, the effect of agar doped with NaCl is intriguing. The NaCl-agar gel electrolyte was fabricated through simple solution-mixing and heating processes. The 0.1 M NaCl solution was prepared by vigorous stirring of powdered NaCl (1.16 g) in DI water (20 mL). Agar powder was dissolved in the prepared solution of NaCl (20mL) in different wt.% mixtures (0.2%, 2% and 4%). The NaCl-agar solution was then heated in a microwave oven in two bursts of 10s each till the agar powder had completely dissolved. This warm liquid solution was injected into the two channels to provide an ion conducting pathway with a blue food color dye.

4.4 Test and Measurement

Two attributes essential for the characterization of the electrode design are warranting the apt positioning of the electrode, while maintaining the applied pressure within the defined limits. Another feature specifically pertaining to the SDCS application is the need for a high ionic conductive lead. Moreover, the SDCS device restricts the impedance of the electrode to within 100 k Ω . The cuff electrode and the clamp are held accountable for different features. The cuff electrode design can be characterized through two approaches; *in-vivo* experimentation for determination of the size of the electrode and analysis of the electrode impedance using a frequency analyzer. The clamp was evaluated through force measurements for pressure calculations. The experiments undergone for the cuff-clamp lead characterization are detailed below.

(a) In-Vivo Characterization

For optimizing the electrode design in terms of the dimensions, the adult rat sciatic nerve was used as an experimental model. Since the testing was utilized for qualitative characterization of the electrodes, rat cadavers were obtained from Department of Otolaryngology, Johns Hopkins University. The right and left hind legs of the rat were shaved using electric clippers. This region is disinfected with isopropyl alcohol. Under sterile surgical procedures, the surrounding layers of tissue were dissected till the sciatic nerve was exposed from the sciatic notch to the knee. The cuff electrodes were then snugly implanted on the right and left cadaveric sciatic nerves, proximal to the sciatic nerve bifurcation. The implant procedure involved sliding the width of the cuff below the nerve till the nerve was placed perpendicular to the two ionic channels and contacts. The end was folded over the top of the nerve to get a cuff-like figure such that the nerve was placed between the two stoppers. The height of the stoppers was varied and the impact of the same were assessed through qualitative evaluation. Finally, the clamp was placed over it to maintain the proper contact between the electrode and the nerve. Precautions during implantation were ensured to minimize the manipulation of the nerve. Through this procedure, the dimensions of the electrode were characterized based on visual feedback.

(b) Impedance Testing

The impedance of the electrode plays a dominant role in the power consumption of the implantable SDCS device. By reducing the electrode impedance, the power consumed is further decreased. Based on current literature, two premises were shaped. One examines the influence of the electrode size on the impedance. Since the electrode is basically a conductor between the microfluidic device and the nerve, it would abide

by Ohm's law, which suggests that an inverse relationship exists between area and impedance. To evaluate this, two electrodes with channel areas 0.375 mm^2 and 0.5 mm^2 were constructed. A tube with a larger cross-sectional area of 7.8 mm^2 was also tested. Constraints on the length and width of the channel were placed due to the size of the electrode and the site of implantation in a rat. By increasing the depth or thickness of these channels, the risk of fabricating a relatively more rigid and non-conforming electrode looms, that could potentially damage the nerve. Hence, the areas taken into consideration were limited to 0.375 mm^2 and 0.5 mm^2 . The microfluidic channels of the electrode and the tube were filled with 0.1 M NaCl solutions that served as a medium for ion conduction. These channels were further visualized using a blue color food dye. To measure the impedance, the electrodes were hooked up to an impedance frequency response analyzer (C60, Cypher Instruments, UK) with standard bare metal wires, which outputted the impedance values at different frequencies ranging from 10 Hz to 10 MHz .

The second theory explores the relationship between the electrolyte composition and the impedance. Electrolyte constituents were varied by the addition of agar. To test whether agar improves the conductivity of the electrode, the same three samples were filled with different weight percentages of NaCl-doped agar (0.2% , 2% and 4%). Since impedance is a factor of ion mobility, it was hypothesized that an increase in the agar concentration would increase the conductivity. This is based on the understanding that with a higher agar concentration, for every unit volume of the gel, agar particles would occupy most of the space. [105] This results in a viscous electrolyte, which diminishes the flow of ions through the system. Hence, the conductivity should decrease, thereby increasing the impedance. The theory was tested by connecting these samples to the frequency analyzer and generating the impedance

vs frequency graphs for further analysis. Testing experiments were repeated three times with a newly fabricated electrode for each test to encompass the experimental uncertainty in their manufacturing.

(c) Pressure Calculations

In order to calculate the pressure applied on the nerve by the cuff-clamp system, the effects of the forces were examined quantitatively. As the clamp is constructed from a more rigid material, the weight of the PDMS-based cuff electrode was negligible when compared to the clamp. It can, thus be assumed that the forces exerted on the nerve was entirely because of the clamp. Hence, an indirect and quantifiable characterization of the clamp was carried out through a relatively simple setup.

A schematic of the experimental setup is shown in Figure 33. The initial heights, $h_{initial}$, for the clamp was measured and recorded using a Vernier caliper. Now, the cuff electrode was wrapped around a reproduction of the nerve and placed within the clamp.

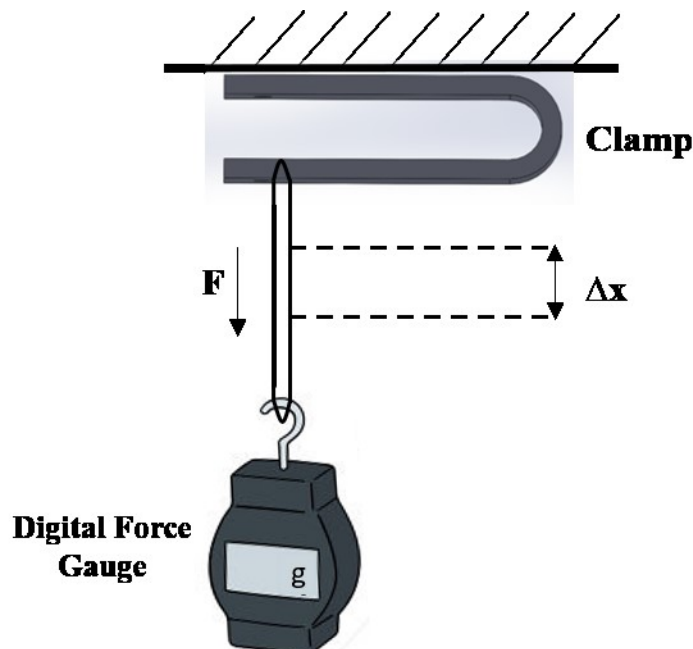


Figure 33. Experimental Setup for Force Testing of the Clamp: An experimental setup used to quantify the force applied on the nerve. One end of the clamp is fixed, and the other end is connected to the micromanipulator through a wire. The displacement (Δx) is varied in equal increments, and the corresponding force is obtained from the force gauge.

Once again, the height of the clamp with the cuff and nerve, h_{final} , was approximately calculated using the Vernier caliper. The difference between the opening heights, d , was evaluated and noted and this corresponded to the displacement of the clamp. For the consequent force measurements, a 50 μ m suturing wire was looped around one of the open ends of the clamp and to a micromanipulator, while the other end was securely attached to a flat surface. By displacing the wire in a controlled manner, a force was generated that was followed by an increase in the opening height of the clamp. These resulting pull forces were measured using a digital force gauge. The force linked with the displacement, d , signified the extent of stress the clamp enforced on the nerve. When the electrode was placed within the clamp, it was assumed that most of the force applied on the nerve is concentrated along the width of the clamp. As the cross-sectional area of the curve portion was smaller than that along the width of the clamp, the curved portion was presumed to have an insignificant effect on the nerve and thus its effect was neglected. Hence, the pressure can be calculated through its standard formulation of force/area. In this case, the perpendicular force applied on the nerve was distributed evenly, mainly across the clamp's width. Thus, the area under consideration would be twice the cross-sectional area of the rectangular surface of the clamp.

The pressure exerted by the clamp on the nerve must be well within an allowable pressure range, set by the nerve. While several parameters of the clamp can be varied to bring about a change in the pressures, the opening height and the length of the clamp would have a greater influence in the deformation of the PDMS electrode placed within it, thereby the nerve. From Figure 30(a), the thickness of Part A and Part B are 0.65mm each. Since the electrode is placed between the supports of Part A and then folded over the channels of Part B, the total thickness of the electrode would be the sum of thickness

of Part A (0.72mm), Part B (0.72mm) and the supports (1.25mm), ie. 2.7mm. The clamp has to fit around this entire system to hold the nerve and electrode in place.

(i) Effect of Clamp Opening Height

Three clamps were manufactured with varying opening heights (*oh*); narrow, medium, and wide clamps. The dimensions were defined in Figure 31(a). The opening heights opted for testing were 2.55 mm ($OH_{2.55}$), 2.7 mm ($OH_{2.7}$) and 2.85 mm ($OH_{2.85}$), while keeping the other dimensions constant throughout. A smaller opening height would damage the nerve.

(ii) Effect of Clamp Length

Similarly, the length of the clamp would have a considerable effect on the applied force. This can be investigated by designing three clamps with various lengths: short, medium and long clamps. The electrode is 6.5mm in length. Hence, three clamps of 2.85mm opening height with 5 mm (L_5), 6.5 mm ($L_{6.5}$) and 8 mm (L_8) lengths were fabricated and tested. Ideally, it would be expected that the longer the length, the lesser amount of force would be required. Testing experiments were repeated three times with a newly fabricated electrode and clamp for each test to encompass the experimental uncertainty in their manufacturing.

4.5 RESULTS

(a) In-Vivo Characterization

The implantation of the prior electrode designs visually damaged the nerve as there was plenty of nerve movement in the form of twisting and elongation of the nerve. Hence, an additional structure, the clamp, was necessary to prevent both electrode and nerve motion as seen in Figure 34. By positioning the nerve between the two stoppers,

the movement of the nerve was further restrained as these stoppers provided the supporting role for the nerve. The impact of the height of the stoppers on the nerve was observed. Since the rat sciatic nerve has a diameter of 1.25 ± 0.25 mm, heights of 1 mm, 1.25 mm, 1.5 mm and 1.75 mm were sampled. With the 1 mm height stopper, the placement of the clamp caused a relatively strong reshaping force to be applied on the nerve, as there was a noticeable change in the nerve's cross-section. Although the nerve seemed to be securely fastened with no movement artifacts, considerable nerve damage would be imminent. The 1.5 mm and 1.75 mm heights averted the enfolding force but resulted in twisting of the nerve. Since the nerve was not snugly fitted between the stoppers, a torsional force acted on the nerve, causing it to deflect significantly. This torsion eventually led to shear stresses on the nerve that would harm the nerve. The space surrounding the sciatic nerve is composed of tissue and fluid, which limits the area needed to implant these electrode sizes. Moreover, nerve motion also stemmed from the lack of friction. The PDMS electrode provides considerable friction when in contact with the nerve, which would grip the nerve in position. The heights of these stoppers allowed ample room for the nerve to avoid contact with the PDMS electrode. This prevented the necessary friction and would also require larger electrode contacts for the iDC flow. The 1.25 mm stoppers provided sufficient friction to hold the nerve, and not cause any significant reshaping. It could be noticeably discerned from the previous heights as the nerve was secured between the stoppers, with only slight movements. These qualitative results conclude that the 1 mm, 1.5 mm and 1.75 mm heights of stoppers would result in irreversible damage to the nerve and could not be used in the electrode design.

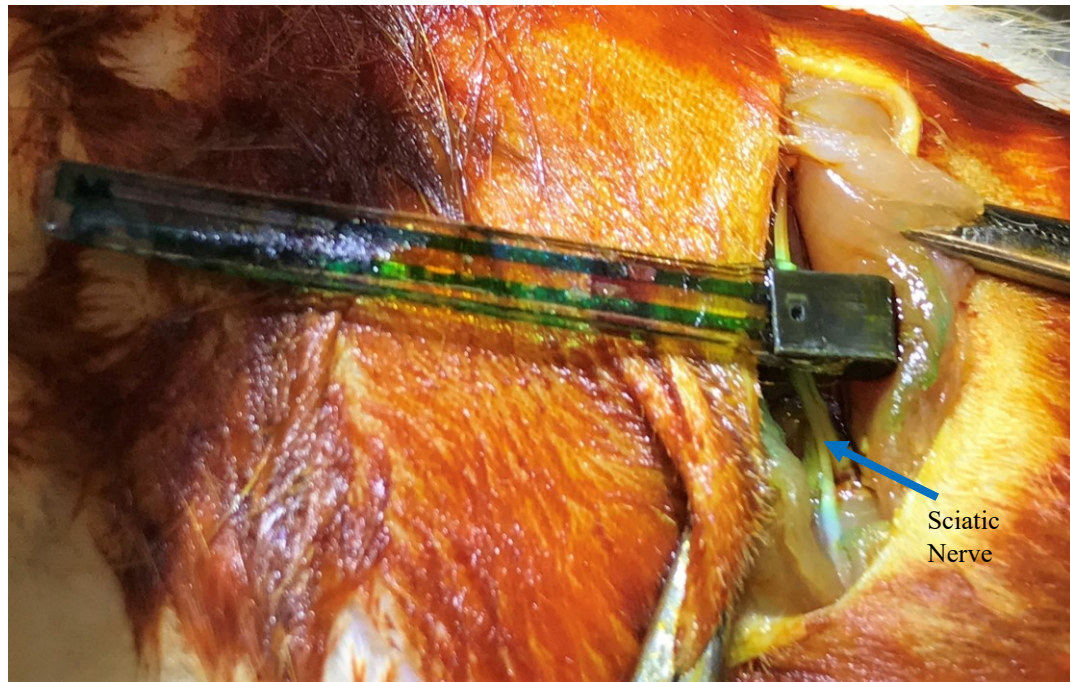


Figure 34. Implantation of Cuff-Clamp Lead System: *In-vivo* characterization of the cuff electrode was carried out through the implantation of the same over the sciatic nerve of a rat. The extended leads are to be connected to the microfluidic layer.

(b) Impedance Testing

(i) Effect of Channel Size

The impedance frequency response *analyser* characterized the impedance of the system for frequencies ranging from 10 Hz to 10 MHz. However, as this electrode aims to deliver ionic direct current, the impedance values at low frequencies of around and below 10 Hz only need to be evaluated. Additionally, ongoing experiments into the safety and practicality of safe DC for the various applications utilize micropipette tips with a cross-sectional area of 200 μm and are filled with NaCl-agar gel. The impedance of these tips, which is approximately 100 k Ω , symbolizes the experimental electrode impedance. By experimenting with different channel cross-sectional areas, the impact of the same could be examined in the plot of Figure 35. As observed, an increase in the cross-sectional area of the channel brings about a decrease in the impedance. This

is because a larger surface area allows for a larger concentration of the electrolyte, which permits more solute ions to pass through and thus reduces the impedance. It can be perceived that a 20x increase in the channel area, from 0.375 mm² to 7.8 mm², brings around a 10x decrease in the impedance. However, the difference in impedances for channel areas of 0.375 mm² and 0.5 mm² was quite small. As the distinction between these areas were quite marginal, the impedance change was minor too. To further strengthen the premise relating the area and impedance, the method was repeated for 2% agar, 0.2% agar and 4% agar. The findings showed a similar trend for the plots with respect to using a purely saline electrolyte.

(ii) *Effect of Electrolyte Composition:*

The plot in Figure 35 also demonstrates how the composition of the electrolyte alters the impedance of the system. The 0% agar solution represents a 0.1 M saline solution that was filled into the electrode channels. The inclusion of agar into the

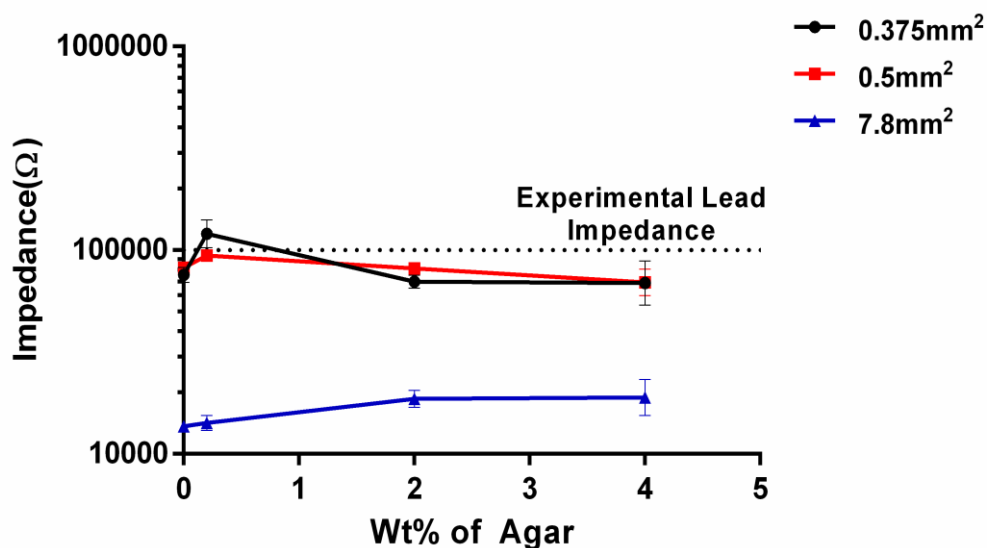


Figure 35. Effect of Area and Electrolyte Composition on Impedance: The plot describes the influence of the electrolyte composition on the impedance of the electrode for various channel sizes at 10Hz. The experimental electrode impedance refers to the impedance of the currently used electrode in experimental studies. It refers to a threshold value below which the feasibility of the electrode for delivering safe DC has been validated.

electrolyte does not significantly vary the impedance of the system as seen with the trifling change in values from 0% agar to 4% agar electrolytes. A similar inclination was detected for all the channel sizes taken into consideration. This disproves the earlier premise, which stated that an increase in agar concentration would increase the impedance significantly. A possible explanation for this trend could be the properties of agar. Agar is porous in nature and its porosity is directly related to the concentration. However, various other factors such as the temperature, pH influence the gelation process, which governs the viscosity of the gel. [106] The experiments conducted were not regulated for those factors. Furthermore, the viscosity of the gels slowly increases with time. As the experiments were conducted without any regulation of the other governing factors and were done within the span of minutes, sufficient time was not provided for the gel to become more viscous, which would then increase the impedance. Hence, there was no statistical difference observed between a purely saline electrolyte and a gel-based electrolyte. Furthermore, with time, degradation of the gel can occur due to the loss of moisture, as the electrolyte is mainly deionized water. Thus, their use for chronic studies could be limited if a solution to the evaporation or a method of replenishing the electrolyte is not established.

(c) Pressure Calculations

(i) Effect of Clamp Opening Heights

Through the strain analysis set-up, the forces that were exerted by the clamp were recorded. When an electrode was inserted in the clamp, these forces could be translated to the force experienced by the nerve. The plots shown in Figure 36 defines the trend of force and displacement when the opening height of the clamp was varied. It proves the hypothesis that the opening height dictates the applied force and hence the pressures. Figure 36 (top) describes this relationship. Force-displacement relationships

of these clamps conclude that as the opening heights were increased from the narrow clamp to the wide clamp, the forces required to produce a necessary displacement was decreased. The force required to bring about a particular displacement was the greatest for the narrow clamp of 2.55 mm height. Moreover, a considerable amount of force was required to properly position the electrode of thickness 2.7 mm within it. Since the experimental setup involves one end of the clamp to be fixed, the process of inserting the electrode within the clamp generates additional stress on the untethered, inner surface, causing a large displacement to occur as seen in Table 1. This acts as a

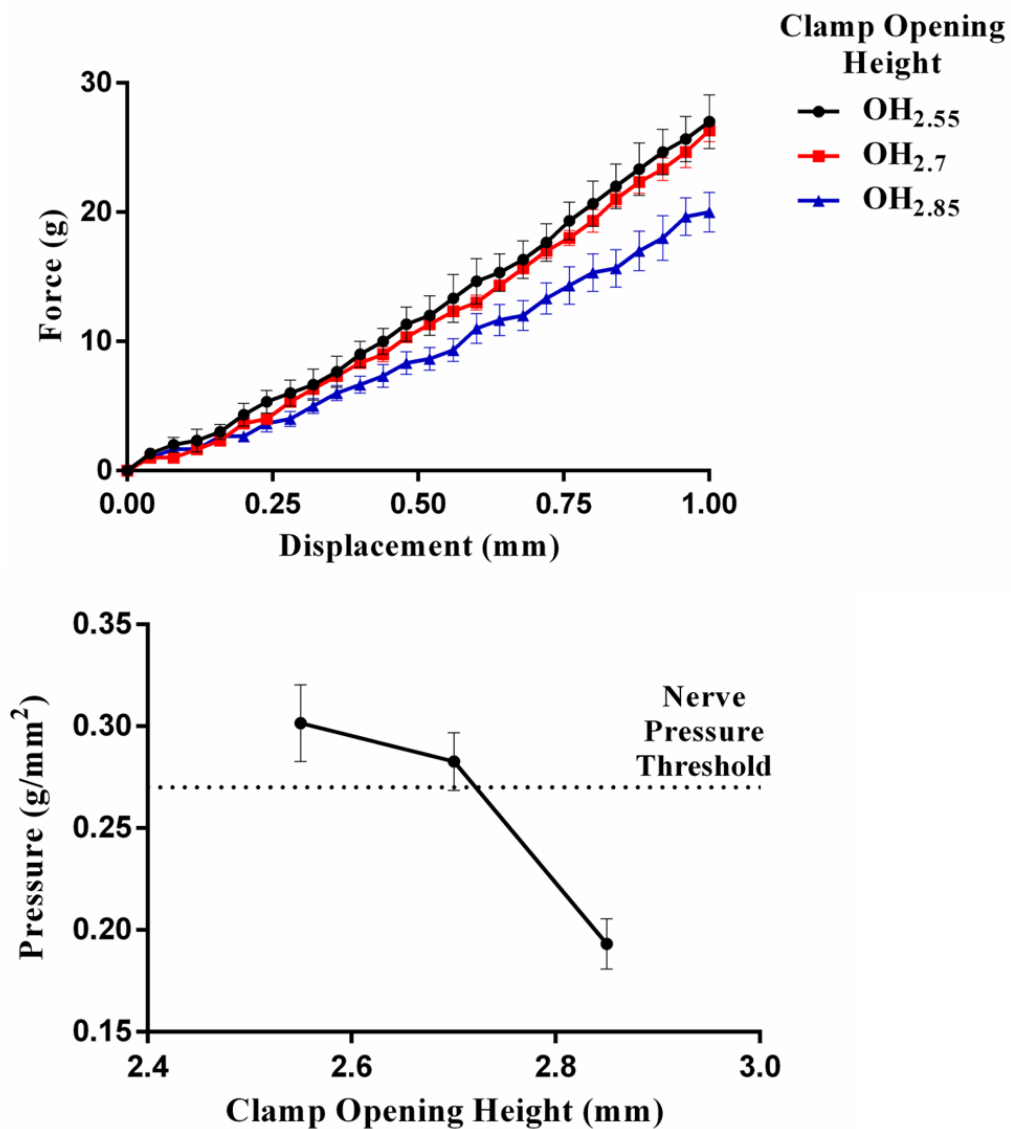


Figure 36. Characterization of Clamp's Opening Height: (top) Force-displacement characteristic plot. **(bottom)** Pressure plot for clamps with different opening heights. N=3 clamps were tested for

downward force on the electrode. The visibly deformed the PDMS electrode would flatten the nerve beyond its standard oblong shape.

The medium clamp's opening of 2.7 mm corresponded to the overall thickness of the electrode. However, there was only a slight difference in the forces experienced by the electrode in comparison to the narrow clamp. The hysteresis plot of the clamp as seen in Figure 37 could provide an explanation for this. The clamp was constructed with a rigid polymeric material, which causes the clamp to remain misshapen once the loading force was removed. Although the experiment was repeated with 3 different clamps, any small force could warp the clamp. Over time, the manually conducted experiment accumulates these shifts and could cause significant changes in the recorded forces. Furthermore, due to the semi-automatic manufacturing process, minute variations in the electrode thickness could arise that further deforms the electrode. In contrast to the narrow and medium clamps, the wide clamp was subjected to a significant decrease in the force. The little gap between the electrode and the clamp accounted for an appreciably lesser force being applied on the clamp, causing smaller

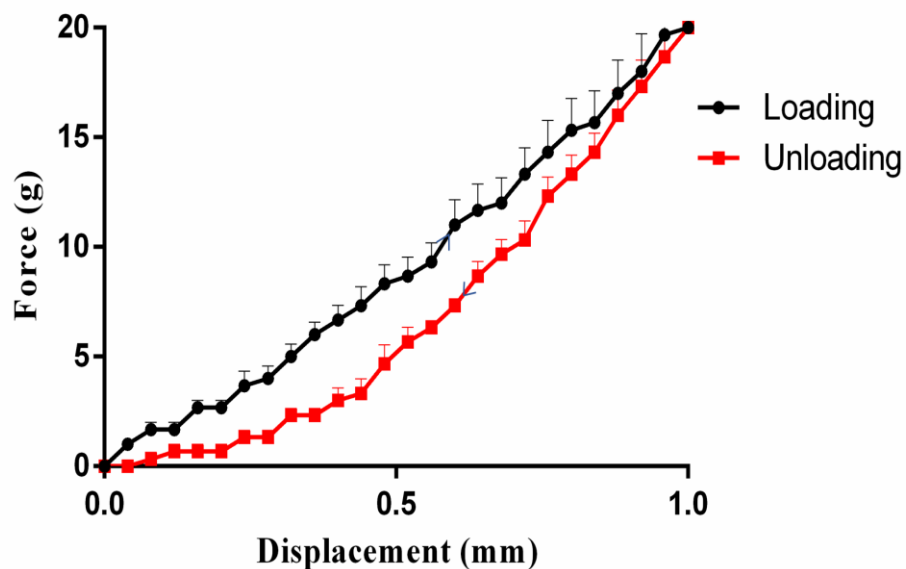


Figure 37. Hysteresis Plot: The plot shows the hysteresis loop for the clamp during loading and unloading. The clamp does not return to its original shape at the end of the process.

displacements Hence, for any displacement, a reduced force was observed for the wide clamp.

Table 1 depicts the resulting outputs of this experiment. By following the experimental procedure, the average displacement, forces, clamp area and pressures were measured. Securing the electrode within the clamp causes a change in the final

TYPE	AVERAGE DISPLACEMENT (mm)	AVERAGE FORCE (g)	CLAMP AREA (mm²)	AVERAGE PRESSURES (g/mm²)
OH _{2.55}	0.83	21.33	70.74	0.3
OH _{2.7}	0.8	20	70.74	0.28
OH _{2.85}	0.73	13.67	70.74	0.19
L ₅	0.77	20.33	54.24	0.375
L _{6.5}	0.73	13.67	70.74	0.193
L ₈	0.7	11	87.24	0.126

Table 1. Pressure Calculations: The table displays the experimental outputs required for the calculation of pressure. The displacement denotes the difference in the initial and final heights of the clamp. The corresponding forces were measured using the digital force gauge. The pressures were calculated by the formula Force/Area. N=3 clamps were tested for each opening height and length.

height of the clamp. The average displacement was obtained by subtracting the initial height of the clamp without the electrode from the height of the clamp when the electrode was properly inserted. The corresponding force was measured from the force gauge and then the pressures were calculated.

Figure 36 (bottom) shows the variations of pressure for various opening heights of the clamp. From the literature, the pressure threshold that a nerve can withstand was set as 20mmHg (0.27g/mm²). As expected, the pressure dropped by half, from 0.3 to 0.19 g/mm², when the opening height of the clamp was increased from 2.55 to 2.85 mm. Although the cross-sectional areas for the clamps were the same, the decrease in pressure correlated to a decrease in force. Since the aim of the characterization was to minimize the pressure applied on the nerve, the wide clamp (2.85 mm) was selected,

and further characterization was carried out to determine the parametric values of the clamp needed for a feasible design.

(iii) Effect of Clamp Length

It was presumed that the length of the clamp would have a substantial effect on the pressure. Figure 38 (top) portrays the effect the length of the clamp would have on the nerve. As observed in the previous force-displacement characteristic plot; an increase in the clamp length results in a corresponding decrease of the force. When the short clamp of length 5 mm was displaced, a sharper increase in force was observed with increasing displacement. Since the clamp had a smaller cross-sectional area, it could barely cover the electrode. When the electrode was folded, a large stress was applied on the thin connecting membrane between Part A and Part B. The flexible nature of PDMS would cause the electrode to push against the clamp for it to return to its original position, thereby generating additional stress on the inner surface of the clamp and displacing it further. Although the weight of the PDMS electrode was assumed to be negligible when compared to the clamp, this upwards force of the electrode could possibly cause miniscule motions of the clamp, which would be detrimental to the nerve. By using this cuff, it could prove to be challenging to prevent this movement of the electrode and the nerve. Hence, this design would not be suitable for further implantation in a nerve. A medium clamp of the same length as that of the electrode resulted in a lower value of force for the same displacement. As both the electrode and clamp had similar cross-sectional areas, the forces should be evenly distributed along the clamp's surface. The long clamp of length 8 mm gave rise to even lower forces. This occurs due to the distribution of forces over a larger surface area. Before the feasibility of these designs can be verified, the pressures plot was also analyzed.

Figure 38 (bottom) summarizes the effect of the clamp length on the pressures. The applied pressures decreased with the clamp's length. A 3.5 mm increase in length decreased the pressure by three times. Although the cross-sectional areas were increased towards the long clamp, there substantial decrease in force of the medium and long clamps resulted in pressures below the nerve's threshold. However, a primary challenge faced by the long cuff was the limitation of the implantation site size. Based on these characterizations, the opening height of 2.85 mm and length of 6.5 mm were

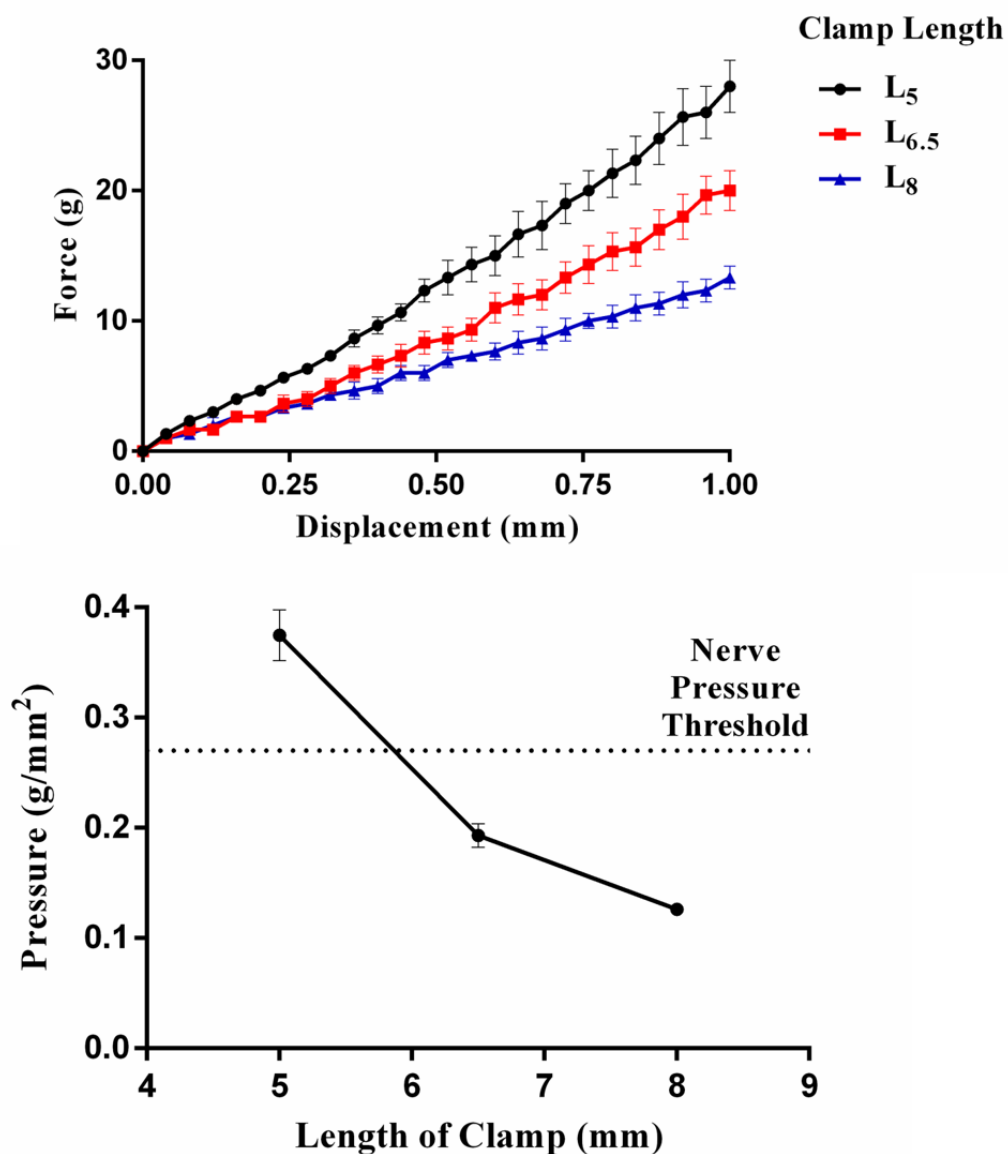


Figure 38. Characterization of Clamp's Length: (top) Force-displacement characteristic plot. (bottom) The pressure plot for clamps with different lengths. N=3 clamps tested for each clamp length. Error bars represent the standard error of the mean (SEM) of the measurements.

selected as optimum parameters (i.e, applying a small pressure on the nerve, while ensuring the size would be suitable at the site of implantation) for further tests.

4.6 Discussions

The findings conclude that the cuff-clamp electrode design with some modifications could be potentially used with the SDCS microfluidics for chronic pain suppression studies. The electrode design described here is an initial modification of a cuff electrode. While promising results for the pressures and impedance are obtained, this is simply a stepping stone for future design iterations, as many factors are yet to be investigated upon.

Pressures could be drastically reduced by manufacturing the clamp with a more flexible material than presently used with considerable strength to hold the electrode in place. The manufacturing technique employed for the fabrication of these PDMS based electrodes limits the method of closure to employing the clamp. Current design iterations were obtained through the implantation in cadaveric rats. While they are sufficient for determining the parameters related to the size of the electrode, it is purely qualitative. Further quantitative measurements such as testing the nerve responses of the live rat and histological analysis of the nerve with the electrode would be necessary for ascertaining the feasibility of the design. A vital feature that was missing from this design are the electrode contacts. An ionically conductive, biocompatible, and stable contact must be achieved with the nerve. Moreover, the positioning, number of contacts, electrode material and electrode contact material should prevent the shunting of the current. Additional alterations into the electrode material and electrolyte should be explored for improving the conductivity.

While the experiments explained in this chapter were used to gather preliminary data, further experimentation is certainly necessary to optimize the design of the electrode and add other features for not only the successful implantation on a sciatic nerve, but also the to conduct ionic current.

CHAPTER 5: CONCLUSIONS

While all existing neuroprostheses use biphasic pulsatile stimulation, the effectiveness of the system, particularly for the inhibition of the neural activity is reduced. On the other hand, direct current has the ability to excite and inhibit the neurons, but is subjected to toxic electrochemical reactions at the metal electrode-electrolyte interface. The SDCS tackles this issue by rectifying the input alternating current into ionic direct current, which can be supplied to the neural tissue safely. While the device as such can be divided into several functional layers; microfluidics, electronics, application-specific electronics and power, this thesis examines the microfluidic layer and establishes a neural interface that could possibly be used with the SDCS device.

This thesis covers the design, characterization and testing of microfluidic valves for the next generation SDCS device. A normally-closed, miniature valve that is actuated with shape memory alloy was described. Testing of these valve impedances for the open and closed states (as 1:10 ratio) established its ability to rectify the charge-balanced biphasic pulses into direct current. However, as seen in Figure 4, the SDCS device requires eight such valves. Delivery of the iDC through the tissue is made possible by governing the opening and closing states of the valves in a controlled manner so as to direct the path of the ionic direct current through the tissue in the same direction. Overall, this ion rectifier circuit when interfaced with the electronics, lays the groundwork for safe and effective delivery of iDC to excite, inhibit, block, or modulate the neuronal activity *in-vivo*.

While progressive steps are being made towards the development of a functional prototype of SDCS, a connecting bridge between the microfluidics and the neural tissue

is essential. Most of the typically used electrodes for neural prostheses are metallic in nature, which prove to be deleterious to the biological tissue in conjunction with SDCS. Although the SDCS concept is currently being experimented for 3 major applications, the focus of this thesis is specific to designing electrodes for pain studies. Work towards a preliminary design and testing of an electrode capable of carrying iDC is presented in this thesis. The cuff-clamp electrode system comprises of a PDMS based cuff electrode (length = 6.5 mm, thickness = 0.72 mm), which is secured over the nerve using a c-clamp (length = 6.5 mm, opening height = 2.85 mm). Sizes were chosen for implantation on the sciatic nerve of a rat. Moreover, the impedances obtained were around the SDCS device's allowable impedance of 100k Ω . Pressure calculations and impedance measurements verified the possibility of this system as a successful interface.

The microvalves and electrode system form the basis of the SDCS device design. Further research in the other layers (electronics, power, electrodes interfacing with microfluidic layer, chronic animal experiments for studying the effects of iDC, etc) and for optimizing the existing designs are necessary for building a functional prototype. Moreover, long-term experiments are to be carried out to establish the safety and efficacy of using direct current as a neuromodulation modality. The ultimate aim of this project is to establish a novel neuromodulation modality in the form of direct current, for expanding the range of applications of the existing implantable neural prostheses.

BIBLIOGRAPHY

- [1] D. Horch, Kenneth W., Kipke, *Neuroprosthetics Theory and Practice*. World Scientific, 2017.
- [2] G. G. Naples, J. T. Mortimer, A. Scheiner, and J. D. Sweeney, "A Spiral Nerve Cuff Electrode for Peripheral Nerve Stimulation," *IEEE Trans. Biomed. Eng. NO. 11*, vol. 35, 1988.
- [3] "About Neuromodulation." [Online]. Available: <http://www.neuromodulation.com/about-neuromodulation>. [Accessed: 21-Jun-2018].
- [4] D. R. Merrill, M. Bikson, and J. G. R. Jefferys, "Electrical stimulation of excitable tissue: design of efficacious and safe protocols," *J. Neurosci. Methods*, vol. 141, pp. 171–198, 2005.
- [5] S. F. Cogan, "Neural Stimulation and Recording Electrodes," *Annu. Rev. Biomed. Eng.*, vol. 10, pp. 275–309, 2008.
- [6] R. H. Kramer and C. M. Davenport, "Lateral Inhibition in the Vertebrate Retina: The Case of the Missing Neurotransmitter.," *PLoS Biol.*, vol. 13, no. 12, p. e1002322, Dec. 2015.
- [7] D. M. Ackermann, N. Bhadra, E. L. Foldes, K. L. Kilgore, and K. L. Kilgore, "Conduction block of whole nerve without onset firing using combined high frequency and direct current.," *Med. Biol. Eng. Comput.*, vol. 49, no. 2, pp. 241–51, Feb. 2011.
- [8] K. L. Kilgore, N. Bhadra, and K. L. Kilgore, "Direct Current Electrical Conduction Block of Peripheral Nerve," *IEEE Trans. NEURAL Syst. Rehabil. Eng.*, vol. 12, no. 3, 2004.
- [9] F. A. Hopp, E. J. Zuperku, R. L. Coon, and J. P. Kampine, "Effect of anodal blockade of myelinated fibers on vagal C-fiber afferents."
- [10] C. Cheng, A. R. Nair, R. Thakur, and G. Fridman, "Normally closed plunger-membrane microvalve self-actuated electrically using a shape memory alloy wire," *Microfluid. Nanofluidics*, vol. 22, no. 3, pp. 1–9, 2018.
- [11] J. D. Zahn, *Methods in Bioengineering: Biomicrofabrication and Biomicrofluidics*. Artech House, 2010.
- [12] K. W. Oh, R. Rong, and C. H. Ahn, "Miniaturization of pinch-type valves and pumps for practical micro total analysis system integration," *J. Micromechanics Microengineering*, vol. 15, no. 12, pp. 2449–2455, 2005.
- [13] Kuznetsov I. A., *Microfluidics: Theory and Applications*. Nova Science Publishers, 2010.
- [14] G. M. Whitesides, "The origins and the future of microfluidics," *Nature*, vol. 442, no. 7101, pp. 368–373, 2006.
- [15] W. Walz, *Microfluidic and Compartmentalized Platforms for Neurobiological Series Editor*. .
- [16] S. K. Y. Tang and G. M. Whitesides, "Basic Microfluidic and Soft Lithographic Techniques 2-1 Introduction 2-3 Materials for Fabricating Microfluidic Devices."
- [17] D. E. Angelescu, *Highly Integrated Microfluidics Design*. Artech House, 2011.
- [18] S. Waheed *et al.*, "3D printed microfluidic devices: enablers and barriers," *Lab Chip*,

vol. 16, no. 11, pp. 1993–2013, 2016.

- [19] Y. Xia and G. Whitesides, “Soft lithography,” *Annu. Rev. Mater. Sci.*, vol. 28, pp. 153–184, 1998.
- [20] and A. R. Keith, Herold E., *Lab on a Chip Technology. Fabrication and Microfluidics*. Caister Academic Press, 2009.
- [21] “Standard Terminology for Additive Manufacturing Technologies 1,2.”
- [22] R. Noorani, *3D Printing: Technology, Applications, Selections*. 2018.
- [23] A. K. Au, W. Huynh, L. F. Horowitz, and A. Folch, “3D-Printed Microfluidics,” *Angew. Chemie - Int. Ed.*, vol. 55, no. 12, pp. 3862–3881, 2016.
- [24] et al. Jackson, Beau, “The Free Beginner’s Guide - 3D Printing Industry.” [Online]. Available: <https://3dprintingindustry.com/3d-printing-basics-free-beginners-guide#02-history>. [Accessed: 24-Apr-2018].
- [25] “Types of 3D printers or 3D printing technologies overview.” [Online]. Available: <http://3dprintingfromscratch.com/common/types-of-3d-printers-or-3d-printing-technologies-overview/>. [Accessed: 25-Apr-2018].
- [26] P. J. (PJ), “Photopolymer Jetting - Additively.” [Online]. Available: <https://www.additively.com/en/learn-about/photopolymer-jetting#read-advantages>. [Accessed: 25-Apr-2018].
- [27] “SLA 3D Printing: Difference in Laser and DLP Light Pattern Generation - Kudo3D Inc.” [Online]. Available: <https://www.kudo3d.com/sla-3d-printing-difference-in-laser-and-dlp-light-generation/>. [Accessed: 07-May-2018].
- [28] “20 Best Resin (DLP/SLA) 3D Printers 2018 | All3DP.” [Online]. Available: <https://all3dp.com/1/best-resin-dlp-sla-3d-printer-kit-stereolithography/>. [Accessed: 07-May-2018].
- [29] “Materials | B9Creations.” [Online]. Available: <http://www.b9c.com/products/materials>. [Accessed: 07-May-2018].
- [30] “What is UV Curing, and What Can UV Curing Do for You?” [Online]. Available: <http://www.fusionuv.com/uvlearningcenter.aspx?id=206>. [Accessed: 07-May-2018].
- [31] C. E. Hoyle, “Photocurable Coatings,” pp. 1–16, 1990.
- [32] B. Verhaagen, T. Zanderink, and D. Fernandez Rivas, “Ultrasonic cleaning of 3D printed objects and Cleaning Challenge Devices,” *Appl. Acoust.*, vol. 103, no. July, pp. 172–181, 2016.
- [33] “How does ultrasonic cleaning work and why is it the best form of cleaning? | Sonic Pro.” [Online]. Available: <http://www.sonicpro.com/how-does-ultrasonic-cleaning-work/>. [Accessed: 25-Apr-2018].
- [34] H. H. Ultrasonic, “Fundamentals.”
- [35] ESP Group, “How Does UV Curing Work?,” p. 4.
- [36] A. Moeck and R. Ag, “Shrinkage of UV Oligomers and Monomers,” *Radtech Conf.*, pp. 5–9, 2014.
- [37] “UV Nail Lamps – The Facts.”
- [38] “Water absorption spectrum.” [Online]. Available: http://www1.lsbu.ac.uk/water/water_vibrational_spectrum.html. [Accessed: 07-May-

2018].

- [39] R. C. Inks, “Uv-radiation curing technology.”
- [40] I. D. Johnston, D. K. McCluskey, C. K. L. Tan, and M. C. Tracey, “Mechanical characterization of bulk Sylgard 184 for microfluidics and microengineering,” *J. Micromechanics Microengineering*, vol. 24, no. 3, 2014.
- [41] K. Haubert, T. Drier, and D. Beebe, “PDMS bonding by means of a portable, low-cost corona system,” *Lab Chip*, vol. 6, no. 12, p. 1548, 2006.
- [42] D. E. Angelescu, *Highly Integrated Microfluidics Design*. Artech House, 2011.
- [43] A. F. Ayhan, “DESIGN OF A PIEZOELECTRICALLY ACTUATED MICROVALVE FOR FLOW CONTROL IN FUEL CELLS,” 2002.
- [44] S. Prakash, *Nanofluidics and Microfluidics: Systems and Applications*. Elsevier Ltd, 2016.
- [45] N. Vandelli, D. Wroblewski, M. Velonis, and T. Bifano, “Development of a MEMS Microvalve Array for Fluid Flow Control,” *J. MICROELECTROMECHANICAL Syst.*, vol. 7, no. 4, 1998.
- [46] M. A. Huff, M. S. Mettner, T. A. Lober, and M. A. Schmidt, “A pressure balanced electrostatically-actuated microvalve,” *IEEE Solid-State Sensor and Actuator Workshop, 4th Technical Digest*. pp. 123–127, 1990.
- [47] K. W. Oh and C. H. Ahn, “A review of microvalves,” *J. Micromechanics Microengineering*, vol. 16, no. 5, pp. R13–R39, 2006.
- [48] J. . Zahn, *Methods in Bioengineering: Biomicrofabrication and Biomicrofluidics*. Artech House, 2010.
- [49] N. Li, C. Sip, and A. Folch, “Microfluidic Chips Controlled with Elastomeric Microvalve Arrays,” *J. Vis. Exp.*, no. 8, 2007.
- [50] A. Chen and T. Pan, “Manually operatable on-chip bistable pneumatic microstructures for microfluidic manipulations.,” *Lab Chip*, vol. 14, no. 17, pp. 3401–8, Sep. 2014.
- [51] C. S. S. R. Kumar, *Microfluidic Devices in Nanotechnology: Fundamental Concepts*. Wiley Inc, 2010.
- [52] S. Colin, *Microfluidics*. ISTE, 2010.
- [53] M. Koch, *Microfluidic Technology and Applications*. Research Studies Press, 2000.
- [54] M. Díaz-González, C. Fernández-Sánchez, and A. Baldi, “Multiple actuation microvalves in wax microfluidics,” *Lab Chip*, vol. 16, no. 20, pp. 3969–3976, 2016.
- [55] C. I. Rogers, J. B. Oxborrow, R. R. Anderson, L.-F. Tsai, G. P. Nordin, and A. T. Woolley, “Microfluidic Valves Made From Polymerized Polyethylene Glycol Diacrylate.,” *Sens. Actuators. B. Chem.*, vol. 191, Feb. 2014.
- [56] S. Augustine, P. Gu, X. Zheng, T. Nishida, and Z. H. Fan, “Low-power electrically controlled thermoelastic microvalves integrated in thermoplastic microfluidic devices,” *Microfluid. Nanofluidics*, vol. 19, no. 6, pp. 1385–1394, 2015.
- [57] C. Zhang, D. Xing, and Y. Li, “Micropumps, microvalves, and micromixers within PCR microfluidic chips: Advances and trends,” *Biotechnol. Adv.*, vol. 25, no. 5, pp. 483–514, 2007.
- [58] A. Ghosh, *Mechanics Over Micro and Nano Scales*. 2011.

- [59] S. Vyawahare *et al.*, “Electronic control of elastomeric microfluidic circuits with shape memory actuators,” *Lab Chip*, vol. 8, no. 9, p. 1530, Aug. 2008.
- [60] D. S. Goldberg and S. J. McGee, “Pain as a global public health priority,” *BMC Public Health*, vol. 11, no. 1, p. 770, Dec. 2011.
- [61] “Electrical Neuromodulation in Chronic, Intractable Pain.”
- [62] “Neuromodulation.” [Online]. Available: <http://www.neuromodulation.com/about-neuromodulation>. [Accessed: 06-Apr-2018].
- [63] H. Knotkova and D. Rasche, “Textbook of Neuromodulation.”
- [64] I. Jones and M. I. Johnson, “Transcutaneous electrical nerve stimulation,” *Contin. Educ. Anaesth. Crit. Care Pain*, vol. 9, no. 4, pp. 130–135, Aug. 2009.
- [65] H. Knotkova and D. Rasche, “Textbook of Neuromodulation.”
- [66] T. Deer, *Atlas of Implantable Therapies for Pain Management*. .
- [67] M. Karamanou, G. Tsoucalas, M. Lymperi, V. Gennimata, and G. Androutsos, “The "torpedo " effect in medicine,” *Int Marit Heal. Marit Heal.*, vol. 65, no. 2, pp. 65–67, 2014.
- [68] K. V. Slavin and S. Karger (Firm), *Peripheral nerve stimulation*. Karger, 2011.
- [69] “The History of Pain Treatments.”
- [70] P. Verrills, C. Sinclair, and A. Barnard, “A review of spinal cord stimulation systems for chronic pain,” *J. Pain Res.*, vol. 9, pp. 481–92, 2016.
- [71] C. N. Shealy, J. T. Mortimer, and J. B. Reswick, “Electrical Inhibition of Pain by Stimulation of the Dorsal Columns,” *Anesth. Analg.*, vol. 46, no. 4, pp. 489–491, 1967.
- [72] R. Melzack and P. D. Wall, “Pain Mechanisms: A New Theory A gate control system modulates sensory input from the skin before it evokes pain perception and response,” vol. 150, no. 3699, 1965.
- [73] P. D. Wall and W. H. Sweet, “Temporary Abolition of Pain in Man,” *Source Sci. New Ser.*, vol. 155, no. 3758, pp. 108–109, 1967.
- [74] K. V Slavin, “Technical Aspects of Peripheral Nerve Stimulation: Hardware and Complications,” pp. 1–21.
- [75] K. V. Slavin, *Stimulation of the peripheral nervous system : the neuromodulation frontier*. .
- [76] K. V. Slavin, “History of peripheral nerve stimulation,” *Prog. Neurol. Surg.*, vol. 24, no. March 2011, pp. 1–15, 2011.
- [77] “Peripheral Nervous System Anatomy: Overview, Gross Anatomy, Microscopic Anatomy.” [Online]. Available: <https://emedicine.medscape.com/article/1948687-overview>. [Accessed: 08-Jun-2018].
- [78] Y. Gao, C. Weng, and X. Wang, “Changes in nerve microcirculation following peripheral nerve compression,” *Neural Regen. Res.*, vol. 8, no. 11, pp. 1041–7, Apr. 2013.
- [79] A. P. Mizisin and A. Weerasuriya, “Homeostatic regulation of the endoneurial microenvironment during development, aging and in response to trauma, disease and toxic insult,” *Acta Neuropathol.*, vol. 121, no. 3, pp. 291–312, Mar. 2011.

- [80] A. Weerasuriya and A. P. Mizisin, "The Blood-Nerve Barrier: Structure and Functional Significance," Humana Press, 2011, pp. 149–173.
- [81] S. J. Carp, *Peripheral Nerve Injury: An Anatomical and Physiological Approach for Physical Therapy Intervention*. F.A. Davis Company, Philadelphia, 2015.
- [82] D. J. Tyler and D. M. Durand, "Chronic Response of the Rat Sciatic Nerve to the Flat Interface Nerve Electrode," *Ann. Biomed. Eng.*, vol. 31, no. 6, pp. 633–642, Jun. 2003.
- [83] M. Z. Siemionow, *Plastic and reconstructive surgery: experimental models and research designs*. Springer, 2015.
- [84] J. Badia, T. Boretius, D. Andreu, C. Azevedo-Coste, T. Stieglitz, and X. Navarro, "Comparative analysis of transverse intrafascicular multichannel, longitudinal intrafascicular and multipolar cuff electrodes for the selective stimulation of nerve fascicles," *J. Neural Eng.*, vol. 8, no. 3, p. 036023, Jun. 2011.
- [85] E. Brunton, C. W. Blau, and K. Nazarpour, "Multichannel cuff electrodes for peripheral nerve stimulation and recording," in *2016 IEEE International Conference on Systems, Man, and Cybernetics (SMC)*, 2016, pp. 003223–003227.
- [86] C. H. Thompson, M. J. Zoratti, N. B. Langhals, and E. K. Purcell, "Regenerative Electrode Interfaces for Neural Prostheses," *Tissue Eng. Part B Rev.*, vol. 22, no. 2, pp. 125–135, 2016.
- [87] J. J. Fitzgerald *et al.*, "interface Erratum : A regenerative microchannel neural interface for recording from and," *J. Neural Eng.*, vol. 016010, no. 9, 2012.
- [88] F. a Cuoco and D. M. Durand, "Nerve Cuff Electrodes," *Rehabilitation*, vol. 8, no. 1, pp. 35–41, 2000.
- [89] S. P. Lacour, G. Courtine, and J. Guck, "Materials and technologies for soft implantable neuroprostheses," *Nat. Rev. Mater.*, vol. 1, no. 10, 2016.
- [90] W. G. Moon, G.-P. Kim, M. Lee, H. D. Song, and J. Yi, "A Biodegradable Gel Electrolyte for Use in High-Performance Flexible Supercapacitors," *ACS Appl. Mater. Interfaces*, vol. 7, no. 6, pp. 3503–3511, Feb. 2015.
- [91] W. G. Moon, G. P. Kim, M. Lee, H. D. Song, and J. Yi, "A biodegradable gel electrolyte for use in high-performance flexible supercapacitors," *ACS Appl. Mater. Interfaces*, vol. 7, no. 6, pp. 3503–3511, 2015.
- [92] E. W. Lau, "Leads and Electrodes for Cardiac Implantable Electronic Devices," *Clin. Card. Pacing, Defibrillation Resynchronization Ther.*, 2017.
- [93] T. Da *et al.*, "Peripheral nerve stimulation to treat chronic painful syndromes* Estimulação de nervos periféricos no tratamento das síndromes dolorosas crônicas."
- [94] "Utilizing Nerve Cuff Electrodes for in vivo Peripheral Nerve Research." [Online]. Available: <https://www.slideshare.net/InsideScientific/utilizing-nerve-cuff-electrodes-for-in-vivo-peripheral-nerve-research>. [Accessed: 12-Jun-2018].
- [95] "10.1 Buckling." [Online]. Available: http://www.ah-engr.com/som/10_buckling/text_10-1.htm. [Accessed: 14-Jun-2018].
- [96] S. P. Lacour, G. Courtine, and J. Guck, "Materials and technologies for soft implantable neuroprostheses," *Nat. Rev. Mater.*, 2016.
- [97] F. Lotti, F. Ranieri, G. Vadalà, L. Zollo, and G. Di Pino, "Invasive Intraneural Interfaces: Foreign Body Reaction Issues.," *Front. Neurosci.*, vol. 11, p. 497, 2017.

- [98] A. Namasivayam, “Cochlear Implant Technical Issues Electrodes, Channels, Stimulation Modes and More,” pp. 1–6, 2017.
- [99] MedEsthetics, “Monopolar vs Bipolar RF.” p. 4.
- [100] B. E. Thorn, L. Applegate, and K. Jones, “The relative efficacy of monopolar vs. bipolar electrodes in stimulation-produced analgesia,” *Exp. Brain Res.*, vol. 79, no. 2, pp. 266–270, 1990.
- [101] J. Ballesterro *et al.*, “Reducing Current Spread by Use of a Novel Pulse Shape for Electrical Stimulation of the Auditory Nerve.,” *Trends Hear.*, vol. 19, Dec. 2015.
- [102] “ASPEN - Consequences of Nerve to Nerve Tube Diameter Mismatch.” [Online]. Available: <http://peripheralnerve.org/meeting/abstracts/2014/80.cgi>. [Accessed: 19-Jun-2018].
- [103] G. G. Naples, J. T. Mortimer, A. Scheiner, and J. D. Sweeney, “A Spiral Nerve Cuff Electrode for Peripheral Nerve Stimulation,” *IEEE Trans. Biomed. Eng. NO. 11*, vol. 35, 1988.
- [104] J. Kim, “Plateau-Shaped Flexible Polymer Microelectrode Array for Neural Recording,” 2017.
- [105] T. C. Smith, “Self-diffusion of ions in gels,” p. 43, 1963.
- [106] European Insulation Manufacturers Association, “Production Process,” pp. 1–3, 2011.
- [107] “Introduction to Psychology v1.0 | FlatWorld.” [Online]. Available: https://catalog.flatworldknowledge.com/bookhub/127?e=stangor-ch03_s01. [Accessed: 09-Jun-2018].
- [108] “What is an action potential? | Molecular Devices.” [Online]. Available: <https://www.moleculardevices.com/applications/patch-clamp-electrophysiology/what-action-potential>. [Accessed: 22-Jun-2018].
- [109] G. Y. Fridman and C. C. Della Santina, “Safe Direct Current Stimulation to Expand Capabilities of Neural Prostheses,” *IEEE Trans. Neural Syst. Rehabil. Eng.*, vol. 21, no. 2, pp. 319–328, Mar. 2013.
- [110] G. Y. Fridman and C. C. Della Santina, “Safe direct current stimulator 2: Concept and design,” in *2013 35th Annual International Conference of the IEEE Engineering in Medicine and Biology Society (EMBC)*, 2013, pp. 3126–3129.
- [111] A. Mao and P. Ou, “Developing a Microfluidic Device for Safe DC Stimulation,” *Minnesota Neuromodulation Symp.*, vol. 21, no. 2, p. 18818809, 2016.
- [112] “Fundamentals of the Nervous System and Nervous Tissue.” [Online]. Available: <https://antranik.org/fundamentals-of-the-nervous-system-and-nervous-tissue/>. [Accessed: 09-Jun-2018].
- [113] Z. Zhu, Q. Tang, F. G. Zeng, T. Guan, and D. Ye, “Cochlear-implant spatial selectivity with monopolar, bipolar and tripolar stimulation,” *Hear. Res.*, vol. 283, no. 1–2, pp. 45–58, 2012.

CURRICULUM VITAE

ANKITHA R. NAIR

500 W University Parkway, Apt 6H, Baltimore, MD 21210

Mobile: (443) 317-7299 | E-mail: anair9@jhu.edu | DOB: 11/15/1993 | Place of Birth: Bahrain

<https://www.linkedin.com/in/ankitha-rajagopalan-nair/>

EDUCATION

Johns Hopkins University (JHU), MD, USA

Master of Science in Engineering (MSE): Biomedical Engineering

Expected: August 2018

College of Engineering Trivandrum (CET), Kerala, India

Bachelor of Technology: Applied Electronics and Instrumentation

May 2015

WORK EXPERIENCE

Machine Biointerface Lab, Johns Hopkins University, MD, USA

Graduate Research Assistant (Master's Thesis)

Dec. 2016- Present

Design of a Neural Interface for Chronic Pain Suppression

- Created 3D models of neural interface designs using **SolidWorks** (involved working with SolidWorks mold tools), **3D printing** of the prototypes with a photopolymer resin, carried out inverse replica moulding using polymers and performed surgery and prototype implantation in sciatic nerves of small animal models.

Development of an Implantable, Elastomeric Microvalve for Neuromodulation

- Designed layer-by-layer models in SolidWorks for further assembly into miniature valves, performed resin-based 3D printing of these moulds, creation of negative impressions with polymers for obtaining elastomeric valves, corona treatment for bonding the layers of polymers, and performed shape memory alloy (Nitinol) actuation of the miniature valves.
- Collected and recorded **electrical impedance measurements**, data analysis and visualization using GraphPad **Prism** software, and circuit designing with Inkscape platform.

Human Molecular Genetics Lab, Rajiv Gandhi Centre for Biotechnology, Kerala, India

Summer Trainee

July 2015- Oct. 2015

- Identified SNP markers for complex disorders such as autism, schizophrenia and deafness.
- Gained practical knowledge on DNA isolation using Salting-Out and Phenol-Chloroform methods, amplification using PCR, sequencing and fingerprinting through RFLP.

PROJECTS

Haptic Feedback System for Upper Limb Trans-radial Myoelectric Prosthesis, JHU

Jan. 2017

- Designed a portable, wireless haptic band in conjunction with a wearable force sensing glove to improve the physical perception of the environment for upper limb amputees, by providing vibration feedback for contact and slip of an object.
- Developed using **Teensy** microcontroller, XBee, textile-based force sensors and vibration motors with Arduino IDE, XCTU and Teensyduino platforms. Analyzed real-time stimulation data with **PLX-DAQ** software.

Dynamic Mapping of the Environment, JHU*Sept. 2016 – Nov. 2016*

- Constructed a robot for its dynamic mapping and localization in unknown environments.
- Developed using *Arduino* microcontroller, ultrasonic sensor, infrared sensors, stepper motors, Pololu motor encoder and Darlington transistor array along with Arduino IDE. Data was processed using *MATLAB*.

Quadriplegic Gaming System: GameFace, JHU*Oct. 2016 – Nov. 2016*

- Designed a wearable biological gaming system that allowed disabled people to control a computer-based video game using puff and sip mechanisms and small head movements.
- Developed using a Teensy microcontroller, differential pressure sensors and infrared sensors with Arduino IDE platform.

UltraVision, JHU*Sept. 2016-Oct. 2016*

- Designed a wearable headband for the blind for obstacle detection & avoidance via auditory feedback with varying pitches.
- Developed using Arduino microcontroller, ultrasonic sensors and an analog speaker

FERO: Fire Extinguishing Robot, CET*June 2014- March 2015*

- Built a robot for detecting and extinguishing a fire in close proximity and for transmitting messages to alert the user
- Developed using Arduino microcontroller, flame sensors, ultrasonic sensor, DC motors and RF transmitters and receivers along with Arduino IDE and GSM platforms and a cam actuation mechanism.

RFID Based Toll Plaza, CET*Dec. 2013- March 2014*

- Automated the tolling mechanism for vehicles with the use of RFID tags
- Developed using ATMEL 89C51 microcontroller, RFID, LCD and servomotors along with Keil UVision software and layout construction and PCB design using Proteus and KiCad platforms.

PUBLICATIONS/PRESENTATIONS

- **A.R. Nair***, C. Cheng*, R. Thakur, G.Y. Fridman, “Normally-Closed Plunger-Membrane Microvalve Self-Actuated Electrically Using a Shape Memory Alloy Wire,” *Microfluidics and Nanofluidics*, Feb. 2018. (*joint first authors)
- C. Cheng, **A.R. Nair**, R. Thakur, G.Y. Fridman, “Shape Memory Alloy Actuated Miniature Mechanical Valve for Ionic Current Rectification,” 21st *North American Neuromodulation Society Annual Meeting*, Las Vegas, Nevada, Jan. 2018.
- C. Cheng, R. Thakur, **A.R. Nair**, S. Sterrett, G.Y. Fridman, “Miniature Elastomeric Valve Design for Safe Direct Current Stimulator,” 13th *IEEE Biomedical Circuits & Systems Conference*, Turin, Italy, Oct. 2017. (Presenter)